Diss. ETH Nr. 14399

Monte Carlo models for dosimetry in photon beam radiotherapy

Dissertation for the degree of

DOCTOR OF THE NATURAL SCIENCES

of the

SWISS FEDERAL INSTITUTE OF TECHNOLOGY

ZURICH, SWITZERLAND

presented by

Michael K Fix

Dipl. Phys. ETH

born on May 20, 1967

Germany

Accepted on the recommendation of

Prof. Dr. P. Niederer, examiner

Prof. Dr. P. Rüegsegger, co-examiner

Prof. Dr. R. A. Eichler, co-examiner

2001

Contents

Abstract

The Monte Carlo (MC) technique is recognized as the most accurate method to predict patient dose. Prerequisite for the high accuracy is, however, the precise knowledge of the characteristics of the radiation field, especially in the case of the complex application techniques used in intensity modulated radiotherapy (IMRT). In this work, MC beam models for a Varian Clinac 2300 C/D with a 6 and 15 MV photon beam have been developed, which are able to describe and analyze the dosimetric situation for IMRT in detail. On the basis of 6 and 15 MV phase space (PS) data, generated with the MC code GEANT, several simple beam models and a multiple source model are investigated.

The full PS information within the geometric radiation field including the head scatter is used to develop simple beam models, wherein the sources are assumed to be point sources. Four different models are investigated which involve different ways to determine the energies and locations of beam particles in the output plane by using a combination of constant or variable spatial fluence distributions with constant or off axis dependent photon energy spectra. Depth dose curves, profiles and relative output factors are calculated with these models and compared with measurements. Good agreement for these comparisons within the geometric radiation field are achieved for the model, which uses a variable spatial particle fluence distribution and off axis dependent photon energy spectra . All other models lead to appreciable deviations between calculated and measured depth doses and/or dose profiles.

For the multiple source model (MSM) the full PS information of the 6 and 15 MV beam is used to characterize 12 sources representing the main components of the beam defining system. By parametrizing the source characteristics and by evaluating the dependence of the parameters on field size, it is possible to extend the validity of the model to rectangular fields without additional precalculated PS data. To validate the MSM, fluences, energy fluences and mean energies determined from original PS data and those reproduced by the MSM are compared. They show very good agreement within 1% for both energies. In addition, the MC calculated primary photon energy spectra are verified by the corresponding energy spectra derived from transmission

measurements. Comparisons of MC calculated depth dose curves and profiles, using original and PS data reproduced by the MSM, agree within 1% and 1 mm for both energies. Deviations from measured dose distributions are within 1.5% and 1 mm. Calculated output factors for the 6 MV beam in 10 cm water depth agree within 1.5% with experimentally determined data.

In order to characterize a radiation field shaped by an multileaf collimator (MLC) the MSM is supplemented with an accurate model of an 80-leaf dynamic MLC. Using this supplemented MSM, lateral dose distributions are calculated in a water phantom and in a portal water phantom. Two test fields (one for 6 and one for 15 MV) for the step and shoot technique and two realistic fields (one for 6 and one for 15 MV) from an IMRT treatment plan delivered with dynamic MLC are investigated. MC calculated dose profiles using the MSM are in excellent agreement with measured data from film dosimetry for all cases studied. To assess possible spectral changes caused by the modulation of beam intensity by an MLC, the energy spectra in five portal planes are calculated for moving slits of different widths. The investigation of a 13 cm wide field shows an increase in mean photon energy of up to 16% for the 0.25 cm slit compared to the open beam for 6 MV and of up to 6% for 15 MV respectively. Due to transmission, scattered radiation and changes in the energy spectrum the energy fluence increases up to 40% for decreasing slit widths when the time of direct exposure through the slit is kept constant.

In conclusion, the MSM supplemented with the dynamic MLC has proven to be a powerful tool for investigational and benchmarking purposes or even for IMRT treatment planning.

Zusammenfassung

Die Monte Carlo (MC) Technik wird als die genauste Methode zur Dosisvorhersage in Patienten angesehen. Voraussetzung für die hohe Genauigkeit ist allerdings ein präzises Wissen über die Strahlcharakteristik, insbesondere im Falle von komplexen Bestrahlungstechniken, wie sie in der intensitätsmodulierten Radiotherapie (IMRT) verwendet werden. In dieser Arbeit wurden MC Strahlmodelle für einen Varian Clinac 2300 C/D mit einem 6 und 15 MV Photonenstrahl entwickelt, welche in der Lage sind, die dosimetrische Situation in der IMRT detailliert zu beschreiben und zu analysieren. Auf der Basis von Daten der Phasenräume (PS) für 6 und 15 MV, welche mit dem MC Programm GEANT erzeugt wurden, werden verschiedene einfache Strahlmodelle sowie ein Mehrkomponentenmodell untersucht.

Die gesamten PS Informationen innerhalb des geometrischen Strahlungsfeldes, einschliesslich der Streustrahlung des Beschleunigerkopfes, wurde für die Entwicklung von einfachen Stahlmodellen verwendet, bei welchen die Quellen als Punktquellen angenommen werden. Vier verschiedene Modelle werden untersucht, welche jeweils verschiedene Möglichkeiten zur Bestimmung der Energie und des Partikelortes in der Austrittsebene beinhalten, indem konstante oder variable räumliche Fluenzverteilungen mit konstanten oder radial-ortsabhängigen Energiespektren kombiniert werden. Mit diesen Modellen werden Tiefendosiskurven, Profile und relative Output Faktoren berechnet und mit Messungen verglichen. Eine gute Übereinstimmung für diese Vergleiche wird für das Modell erhalten, welches eine variable räumliche Fluenzverteilung des Partikels mit radial-ortsabhängigen Energiespektren verknüpft. Alle anderen Modelle führen zu merklichen Abweichungen zwischen berechneten und gemessenen Tiefendosen und/oder Dosisprofilen.

Für das Mehrkomponentenmodell (MSM) wird die gesamte PS Information für den 6 und 15 MV Strahl für die Beschreibung von 12 Quellen verwendet, welche die Hauptbestandteile des Beschleunigerkopfes sind, um den Strahl zu formen. Durch Parametrisierung der Quellencharakteristiken und durch das Beurteilen der Feldgrössenabhängigkeit der Parameter, kann die Gültigkeit des Modells ohne zusätzliche vorausberechnete PS Daten auf Rechteckfelder erweitert werden. Um das MSM zu validieren

werden Fluenzen, Energiefluenzen und mittlere Energien, welche aus den originalen und aus den vom MSM reproduzierten PS Daten bestimmt wurden, miteinander verglichen. Dabei zeigt sich eine gute Übereinstimmung innerhalb 1% für beide Energien. Zusätzlich werden die mit MC berechneten primären Energiespektren der Photonen mit entsprechenden Energiespektren, die aus Transmissionsmessungen rekonstruiert wurden, verifiziert. Vergleiche von MC gerechneten Tiefendosiskurven und Profilen, bei welchen die originalen und die mit dem MSM reproduzierten PS Daten verwendet werden, stimmen für beide Energien innerhalb von 1% und 1 mm überein. Abweichungen zu den Messungen sind innerhalb von 1.5% und 1 mm. Gerechnete Output Faktoren für den 6 MV Strahl in 10 cm Wassertiefe stimmen innerhalb von 1.5% mit experimentell bestimmten Werten überein.

Um ein mit einem Mehrlamellenkollimator (MLC) geformtes Feld charakterisieren zu können, wird das MSM mit einem genauen Modell eines dynamischen 80-Lamellen MLCs erweitert. Mit dem erweiterten MSM werden laterale Dosisverteilungen in einem Wasserphantom und in einem portalen Wasserphantom berechnet. Zwei Testfelder (eines für 6, das andere für 15 MV) für die step and shoot Technik und zwei realistische Felder (eines für 6, das andere für 15 MV) aus einem IMRT Bestrahlungsplan mit dynamischem MLC werden untersucht. Für alle untersuchten Situationen sind die mit dem MSM berechneten Dosisprofile in sehr guter Übereinstimmung mit Messungen aus der Filmdosimetrie. Um mögliche spektrale Änderungen zu erfassen, die durch die Modulation des Strahles durch den MLC bedingt sind, werden Energiespektren für dynamische Schlitze verschiedener Breiten in fünf Portalebenen berechnet. Die Untersuchung der Schlitzbestrahlungen in einem 13 cm breiten Feld zeigt im Vergleich zu einem offenen Strahl einen Anstieg der mittleren Photonenenergie um bis zu 16% für den 0.25 cm Schlitz für den 6 MV Strahl und um bis zu 6% für den 15 MV Strahl. Auf Grund von Transmission, Streustrahlung und Änderungen im Energiespektrum steigt die Energiefluenz für schmaler werdende Schlitzbreiten um bis zu 40% an, falls die Zeit der direkten Bestrahlung durch den Schlitz hindurch konstant gehalten wird.

Insgesamt zeigt sich, dass das mit dem dynamischen MLC erweiterte MSM ein mächtiges Tool ist, welches für Untersuchungen, zur Bestimmung von Bezugswerten oder sogar für die Bestrahlungsplanung in der IMRT einsetzbar ist.

1

Introduction

Cancer is the second leading cause of death in the western world and therefore a main problem in health care. The estimated incidence for the year 2000 is about 500 per 100000 citizens for the United States as well as for Germany (Ferlay 2000, van Dyk 1999). On the other hand the corresponding death rate of cancer during the years 1994-1997 reached about 0.25% of the citizens per year (Ferlay 2000), which means that every second person who is diagnosed with cancer dies from this disease. More than one in three persons will develop cancer during their lifetime and about one in four persons will die of cancer. Radiotherapy is one of the three principle methods available to cancer patients. It uses ionizing radiation to sterilize cancerous cells and has proven to be an effective treatment method for a variety of tumors. Today it is prescribed to more than half of the cancer patients (Karzmark 1993). Surgery and chemotherapy are the other two major modes used in cancer therapy. In many cases a combination of these three modes of therapy is applied.

Since Betatrons and ^{60}Co units replaced the x-ray machines after the late 1950's, which was accompanied by a shift from kilovoltage into megavoltage radiation therapy, an enormous improvement in overall five years survival from 39% in the 1960's to 50% in the 1980's took place (van Dyk 1999). Since the 1970's, medical linear accelerators became available, which generate megavoltage electrons in an energy range from 4 to 50 MeV using microwave wave-guides. These high-energy electrons are used to produce clinically useful electron and photon beams, which today are the most common types of radiation in radiotherapy. In some cases also protons or neutrons are used.

To eradicate tumors within the human body using one or several of these types of ionizing radiation, the radiation beams usually traverse normal tissue and cause the possibility of treatment complications, even when several beams with different beam directions are focused on the tumor. In the simplest form, the response of tumors and normal tissues to irradiation follow sigmoidal dose-response curves (figure 1).

Thereby dose is defined as the amount of energy deposited by the radiation beam in a medium per unit mass of the medium (unit Gray: 1Gy = 1J/kg).

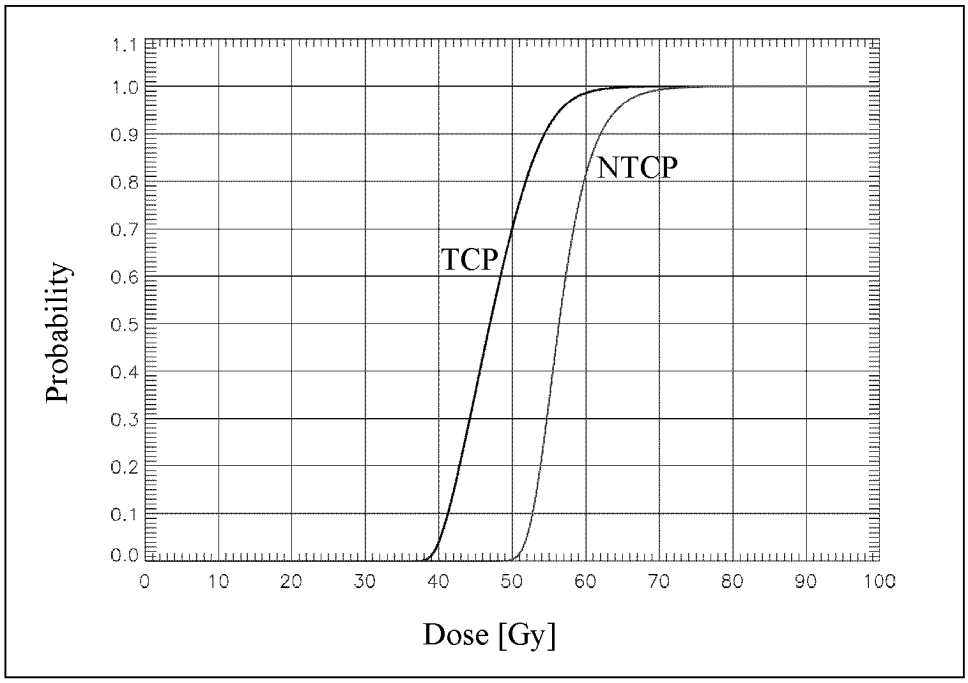

Figure 1 *Schematic dose-response curves for tumor control probability (TCP) and normal tissue complication probability (NTCP). (Illustration adapted from van Dyk 1999.)*

The sigmoidal shape of the curves implies the existence of dose thresholds. For higher doses a sharp increase in tumor and tissue response can be observed. As the dose is increased even more, the slope decreases and asymptotically reaches the likelihood of one for both the tumor response and the normal tissue complication. Therefore, the aim of radiotherapy is to deliver such an amount of radiation to a well-defined target volume to reach a high tumor control probability (TCP) while keeping the normal tissue complication probability (NTCP) at an acceptable level. Clinical data about position and shape of TCP and NTCP curves (figure 1) suggest, that, in order to reach this goal, the accuracy of the doses applied in radiotherapy has to be within ±5% (ICRU report 24 1976).

The desire to tailor geometrically the spatial dose distribution to the tumor of a particular patient by shaping each beam individually is referred to as *conformal radiotherapy*. Minimizing the amount of normal tissue irradiated while covering accurately the target volume should lead to fewer complications and to better local tumor control

resulting in better cure rates. In the mid 90's, a new technique, the *intensity modulated radiotherapy (IMRT)*, was developed to improve the conformal radiotherapy. In IMRT the particle fluence (number of particle per area) at each point of the irradiated field is adapted or modulated to reach an optimal 3D dose conformation to the tumor and to reduce dose in normal tissue. The implementation of conformal radiotherapy and IMRT requires sophisticated medical equipment. Today linear accelerators equipped with multileaf collimators (MLCs) are most commonly used for this purpose.

1.1. Linear accelerator

The principal components of linear accelerators for use in radiotherapy are illustrated in figure 2. As this work is focused on photon beams, this thesis is restricted to the photon mode.

The megavoltage x-rays are created when high-energy electrons are stopped in a target. These electrons are first boiled off a filament, accelerated to kilovoltage energies in an electron gun and injected into a wave-guide, which receives its power from a magnetron, klystron or microtron. The electrons leaving the wave-guide are roughly monoenergetic with an energy in the megavoltage range. They pass a bending magnet (usually 270°) and thus are directed towards the tumor within the patient. In the photon mode, the electrons hit the target where x-rays with a broad energy spectrum are produced by bremsstrahlung. The target is surrounded by a shield of tungsten which serves as a primary collimator of the photon beam. The angular distribution of the bremsstrahlung photons at megavoltage energies is primarily forward-peaked and therefore the beam has to be flattened by a flattening filter in order to achieve homogeneous intensity over field widths used in radiotherapy. The shape of the flattening filter is different for each beam energy and strongly influences the characteristics of the x-ray treatment beam. Just below the flattening filter, a dual sealed ion chamber or monitor chamber, impervious to changes in temperature and pressure, is mounted for rigorous beam control. The monitor chamber actually measures the dose in arbitrary units called “monitor units” (MU). Generally, the sensitivity of the monitor chamber is adjusted such that 1 MU corresponds to a dose of 1 cGy in a phantom under reference conditions.

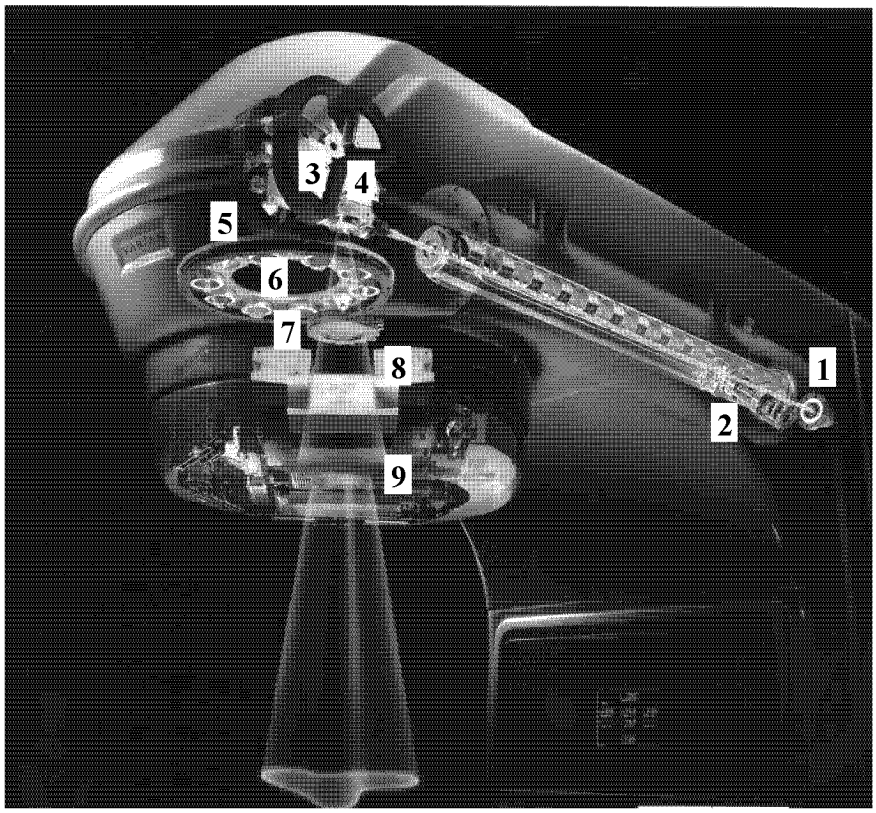

Figure 2 *A typical beam delivery system for a linear accelerator: gripped electron gun (1), where the preaccelerated electrons are transferred into the wave-guide; energy switch (2), which selects the correct beam energy; 270°-3-field bending magnet (3) to change beam direction and focus the electron beam on the target; focal spot on the target (4); real time beam control steering system (5), which ensures beam symmetry to within 2%; port-carousel (6) to select the correct flattening filter (or scattering foil in the electron mode); dose monitor (7), by which the output of the linear accelerator is controlled; asymmetric jaws (8) to adjust the boundaries of the beam of rectangular symmetric and asymmetric fields; MLC (9) to provide arbitrary beam shapes. (Illustration adapted from Varian Medical Systems.)*

Below the monitor chamber four independent collimator jaws allow flexible beam definition of rectangular symmetric and asymmetric fields. Arbitrary field apertures can be achieved by manufacturing a custom metal block, which is placed in an accessory tray below the secondary collimator. Another approach is to produce non rectangular fields with an MLC. This collimator consists of movable tungsten leaf pairs with a width of a few millimeters, which can be adjusted independently from each other. In principle the MLCs are predestinated to modulate beam intensity for IMRT fields.

There are mainly two application methods (Webb 2001): firstly, the *step and shoot* method using multiple-static MLC-shaped fields, and secondly, the *dynamic MLC* method, where leaf positions, and therefore the beam shape, change continuously during the application. The position and movement of the leaves are steered by a special MLC-controller and several tools for the calculation of the leaf motion have been developed to produce a given beam modulation (Boyer and Strait 1997, Stein 1997, Svensson *et al* 1994, Spirou and Chui 1994, Webb 1997 chapter 2).

The linear accelerator including the beam defining system is mounted within a gantry together with electronic and other systems and can be rotated around a horizontal gantry axis. The beam central axis intersects the gantry axis at a point in space called the isocenter. Usually, the distance between the target and the isocenter is 1 m.

Each photon beam in a phantom can be characterized by the three-dimensional dose distribution. A practical and efficient representation of this distribution consists of three dosimetric quantities: the depth dose curves, the dose profiles and the output factors. The depth dose curves describe the variation of the central axis dose with depth in a phantom, usually normalized to 100% in the depth of dose maximum. The depth dose curve is a function of beam energy, field size and source to surface distance (SSD). The dose profiles give the variation of dose in a phantom perpendicular to the central axis at a specific depth in the phantom. The dose profile is a function of beam energy, field size, SSD and size of the focal spot on the target. The output factor expresses the dose rate at a point on the central axis in the phantom for a given field in relation to the dose rate in that point for a reference field. The output factor changes with beam energy, SSD and size of the focal spot on the target. The influence on dose profiles and output factors resulting from the divergence of the electron beam incident on the target can be neglected (Sheikh-Bagheri 1998). Knowledge of the three dosimetric quantities for a treatment beam allows to determine the dose at any point in the phantom.

The variations in the output of the linear accelerator strongly influence the dose distribution in the patient and therefore the outcome of the therapy. Several studies have estimated the total uncertainty in dose delivery through the entire radiotherapy process at an arbitrary point in the patient (including also determination of absorbed

dose, patient positioning, organ motion, etc.) to be within ±4.5% (1 SD) (Mijnheer *et al* 1987, Brahme 1988, Karzmark 1993, Curtin-Savard 1998).

1.2. Photon beam dose calculations

Since direct measurements of the 3-dimensional dose distribution in the patient are not possible, the need to predict the effect of the radiation in the patient becomes important. In order to obtain a suggested accuracy of the radiation treatment of about ±5% and taking the accuracy of dose delivery within ±4.5% into account, the accuracy of dose calculation should be within ±2% (Ahnesjö and Aspradakis 1999, Cris 1999).

Traditionally, the patient dose calculation of photon beams is based on correcting dose distributions measured in a homogenous water phantom (Mackie *et al* 1996). More complex algorithms for dose calculation make use of models for radiation transport, as for example the *convolution/superposition* method and the *Monte Carlo* (MC) method, which are briefly discussed in the following sections.

1.2.1. Convolution/Superposition method

The convolution/superposition method has been extensively used to calculate photon dose distributions (Mackie *et al* 1985, Boyer and Mok 1985, Mohan *et al* 1986, Zhu and Boyer 1990, Ahnesjö *et al* 1992, Liu *et al* 1997a,b). This method calculates the photon dose $D(x,y,z)$ as the convolution between the total energy released in medium (TERMA in J/kg) $T(x,y,z)$ due to primary photon interactions in the considered volume and a spatially invariant photon dose kernel $K(x,y,z)$:

$$D(x,y,z) = \iiint T(x',y',z') \cdot K((x,y,z)-(x',y',z'))dx'dy'dz'.$$

The TERMA can analytically be computed from the product of photon energy E, photon fluence ϕ and mass attenuation coefficient μ/ρ:

$$T(x,y,z) = \frac{\mu(E)}{\rho} \cdot \phi(x,y,z) \cdot E\,.$$

The TERMA represents the total energy deposited in the medium by the primary photon interaction. The dose kernel, on the other hand, describes the distribution of rela-

tive energy deposition per unit volume at *(x,y,z)*, which follows the primary interaction at *(x',y',z')*:

$$K((x,y,z)-(x',y',z')) = \frac{dE(x,y,z)}{Edxdydz}$$

and is obtained by MC simulation (Mackie *et al* 1985, Mackie *et al* 1988) or analytical derivation (Boyer and Mok 1985, Mohan *et al* 1986). This kernel is only spatially invariant for a monoenergetic photon beam in an infinite and homogenous medium. Therefore, a superposition method for the TERMA and the kernel has been added to apply the convolution technique to polyenergetic photon beams leading to T^{pol} and K^{pol} (Mackie *et al* 1985, Boyer and Mok 1985, Zhu and Boyer 1990):

$$T^{pol}(x,y,z) = \sum_E \frac{\mu(E)}{\rho} \cdot \phi'(E,x,y,z) \cdot E$$

$$K^{pol}(x,y,z) = \sum_E \frac{\mu(E)}{\rho} \cdot \phi'(E,x,y,z) \cdot E \frac{K(E,x,y,z)}{T^{pol}(x,y,z)}$$

where $\phi'(E,x,y,z)$ is the photon spectrum normalized to the one at the isocenter and $K(E,x,y,z)$ is the dose kernel for the energy E. In order to use the convolution/superposition method for dose calculation in a patient further corrections have to be applied, e.g. for finite patient size, inhomogeneities, charged particle contamination of the beam, etc. It should be noted that these correction factors can lead to appreciable errors in calculated dose values (Woo and Cunningham 1990, Werner *et al* 1990).

1.2.2. Monte Carlo method

The MC technique is being recognized as the most accurate method to predict patient dose (Mohan 1997),but in addition it is also used for accelerator design (McCall *et al* 1978, Sätherberg and Karlsson 1998, Faddegon 1999). The MC calculations simulate the stochastic nature of particle interactions by the means of sampling randomly from known cross sections of particle interactions. The trajectory of the particle is simulated until its energy falls below an energy threshold or leaving the volume of interest. Secondary particles above a certain energy threshold are transported individually. Apart from the precision of the cross section data, the accuracy of the MC calculations depends mainly on the correctness of the information about the starting condition of the

radiation transport, the geometry of the setup and the materials used. Using the MC method for treatment planning in radiotherapy a two step approach is indicated: firstly, the beam output of the linear accelerator is modelled, and secondly, the dose distribution in the patient or phantom is calculated by using the beam model created in the first step. Thus, a prerequisite for the second step is an accurate characterization of the treatment beam. This characterization of the beam is best assessed by MC simulation of the radiation transport from the focal spot on the target through the beam defining system. In the following the interactions modelled in the MC code *GEometry ANd Tracking (GEANT)* (CERN 1995), used in this thesis, are described. Thereafter, some general aspects of GEANT are briefly discussed.

1.2.2.1. Electron and positron interactions

When traversing matter, electrons and positrons undergo deflection from their original trajectory due to the electric field of nuclei and electrons via a large number of elastic collisions. Most charged particle transport algorithms use a multiple-scattering theory in order to group the individual elastic scattering events to just one single step. In GEANT, the Molière multiple scattering theory is used by default, but when the number of scattering events is below the limit of applicability for Molière, single Coulomb scattering is simulated (CERN 1995).

It is also possible that the charged particles interact with matter via inelastic collisions. In principle there are two types of collision: firstly, the collisions where the energy transferred to the atomic electrons is high enough to extract them from the atoms (ionization with production of electrons: δ-rays) and secondly, collisions where the atomic structure is excited without a complete ionization. In GEANT, the Møller scattering theory and the Bhabha scattering formalism are used for the electron-electron collisions and positron-electron collisions respectively (CERN 1995).

The inelastic scattering of electrons and positrons from the electromagnetic field of the nuclei is called bremsstrahlung. During bremsstrahlung the incident charged particle transfers a part or even all of its energy to a photon, which is created in this process. In the MC algorithm a secondary particle is only simulated if its energy is above a threshold. Otherwise, its energy is deposited locally. In GEANT, the cross section as

well as the energy sampling of the created photon are based on values from Seltzer and Berger (CERN 1995).

Finally, positrons can annihilate in matter, whereby one or several photons can be produced. In GEANT the one- and two-photon positron-electron annihilation are simulated. For the latter case the cross section formula of Heitler is used (CERN 1995).

1.2.2.2. Photon interactions

The interactions of photons with matter depend mainly on their energy. At low energies (a few tens of keV) the photoelectric effect is the predominant process, in which the photon is absorbed by a bound electron. This electron is ejected from the atom and leaving a hole. Filling the hole with a higher-level electron, causes the production of characteristic radiation, which is also supported by GEANT. The cross section for the photoelectric effect is strongly affected by the atomic number (proportional to Z^3).

At higher energies, around 1 MeV, the most likely process of interaction is the Compton scattering. In this process the photon scatters from an orbital electron, which is ejected from the atom. Since the number of recoil electrons whose energy is low compared with their binding energy is very small, it is justified to consider the bound electron as free and to neglect the effect of the binding energy on the cross section. The Compton scattering is the dominating process for all materials over the energy range mainly dealt with in radiotherapy. For example, more than half of the total cross section from 25 keV to 25 MeV for carbon is Compton scattering (Johns and Cunningham 1983).

This is in contrast to the elastic photon scattering from an atom, called Rayleigh scattering. Rayleigh scattering contributes to the total cross section only with a few percent in a very low energy range (<100 keV). The dependence of Rayleigh scattering on the atomic number is complex, varying between Z^2 for small and Z^3 for large scattering angles. In order to characterize the linear accelerator very accurately, especially for the angular distribution, the MC simulations account also for Rayleigh scattering.

If the energy of the photon exceeds a few MeV, the process of pair production begins to dominate, whose cross section is proportional to Z^2. During this process, an

electron-positron pair is produced when the photon is absorbed by the electromagnetic field of the nucleus. In addition, rarely a triplet production takes place, where the photon interacts with the electromagnetic field of an orbiting electron, creates an electron-positron pair and transfers a substantial amount of its energy to the electron. Although this process is included in the total cross section of the pair production in GEANT, the recoil momentum of the electron/nucleus as well as the third particle created is ignored (CERN 1995).

In the photonuclear interaction a photon is absorbed by a nucleus and a nucleon is ejected. The resonance in cross section is centered at around 12 MeV and 24 MeV for high-Z and low-Z materials, respectively (Reich 1990). If the interaction with the nucleus is elastic, the process is also called Thompson scattering. Photonuclear processes (elastic and inelastic) are commonly ignored in radiotherapy MC simulations as discussed in Rogers and Bielajew (1990); therefore they are also ignored in this thesis.

All other rare interactions of photons with matter, as for example the double-Compton process, are not explicitly simulated in MC simulations in radiotherapy, because their contribution can be neglected.

1.2.2.3. The Monte Carlo code GEANT

Originally, the *GEANT-Detector Description and Simulation Tool* program was designed for high-energy physics experiments and has been developed at CERN. However, today GEANT has found applications in many other areas such as medical and biological sciences, radio-protection and astronautics. The GEANT system is written in a user-friendly way, which, apart from the transport of particles, provides a graphics support that allows on-line monitoring of the geometry of the setup. GEANT is essentially a library of routines offered to the user for the construction of specific applications and enables to

- describe the geometrical arrangement of a number of volumes. These volumes are defined by their boundaries and the tracking medium parameters, which represent the material filling the volume (initialization);
- accept events simulated by MC generators in order to start or continue a tracking process (event processing);

- transport the particles through the setup, taking into account geometrical volume boundaries and physical effects according to the nature of the particles themselves, their interactions with matter and the magnetic field (event processing);
- record particle trajectories (event processing);
- visualize the setup and the particle trajectories (event processing);
- save data and compute some statistical information (termination).

By means of systematic fits to existing data, the cross sections of the electromagnetic interactions are well reproduced from 10 keV to 10 GeV (energy cut-off range), both for materials with low-Z and high-Z. The electromagnetic physics package accounts for Rayleigh scattering, photo-electric effect, Compton scattering, pair production and photonuclear interactions for processes with photons. In addition, the secondary processes of characteristic radiation and the production of Auger electrons are considered. For electron/positron interactions the package includes the multiple scattering, ionization, the bremsstrahlung and the annihilation processes.

One will encounter some limitations of GEANT when defining volumes. GEANT provides a set of possible geometrys and therefore not all arbitrary geometries of a volume can be defined. Additionally, there are no variance reduction methods included in GEANT. Another drawback is the increasing simulation time with an increasing number of volumes.

1.3. Outline of the thesis

The aim in radiotherapy is to deliver radiation accurately to a well-defined target volume with minimal damage to surrounding healthy tissues. In order to reach this goal, novel application techniques dealing with IMRT have been developed recently. Using this new technique in a step and shoot or even sliding window approach, the demand on treatment planning systems increases considerably, especially on the beam models therein. Most current treatment planning systems do not reach the required accuracy for these new application techniques. Furthermore, the treatment planning systems are not flexible enough, for example, to calculate a portal dose image in a plane below the patient or to analyze the influence of the MLC on energy spectra during a dynamic MLC application. The aim of this thesis is to develop a flexible tool, which is able to

accurately describe and analyze the dosimetry in IMRT. For this purpose the tool is based on the MC method, which is the most accurate approach to characterize the beam and to calculate dose distributions. It is applied to the Varian Clinac 2300 C/D equipped with a 6 and 15 MV photon beam.

As already mentioned, an accurate beam characterization in form of an MC beam model is a prerequisite for an accurate calculation of dose distributions. For this purpose, in chapter 2 simple MC beam models are developed in order to investigate, under what conditions simple models can be found, which, nevertheless, allow the calculations of sufficiently accurate dose distributions.

Although the simple MC beam models lead to acceptable accuracy within the geometrical beam boundaries, these models are lacking in flexibility and show limitations in modelling the beam outside the geometrical field boundaries. Therefore, a multiple source model (MSM) for the 6 MV photon beam has been developed, which is described in chapter 3. Apart from phase space and dose comparisons, the MC calculated primary energy spectrum is compared with an energy spectrum derived from transmission measurements.

The method of measuring the primary energy spectra was introduced by Francois *et al* (1993). They suggest to reconstruct the energy spectrum by directly solving a matrix system using spectral algebra. The corresponding Mathematica algorithm of this reconstruction is discussed in chapter 4.

In order to apply dynamic MLC calculations, the MSM is supplemented by implementing an MLC. Using this supplemented MSM several applications are performed, such as dose calculations of static and dynamic MLC fields and calculations of energy fluence maps. The implementation of the MLC and the applications are described in chapter 5.

In chapter 6, an MSM for the 15 MV beam has been developed. Phase space and dose comparisons are made and the MC calculated primary energy spectrum is compared with the measured one. Besides dynamic MLC dose calculations for both a step and shoot and a sliding window application, portal dose images are calculated and compared with film measurements. To show the flexibility of the supplemented MSM and its use to analyze a complex application, the influence of the dynamic MLC on energy spectra is investigated for both energies.

Chapter 7 discusses certain aspects of uncertainty of MC simulations and dose measurements and chapter 8 draws final conclusions.

References

Ahnesjö A and Aspradakis M M 1999 Dose calculations for external photon beams in radiotherapy *Phys. Med. Biol.* **44** R99-R155

Ahnesjö A, Saxner M and Trepp A 1992 A pencil beam model for photon dose calculation *Med. Phys.* **19** 263-73

Boyer A L and Mok E C 1985 A photon dose distribution model employing convolution calculations *Med. Phys.* **12** 169-77

Boyer A L and Strait J P 1997 Delivery of intensity-modulated treatments with dynamic multileaf collimator *Proc. 12th Int. Conf. on the Use of Computers in Radiation Therapy (Salt Lake City, Utah, May 1977)* ed D D Leavitt and G Starkschall (Madison, WI: Medical Physics Publishing) pp13-16

Brahme A, ed 1988 Accuracy requirements and quality assurance of external beam therapy with photons and electrons *Acta Oncol.* Suppl. 1

CERN Application Software Group Computing and Network Division 1995a GEANT–detector description and simulation tool *CERN Program Library Long Writeup* W5013 Genf

Cris C 1999 Transport der Sekundärenergie im Rahmen einer makroskopischen Monte-Carlo Methode und Modellierung klinischer Bestrahlungsfelder mit Hilfe von Monte-Carlo Verfahren *PhD Thesis* University of Bern

Curtin-Savard A J 1998 Delivery and verification of intensity-modulated y-ray beams in radiotherapy *PhD Thesis* McGill University Montrèal

Faddegon B A, O'Brien P and Mason D L D 1999 The flatness of Siemens linear accelerator x-ray fields *Med. Phys.* **26** 220-8

Ferlay J, Bray F., Pisani P and Parkin D M 2000 GLOBOCAN: Cancer Incidence, Mortality and Prevalence Worldwide, Version 1.0 IARC CancerBase No. 5. Lyon, IARC Press, 2001, URL: http://www-dep.iarc.fr/globocan/globocan.htm

Francois P, Catala A and Scouarnec C 1993 Simulation of x-ray spectral reconstruction from transmission data by direct resolution of the numeric system *AF=T Med. Phys.* **20** 1695-703

ICRU 1976 Determination of absorbed dose in a patient irradiated by beams of x or gamma rays in radiotherapy procedures *ICRU report 24* (Bethesda, MD: International Commission on Radiation Units and Measurement)

Johns H E and Cunningham J R 1983 *The physics of radiology, 4th edition* (Springfield, IL: Charles C Thomas)

Karzmark C J, Nunan C S and Tanabe E 1993 *Medical Electron Accelerators* (New York, NY: NcGraw-Hill)

Liu H H, Mackie T R and McCullough E C 1997a A dual source photon beam model used in convolution/superposition dose calculations for clinical megavoltage x-ray beams *Med. Phys.* **24** 1960-74

——1997b Calculating output factors for photon beam radiotherapy using a convolution/superposition method based on a dual source photon beam model *Med. Phys.* **24** 1975-85

Mackie T R, Bielajew A F, Rogers D W O and Battista J J 1988 Generation of photon energy deposition kernels using the EGS Monte Carlo code *Med. Phys.* **33** 1-20

Mackie T R, Reckwerdt P, McNutt T 1996 Photon beam dose computations *Teletherapy: Present and Future* ed T R Mackie and J R Palta (Madison, WI: Advanced Medical Publishing) pp 103-135

Mackie T R, Scrimger J W and Battista J J 1985 A convolution method of calculating dose for 15 MeV x rays *Med. Phys.* **12** 188-96

McCall R C, McIntyre R D and Turnbull W G 1978 Improvement of linear accelerator depth-dose curves *Med. Phys.* **5** 518-24

Mohan R 1997 Why Monte Carlo? *XII Int. Conf. on the Use of Computers in Radiation Therapy (Salt Lake City, Utah, May 1997)* pp 16-18

Mohan R, Chui C and Lidofsky L 1986 Differential pencil beam dose computation model for photons *Med. Phys.* **13** 64-73

Reich H 1990 Wechselwirkung von Photonen mit Materie *Dosimetrie ionisierender Strahlung* ed H Reich (Stuttgart: Teubner)

Rogers D W O and Bielajew A F 1990 Monte Carlo techniques of electron and photon transport for radiation dosimetry *The Dosimetry of Ionizing Radiation, Vol III* ed K R Kase, B E Bjärngard and F H Attix (San Diego, CA: Academic Press) pp 427-539

Sätherberg A and Karlsson M 1998 Calculation of photon energy and dose distributions in a 50 MV scanned photon beam for different target configurations and scan patterns *Med. Phys.* **25** 236-40

Sheikh-Bagheri D 1998 Monte Carlo study of photon beams from medical linear accelerators: optimization, benchmark and spectra *PhD Thesis* Carleton University of Ottawa

Spirou S V and Chui C S 1994 Generation of arbitrary intensity profiles by dynamic jaws or multileaf collimators *Med. Phys.* **21** 1031-41

Stein J 1997 Investigations on intensity modulated treatment techniques in conformal radiotherapy *PhD Thesis* University of Heidelberg

Svensson R, Källman P and Brahme 1994 Analytic solution for the dynamic control of multileaf collimators *Phys. Med. Biol.* **39** 37-61

van Dyk J 1999 Introduction *The Modern Technology of Radiation Oncology* ed J van Dyk (Madison, WI: Medical Physics Publishing) pp 1-17

Webb S 1997 *The Physics of Conformal Radiotherapy: Advances in Technology* (Bristol: Institute of Physics Publishing)

Webb S 2001 *Intensity-modulated radiation therapy* (Bristol: Institute of Physics Publishing)

Werner B L, Das I J and Salk W N 1990 Dose perturbation at interfaces in photon beams: secondary electron transport *Med. Phys.* **17** 212-26

Woo M K and Cunningham J R 1990 The validity of the density scaling method in primary electron transport for photon beams *Med. Phys.* **17** 187-94

Zhu Y and Boyer A 1990 X-ray dose computations in heterogeneous media using 3-dimensional FFT convolution *Phys. Med. Biol.* **35** 351-68

2

Simple beam models for Monte Carlo photon beam dose calculations in radiotherapy

published in
Medical Physics
2000, Vol. 27, No. 12, 2739-2747

Simple beam models for Monte Carlo photon beam dose calculations in radiotherapy

Michael K. Fix, Harald Keller, and Peter Rüegsegger

Institute for Biomedical Engineering, University of Zurich and Swiss Federal Institute of Technology (ETH), Moussonstrasse 18, CH-8044 Zurich, Switzerland

Ernst J. Born

Division of Medical Radiation Physics, Clinic of Radio-Oncology, Inselspital, University of Berne, CH-3045 Berne, Switzerland

Short title: Simple beam models

Abstract

Monte Carlo (code GEANT) produced 6 and 15 MV phase space (PS) data were used to define several simple photon beam models. For creating the PS data the energy of starting electrons hitting the target was tuned to get correct depth dose data compared to measurements. The modeling process used the full PS information within the geometrical boundaries of the beam including all scattered radiation of the accelerator head. Scattered radiation outside the boundaries was neglected. Photons and electrons were assumed to be radiated from point sources. Four different models were investigated which involved different ways to determine the energies and locations of beam particles in the output plane. Depth dose curves, profiles, and relative output factors were calculated with these models for six field sizes from 5 x 5 to 40 x 40 cm^2 and compared to measurements. Model 1 uses a photon energy spectrum independent of location in the PS plane and a constant photon fluence in this plane. Model 2 takes into account the spatial particle fluence distribution in the PS plane. A constant fluence is used again in model 3, but the photon energy spectrum depends upon the off axis position. Model 4, finally uses the spatial particle fluence distribution and off axis dependent photon energy spectra in the PS plane. Depth dose curves and profiles for field sizes up to 10 x 10 cm^2 were not model sensitive. Good agreement between measured and calculated depth dose curves and profiles for all field sizes was reached for model 4. However, increasing deviations were found for increasing field sizes for models 1–3. Large deviations resulted for the profiles of models 2 and 3. This is due to the fact that these models underestimate and overestimate the energy fluence at large off axis distances. Relative output factors consistent with measurements resulted only for model 4.

Key words: Monte Carlo simulation, photon dose calculation, beam model

I. INTRODUCTION

Monte Carlo (MC) simulation of the radiation transport in an absorbing medium currently is the most accurate method for dose calculations in radiotherapy. A drawback of the method is the long computing time, especially in the case of photon beams, to get dose results of reasonable statistical accuracy. However, faster computers and adapted MC methods[1-5] will bring routine MC dose planning to reality in the near future.

To benefit from the potential accuracy of MC dose calculations, equally accurate physical characterization of the radiotherapeutic beam is required. Each photon or electron to be followed in the simulation process needs to be described by its starting location, direction of motion, and its energy. This can be done by supplying a phase space (PS) file containing these data for a large number of particles traversing a given plane perpendicular to the beam axis and above the irradiated body. PS information is most easily and directly assessed by MC simulations of the radiation transport from the target or vacuum exit window through the accelerator treatment head to the PS plane. Early works for photon beams[6,7] aimed at describing energy and angular spectra, investigating their dependence on off axis distance and identifying the main sources of scattered radiation. Later on, MC simulations allowed detailed investigations of scatter sources[8] and treatment head design[9] for photon beams. The BEAM software[10] was extensively used for electron beam modeling.[11-15] Recently, a number of efforts were undertaken to completely characterize photon beams for specific accelerators by their PS data[16] and to compress the size of PS files by the use of beam models.[17]

Storing the PS data normally requires several hundred MBs of disk space per beam. Bearing in mind that several beam qualities and a large number of field sizes are available per accelerator, the need to compress PS data becomes obvious. Therefore, beam models were constructed, which consist in a compact beam data representation and in an algorithm to extract the PS information from this compact representation before or during dose calculations.[17] One way to investigate the accuracy of such a model is to compare directly the original and the reconstructed PS data. Alternatively

and ultimately, the feasibility of a beam model for radiotherapy treatment planning has to be demonstrated by calculating dose distributions and comparing them to measurements. Compact beam representations for electron beams in the form of multiple source models were created using the BEAM code.[11,14] They were shown to be scalable to different machines of the same type.[13]

Photon beam field sizes are continually variable through the use of movable jaws. The jaws themselves represent weak sources of scattered radiation, which mostly contribute less than 1% of the energy fluence.[18] Therefore, photon beam models either take into account the jaws by considering only their shadowing effect[17] or by also modeling the associated weak, field size dependent sources of scattered radiation.[19]

Recently, an attempt was made to simulate the radiation transport through an accelerator head from the target to a plane below the secondary collimator to create and investigate different types of beam models. The corresponding PS data were used to create a detailed multiple source model including the movable collimators as weak sources of scattered radiation.[19] The present work, in contrast, uses the PS data to investigate, under what conditions simpler models can be found, which, nevertheless, allow sufficiently accurate dose calculations within the geometrical beam boundaries. Here, no attempt was made to characterize and model exactly the beam outside the nominal field size. Within the open beam region, however, all beam components, including scattered photons and charged particles, were taken into account. Different possibilities to set the positions and energies of starting particles in the PS plane for MC dose calculations were considered. As a simplifying assumption for all models investigated here, the directions of motion at the start of the photons and electrons were assumed to be consistent with two point sources. In this sense the models can be termed point source models.

II. MONTE CARLO SIMULATIONS AND MEASUREMENTS

A. Description of the models

The radiation transport for a 6 MV photon beam (Varian Clinac 2300 C/D) through both, an accelerator head and a water phantom, was used to calculate dose distributions. The particles were followed through the complete geometry (accelerator head and water phantom) in the same run. Corresponding results for the dose in the water phantom will be referred to as full MC model. Independently, the radiation transport through only the accelerator head was used to produce phase space data of all beam particles traversing a plane perpendicular to the central axis below the secondary collimator for 6 and 15 MV photon beams (Fig. 1). This plane located at the distance of 44.7 cm from the target is called the output plane of the accelerator. For each particle crossing the output plane, an entry in the phase space file was created including charge, energy, direction of motion, and position of the particle.

In all beam models described below, the photons were started from points in the output plane. The direction of motion of a starting photon was given by the line from the central axis point on the upper surface of the target to the position in the output plane. Starting points and energies were sampled from distributions generated from the phase space files. These distributions contained the information about all photons, scattered and unscattered, arriving in the geometrical field size in the output plane. In this work, four models concerning different approaches in sampling starting points and energies were investigated. For model 1, the photon energy was sampled from a spatially averaged energy spectrum which was determined from all photons in the phase space file within the geometrical field size. For the sampling of the starting point, a constant photon fluence was assumed within the geometrical field. Model 2 considered the dependence of the energy spectrum on the radial distance from the central axis of the field while photon fluence was still assumed to be constant. In contrast, in model 3 the spatial photon fluence distribution from the phase space file was taken into account and the energy spectrum of model 1 was used. Finally,

model 4 used both, radially dependent energy spectra together with the spatial photon fluence distribution. Table I gives an overview of the four models.

Manufacturers of clinical accelerators use flattening filters to reduce the intensity in the central parts of the bremsstrahlung beam to reach an approximately constant energy fluence and flat dose profiles across the beam in a specific depth of water. Consequently, the energy spectrum is harder near the beam axis than far away from it. Figure 2 shows the radial dependence of photon fluence, energy fluence, and mean energy determined from the phase space data for the 40 x 40 cm^2 field. Due to the definition of the models, it had to be expected that models 2 and 3 will underestimate and overestimate the energy fluence in the outer beam regions, respectively. Within the geometrical beam size, the energy fluence should be approximately correct for model 1, and it corresponds exactly to the energy fluence calculated from the phase space data for model 4.

Since in the beam models scattered photons of the accelerator head outside the geometric field were neglected and scattered photons within the field were assumed to originate in the target, doses outside the geometrical beam calculated from these models were expected to be underestimated.

In all models, the electron contamination of the beam was included. For the starting electrons in the output plane, a spatially averaged energy spectrum and the spatial fluence distribution determined from all electrons stored in the phase space file within the geometrical field were used. Many investigations have been done to determine the contributors of the contaminating electrons in a photon beam.[20-26] In these studies, the flattening filter was determined[20-24] or confirmed[25,26] as the major contributor of the electron contamination, especially for high energy photon beams. Consequently, the point source of the electrons in all beam models was fixed at the center of the flattening filter, consistent with the work of Hounsell *et al.*[27]

Since all MC calculations should be compared with measurements, the effective accelerating potential of the linear accelerator considered had to be estimated. For this purpose, depth dose curves were calculated for photon beams with an initial energy of the electrons hitting the target of 5, 6, and 7 MeV, respectively. The effective accelerating potential for the 6 MV photon beam was then determined by interpolating the depth dose data and fitting them to the measured depth dose curve for the

10 x 10 cm^2 field. For 15 MV, an initial energy of the electrons was also chosen to reach correct depth dose data compared to measurements for the 10 x 10 cm^2 field.

B. Dose calculations and measurements

In order to investigate the performance and accuracy of the beam models, measured and calculated depth dose curves, lateral dose distributions, and the ratio of the output factor in water to the output factor in air were compared. The measurements were done in a 6 and 15 MV beam of a Varian Clinac 2300 C/D linear accelerator and a 50 x 50 x 40 cm^3 water phantom. A Scanditronix 0.12 cm^3 RK ionization chamber was used to measure the depth dose curves of the 30 x 30, and the 40 x 40 cm^2 field and a Scanditronix p-type shielded Si diode detector for all the other measurements. Field sizes considered were 5 x 5, 10 x 10, 15 x 15, 20 x 20, 30 x 30, and 40 x 40 cm^2 for the 6 MV and 5 x 5, 10 x 10, and 40 x 40 cm^2 for the 15 MV beam. The SSD used was 90 cm for both energies. The corresponding MC simulations for the radiation transport through the accelerator head along with the dose calculations were performed with the MC Code GEANT 3.21 (Release 97a).[28] The suitability of GEANT for application in health physics problems was discussed in Likar *et al.*[29] Additional references and some benchmarks can be found in Urbán.[30] The standard GEANT code used in this work does not offer any variance reduction methods. The dimension of the water phantom used in the dose calculations was 50 x 50 x 20 cm^3 and the kinetic energy cutoff of the electrons and photons was 10 keV in all calculations.

The MC depth dose curves were determined for depths from 0 to 20 cm by scoring the absorbed energy in voxels of 1 x 1 x 0.1 cm^3 around the central axis. To compare calculated and measured relative depth dose data, the decrease of dose has to be characterized. For this purpose and to use the complete statistical information contained in the MC results, exponential fits for the depth dose curves were determined and normalized. The dose value at a given depth can then be evaluated from the fit including its statistical error. To prevent any influence of the dose build up on the exponential fits, the region between 4 and 16 cm water depth for the 6 MV beam and between 6 and 16 cm for the 15 MV beam was used. These fits were done

with the software package MINUIT (Release 96.03)[31] and were normalized to 100% at the surface of the phantom. Relative dose values in 10 cm water depth were compared for each field size. This procedure was used for the simulations, as well as for the measurements.

For the MC calculations of the lateral dose distribution, the absorbed energy was scored in a slab of 48 x 48 x 1 cm^3 at 10 cm water depth perpendicular to the central axis. The grid size in this plane was 0.4 x 0.4 x 1 cm^3 for the full MC model and 0.1 x 0.1 x 1 cm^3 for the beam models. For statistical reasons, the profiles in one direction were averaged over a field size dependent strip centered around the profile crossing the central axis. This strip was about 10% of the field size. For normalization purposes, three to five bins around the central axis of the profiles were averaged.

The output factor in water OF is defined as the dose D per monitor unit MU in a given depth and a given SSD on the central axis of the field relative to the same quantity in a reference field:

$$\mathrm{OF} = \frac{\left.\frac{D}{\mathrm{MU}}\right|^{\mathrm{act}}}{\left.\frac{D}{\mathrm{MU}}\right|^{\mathrm{ref}}}. \qquad (1)$$

The index act refers to the actual situation and the index ref to the reference situation of the measurements (10 x 10 cm^2 field, 10 cm water depth, SSD = 90 cm). Additionally, output factors can be separated into an in-air component $\mathrm{OF_{air}}$, and an in-phantom component $\mathrm{OF_{phan}}$ such that

$$\mathrm{OF} = \mathrm{OF_{air}} \cdot \mathrm{OF_{phan}}. \qquad (2)$$

Thereby, the in-phantom component can be determined from measured total and in-air output factors. MC calculations generally yield doses D per total energy fluence ψ_{tot} in a specific point in free space (e.g., the isocenter). Output factors calculated as ratios of dose per total energy fluence can be compared directly to in-phantom output factors determined from measurements, since

$$\frac{\left.\frac{D}{\Psi_{\mathrm{tot}}}\right|^{\mathrm{act}}}{\left.\frac{D}{\Psi_{\mathrm{tot}}}\right|^{\mathrm{ref}}} = \frac{\left.\frac{D}{\mathrm{MU}}\right|^{\mathrm{act}}}{\left.\frac{D}{\mathrm{MU}}\right|^{\mathrm{ref}}} \cdot \frac{\left.\frac{\mathrm{MU}}{\Psi_{\mathrm{tot}}}\right|^{\mathrm{act}}}{\left.\frac{\mathrm{MU}}{\Psi_{\mathrm{tot}}}\right|^{\mathrm{ref}}} = \frac{\mathrm{OF}}{\mathrm{OF}_{\mathrm{air}}}. \qquad (3)$$

The number of starting electrons for the generation of the phase space files ranged from 3000 Mio for the field size of 5 x 5 cm^2 to 300 Mio for the field size of 40 x 40 cm^2 in the 6 MV case. This led to 2.1 Mio entries in the phase space file for the field size of 5 x 5 cm^2 up to 13.5 Mio entries for the filed size of 40 x 40 cm^2. The total amount of disk space required for all phase space files was about 3 GB, whereas all files containing the distributions for the models together reached only 2.5 MB of disk space. In the case of the 15 MV photon beam, the number of starting electrons for the generation of the phase space files ranged from 1000 Mio for the field size of 5 x 5 cm^2 field to 100 Mio for the field size of 40 x 40 cm^2. Since the number of created photons per electron in the target is higher for higher electron energies and the penetration of the particles increases with increasing energy, the resulting number of entries in the phase space files was about the same.

The number of starting particles for the MC dose calculations was 2500 Mio for the full MC model and 500 Mio for all the beam models (for both energies). To determine the efficiency for a beam model with respect to the full MC model, the required CPU-times for the dose calculations using these models were compared. Thereby, the same statistical accuracy had to be reached for the dose at a depth of 10 cm in water. For the comparison, the formalism described by Jenkins *et al.*[23] was used, which combines the number of starting particles and their statistical accuracy.

III. RESULTS AND DISCUSSION

From the interpolated depth dose data, the effective accelerating potential was calculated to be 6.05 MV. All simulations for creating the phase space files, as well as the full MC model used electrons as starting particle of this initial energy. For the 15 MV photon beam 15.0 MeV electrons as starting particle were used.

For the field sizes of 5 x 5, 10 x 10, 15 x 15, 20 x 20, 30 x 30, and 40 x 40 cm^2 depth dose curves and profiles were measured and calculated. Figure 3 illustrates the depth dose curves for the full MC model and Fig. 4 the corresponding curves for the different beam models including the measured data of the 5 x 5 and 40 x 40 cm^2 field sizes for the 6 MV beam. The full MC model and model 4 showed good agreement with the measurements for all field sizes. Models 1, 2, and 3 led to an overestimation of the decrease of the dose with depth. Although these discrepancies are small for field sizes of up to 15 x 15 cm^2, the deviation increases to about 5% for larger field sizes in 10 cm water depth. Best results were achieved with model 4, where the largest deviation was 0.7% for the 40 x 40 cm^2 field. A deviation of about 2% was also found by Liu *et al.*[34] and Ma *et al.*[35] using a dual source photon beam model or a multiple-subsource model, respectively.

Despite the large number of primary electrons (2500 Mio) used for the full MC model, the corresponding dose data (Fig. 3, Table II) showed larger statistical variations than the data for the beam models (Fig. 4). The reason for that is that the full MC model also considered the transport through all components of the accelerator head in contrast to the beam models. Because of the same number of starting particles (500 Mio) used in models 1–4 for all field sizes, the statistical accuracy was much better for the 5 x 5 cm^2 field than for the 40 x 40 cm^2 field. Table II shows the results of the numerical depth doses evaluated in 10 cm water depth. The too low mean energy around the central axis in model 1 led to significantly lower depth dose values with regard to the full MC simulation and the measurement, especially for large field sizes. Since model 2 used the spatially dependent energy spectrum, higher depth dose values resulted compared with model 1. However, they were still significantly lower than those of the full MC simulation and lower than the measurement for field sizes

larger than 10 x 10 cm^2. Model 3 showed less significant deviations from the full MC model and the measurements, as it considered the spatial dependence of the photon fluence in the output plane. This led to a higher contribution of lateral scattering and resulted in higher depth dose values for model 3 compared with model 1. If, as in model 4, the spatial dependence of the energy distribution was also taken into account, no significant deviation with the full MC model and the measurement was obtained.

The values in Table II were also used to determine the efficiency for the beam models concerning the required CPU-time for the same statistical accuracy. The time to calculate a dose distribution was reduced by a factor of about 13000 for a 5 x 5 cm^2, 120 for a 20 x 20 cm^2 and approximately 80 for a 40 x 40 cm^2 field by the use of beam models compared to the full MC model.

Figure 5 and 6 show the lateral dose distributions in 10 cm water depth for the different models including the corresponding measurements for the 6 MV beam. For better readability, the distributions for the different field sizes were normalized to different central axis values from 20 to 120 and 40 to 100, respectively. The profiles showed more sensitivity to changing the beam characteristics than depth dose curves, as already mentioned in the work of Faddegon *et al.*[36] The full MC model and model 4 led to good agreement with the measurements inside the radiation field. Outside the radiation field, some discrepancies emerged even for the full MC model. This might be due to other components of the accelerator head, which were not implemented in the full MC model. However, the flattening filter, which was shown by Desobry *et al.*[37] to be the main contributor for the fluence outside the geometric field for high energy photon beams, was considered in the full MC simulations. Additional simulations proved, that this is also the case for 6 MV. For small field sizes ($\leq$ 10 x 10 cm^2), all models yielded good results, since in this case the errors in the simulated energy fluence were only small (Fig. 2). These results for model 1 were in accordance with a study of Sixel *et al.*,[38] where a photon source similar to model 1 was used to calculate dose distributions for circular fields up to a field diameter of 3 cm. For larger field sizes (> 20 x 20 cm^2), however, the calculated flat profile for model 1 underestimated the measurements, and models 2 and 3 resulted in great deviations up to 25% for the 40 x 40 cm^2 field, as expected (Fig. 2). Model 4 showed

good agreement with the full MC model for all field sizes. In comparison with the measurement, model 4 described the profiles very well within the radiation field. There, the difference between the calculation with model 4 and the measurement was less than 2% and 2 mm up to a field size of 30 x 30 cm^2 and 3% for the 40 x 40 cm^2 field. The good agreement could be achieved because the scatter radiation of the accelerator head was taken into account. Corresponding results were obtained by Chaney *et al.*,[8] who found, that the calculated profiles were improved especially at the edge of the field compared with measurements, if the head scatter would be included in the calculations. In contrast to the work of Chaney *et al.*,[8] discrepancies occurred starting at the lower penumbra region. In all beam models, the dose values outside the radiation field were less than the corresponding values in the full MC model, because scattered radiation in the output plane outside the geometrical beam was neglected. This is in difference to Chaney *et al.*,[8] where an extended source was used. In the beam models, the dose outside the radiation field is caused only by phantom scatter and therefore increased for increasing field size and depth.

In Fig. 7, the lateral dose distributions for model 4 for two additional depths (1.5 cm and 5 cm) are depicted for the 6 MV beam. The profiles showed good agreement with the measurement within the radiation field and in the higher part of the penumbra. The contribution outside the radiation field was increasing with increasing depth. This behavior is consistent with the assumption that the dose values in this area are only due to phantom scatter.

Figure 8 illustrates the ratios of the output factors OF/OF_{air} for all models and the measurements for the 6 MV beam. The corresponding numerical values are listed in Table III. The free point in space mentioned in Eq. (3) was fixed at the isocenter. Since the determination of the total energy fluence in free space in a specific point by MC calculations showed appreciable statistical uncertainty for the full MC model, the ratios of output factors were expected to be rather inaccurate (Table III). Nevertheless, the general dependence of the calculated ratios of output factors on field size looked reasonable for the full MC model and for better readability the relatively large errors are not depicted in the figure. For all models Eq. (3) was used to calculate the ratio of dose per total energy fluence. The deviation between the calculated and measured ratios of output factors for the full MC model was less than (2.2 ± 5.8)% and for the

beam model 4 less than (1.3 ± 1)%. More complex dual source photon beam models reached an agreement within 1% between calculated and measured output factors in water (different reference conditions and energies).[32,39] No beam model yielded a significant deviation compared to the full MC model because of its relatively large standard deviations. However, the models 1 and 2 led to significant deviations compared to the measurements for all field sizes greater than 15 x 15 cm^2, and model 3 only for the field sizes of 15 x 15 cm^2 and 40 x 40 cm^2. For model 4, no significant deviations occurred. The structure of these results appeared somewhat similar to those of the depth dose values, although the situation is more complex in this case, since the total energy fluence in free space was involved additionally. However, the results for the ratios of output factors were more sensitive to the spatial photon fluence distribution than to the spatial dependence of the energy spectrum. This is in accordance with the work of Sixel *et al.*,[38] where the dose distributions were found to be insensitive to some differences in energy spectra.

On the basis of these results, we also investigated the most promising beam model (model 4) for the 15 MV photon beam. Depth dose curves and lateral dose distributions for field sizes of 5 x 5 cm^2, 10 x 10 cm^2, and 40 x 40 cm^2 were calculated. Figure 9 shows the calculated depth dose curves and the profiles in 10 cm water depth together with the corresponding measurements. The depth dose curves yielded good agreement with the measurements; the numerical data are summarized in Table IV. The calculated dose values at 10 cm water depth were within 0.7% of the measured ones for the field sizes considered. As for the 6 MV photon beam, the calculated profiles were in good agreement with the measurements inside the radiation field, i.e., within 2% in dose and 1 mm shift in the penumbra region. Smaller discrepancies outside the radiation field occurred for this energy. This is due to the fact, that for higher energies the forward scattering increases.

IV. CONCLUSIONS

In this work, several beam models for a 6 MV photon beam, as well as one beam model for a 15 MV photon beam were investigated. On the basis of precalculated phase space files, the models were defined by various combinations of a spatially dependent or independent energy spectrum with either a spatially dependent or independent photon fluence distribution in the output plane for the starting particles (Table I). The use of such a model allowed the reduction of the large disk space required to store a phase space file from a few hundred MB to about 250 kB for one beam model. All models allowed for contamination electrons produced in the head of the linear accelerator.

For small field sizes up to 10 x 10 cm^2, the depth dose curves, the lateral dose distributions, and the ratios of output factors for all models showed good agreement with the full MC model and the measurements for the 6 MV beam. For large field sizes, model 1 led to appreciable deviations in the depth dose values, while the models 2 and 3 resulted in large deviations in the lateral dose distributions near the field edges. Therefore these models are not suitable for accurate MC dose calculations. For all dose calculations model 4 resulted in good agreement compared with the full MC model and measurements for the 6 and 15 MV beam. The ratios of measured output factors for the 6 MV beam were underestimated for models 1 and 2 for large field sizes (> 15 x 15 cm^2), and showed good agreement with the full MC model and the measurements for model 3 (except for 15 x 15 cm^2 and 40 x 40 cm^2) and model 4.

In summary, a radially variable energy spectrum and a spatial photon fluence distribution had to be taken into account (model 4) to reach acceptable results for MC dose calculations of a 6 and 15 MV photon beam. To improve the dose calculation outside the radiation field, information about the fluence distribution and the energy spectrum of the scattered radiation in the output plane outside the geometrical beam could be considered. This could still be implemented in model 4. However, to extend the use of phase space models to more complicated beam geometries (e.g.,

asymmetric and irregular fields), multiple source models are necessary. These models are currently under development.

References

1 H. Neuenschwander and E. J. Born, "A macro Monte Carlo method for electron beam dose calculations," Phys. Med. Biol. **37**, 107-125 (1992).

2 H. Neuenschwander, T. R. Mackie, and P. J. Reckwerdt, "MMC—a high-performance Monte Carlo code for electron beam treatment planning," Phys. Med. Biol. **40**, 543-574 (1995).

3 I. Kawrakow, M. Fippel, and K. Friedrich, "3D electron dose calculation using a Voxel based Monte Carlo algorithm (VMC)," Med. Phys. **23**, 445-457 (1996).

4 M. Fippel, "Fast Monte Carlo dose calculation for photon beams based on the VMC electron algorithm," Med. Phys. **26**, 1466-1475 (1999).

5 D. M. J. Lovelock, C. S. Chui, and R. Mohan, "A Monte Carlo model of photon beams used in radiation therapy," Med. Phys. **22**, 1387-1394 (1995).

6 R. Mohan, C. Chui, and L. Lidofsky, "Energy and angular distribution of photons from medical linear accelerators," Med. Phys. **12**, 592-597 (1985).

7 E. J. Born and R. Mini, "Simulation of Radiation Transport through Treatment Unit Heads: Photon beam results for three medical accelerators," Med. Biol. Eng. Comput. **29**, Suppl. Part 2, 1152 (1991).

8 E. L. Chaney, T. J. Cullip, and T. A. Gabriel, "A Monte Carlo study of accelerator head scatter," Med. Phys. **21**, 1383-1390 (1994).

9 K. van Laere and W. Mondelaers, "Design of field flattening filters for a high-power bremsstrahlung converter by full Monte Carlo simulation," Radiat. Phys. Chem. **49**, 307-317 (1997).

10 D. W. O. Rogers, B. A. Faddegon, G. X. Ding, C. M. Ma, and J. We, "BEAM: A Monte Carlo code to simulate radiotherapy treatment units," Med. Phys. **22**, 503-525 (1995).

11 C. M. Ma, B. A. Faddegon, D. W. O. Rogers, and T. R. Mackie, "Accurate characterization of Monte Carlo calculated electron beams for radiotherapy," Med. Phys. **24**, 401-416 (1997).

12 D. Scora and B. A. Faddegon "Monte Carlo based phase-space evolution for electron dose calculation," Med. Phys. **24**, 177-187 (1997).

13 C. Cris, E. Born, D. Frei, H. Neuenschwander, W. Volken, and R. Mini, "The dose distribution model," Phys. Medica **15**, 174 (1999).

14 C. M. Ma and D. W. O. Rogers, "Beam Characterization: a Multiple-Source Model," National Research Council of Canada Report PIRS 0509C, NCR, Ottawa, 1995.

15 C. M. Ma, "Characterization of computer simulated clinical beams for Monte Carlo radiotherapy treatment planning," Med. Biol. Eng. Comput. **35**, Part 2, 1105 (1997).

16 W. von der Zee and J. Welleweerd, "Calculating photon beam characteristics with Monte Carlo techniques," Med. Phys. **26**, 1883-1892 (1999).

17 A. E. Schach von Wittenau, L. J. Cox, J. P. M. Bergstrom, W. P. Chandler, C. L. Siantar, and R. Mohan, "Correlated histogram representation of Monte Carlo derived medical accelerator photon-output phase space," Med. Phys. **26**, 1196-1211 (1999).

18 A. Ahnesjö, "Collimator scatter in photon therapy beams," Med. Phys. **22**, 267-278 (1995).

19 M. K. Fix, M. Stampanoni, H. Keller, E. Born, R. Mini, and P. Ruegsegger, "A multiple source model for Monte Carlo dose calculations in radiotherapy," Med. Phys. **26**, 1084 (1999).

20 P. L. Petti, M. S. Goodman, T. A. Gabriel, and R. Mohan, "Investigation of buildup dose from electron contamination of clinical photon beams," Med. Phys. **10**, 18-24 (1983).

21 P. L. Petti, M. S. Goodman, J. M. Sisterson, P. J. Biggs, T. A. Gabriel, and R. Mohan, "Sources of electron contamination for the Clinical-35 25-MV photon beam," Med. Phys. **10**, 856-861 (1983).

22 B. Nilsson, "Electron contamination from different materials in high energy photon beams," Phys. Med. Biol. **30**, 139-151 (1985).

23 B. Nilsson and A. Brahme, "Electron contamination from photon beam collimators," Radiother. Oncol. **5**, 235-244 (1986).

24 K. E. Sixel and B. Podgorsak, "Buildup region and depth of dose maximum of megavoltage x-ray beams," Med. Phys. **21**, 411-416 (1994).

25 R. Sjögren and M. Karlsson, "Electron contamination in clinical high energy photon beams," Med. Phys. **23**, 1873-1881 (1996).

26 T. C. Zhu and J. R. Palta, "Electron contamination in 8 and 18 MV photon beams," Med. Phys. **25**, 13-19 (1998).

27 A. R. Hounsell and J. M. Wilkinson, "Head scatter modeling for irregular field shaping and beam intensity modulation," Phys. Med. Biol. **42**, 1737-1749 (1997).

28 Application Software Group Computing and Networks Division, GEANT - Detector Description and Simulation Tool, CERN Program Library Long Writeup W5013, Genf, 1995.

29 A. Likar, T. Vidmar, and B. Pucelj, "Monte Carlo determination of gamma-ray dose rate with the GEANT system," Health Phys. **75**, 165-169, (1998).

30 L. Urbán, "Experimental Benchmarks of GEANT," in *Proceedings of the Fourth International Conference on Calorimetry in High Energy Physics* (World Scientific, Singapore, 1994), pp. 478-492.

31 Application Software Group Computing and Networks Division, MINUIT-Function Minimization and Error Analysis, CERN Program Library Long Writeup D506, Genf, 1995.

32 H. H. Liu, T. R. Mackie, and E. C. McCullough, "Calculating output factors for photon beam radiotherapy using a convolution/superposition method based on a dual source photon beam model," Med. Phys. **24**, 1975-1985 (1997).

33 T. M. Jenkins, W. R. Nelson, and A. Rindi, *Monte Carlo Transport of Electrons and Photons* (Plenum, New York, 1988), Chap. 1.

34 H. H. Liu, T. R. Mackie, and E. C. McCullough, "A dual source photon beam model used in convolution/superposition dose calculations for clinical megavoltage x-ray beams," Med. Phys. **24**, 1960-1974 (1997).

35 C. Ma, E. Mok, A. Kapur, S. Brain, D. Findley, and A. Boyer, "Clinical Implementation of a Monte Carlo Treatment Planning System," Med. Phys. **25**, A128 (1998).

36 B. A. Faddegon, P. O'Brien, and D. L. D. Mason, "The flatness of Siemens linear accelerator x-ray fields," Med. Phys. **26**, 220-228 (1999).

37 G. E. Desobry and A. L. Boyer, "An analytic calculation of the energy fluence spectrum of a linear accelerator," Med. Phys. **21**, 1943-1952 (1994).

38 K. E. Sixel and B. A. Faddegon, "Calculation of x-ray spectra for radiosurgical beams," Med. Phys. **22**, 1657-1661 (1995).

39 M. B. Sharpe, D. A. Jaffray, J. J. Battista, and P. Munro, "Extrafocal radiation: A unified approach to the prediction of beam penumbra and output factors for megavoltage x-ray beams," Med. Phys. **22**, 2065-2074 (1995).

Table I. Overview of the Monte Carlo beam models.

	Spatially averaged energy spectrum	Variable energy spectrum	Constant spatial photon fluence distribution	Variable spatial photon fluence distribution
Model 1	X		X	
Model 2		X	X	
Model 3	X			X
Model 4		X		X

Table II. Values of the fitted depth dose curves for 6 MV in the reference depth of 10 cm in water (SSD = 90 cm). The error of the measurements was about 0.5% and the statistical standard deviation is shown for the simulations.

Field size (cm^2)	Depth dose value in reference depth [%]					
	Measurements	Full Monte Carlo	Model 1	Model 2	Model 3	Model 4
5 x 5	54.47 ± 0.27	55.03 ± 0.47	54.30 ± 0.07	54.70 ± 0.05	54.22 ± 0.09	54.64 ± 0.05
10 x 10	57.68 ± 0.29	57.62 ± 0.66	57.19 ± 0.18	57.21 ± 0.21	57.30 ± 0.16	57.56 ± 0.21
15 x 15	60.12 ± 0.30	60.68 ± 0.65	58.94 ± 0.38	59.53 ± 0.25	59.81 ± 0.19	59.83 ± 0.25
20 x 20	61.47 ± 0.31	61.14 ± 0.55	60.15 ± 0.35	60.22 ± 0.31	60.31 ± 0.41	61.79 ± 0.27
30 x 30	63.45 ± 0.32	62.84 ± 0.78	60.25 ± 0.39	61.53 ± 0.51	61.68 ± 0.35	63.14 ± 0.41
40 x 40	64.46 ± 0.32	64.08 ± 0.69	61.04 ± 0.31	61.20 ± 0.48	62.10 ± 0.58	64.05 ± 0.43

Table III. Ratios of measured output factors in water to measured output factors in air and the same ratios of output factors determined from the MC models using Eq. (3). The measured output factors in water refer to 10 cm water depth and the 10 x 10 cm^2 field was used as reference field. The error of the measurements was about 0.5% and the statistical standard deviation is shown for the simulations.

Field size (cm^2)	OF/OF_{air}					
	Measurements	Full Monte Carlo	Model 1	Model 2	Model 3	Model 4
5 x 5	0.925 ± 0.006	0.930 ± 0.061	0.932 ± 0.002	0.929 ± 0.008	0.917 ± 0.003	0.923 ± 0.004
10 x 10	1.000 ± 0.007	1.000 ± 0.068	1.000 ± 0.009	1.000 ± 0.002	1.000 ± 0.002	1.000 ± 0.002
15 x 15	1.044 ± 0.007	1.054 ± 0.059	1.028 ± 0.003	1.030 ± 0.002	1.015 ± 0.003	1.029 ± 0.008
20 x 20	1.076 ± 0.008	1.070 ± 0.059	1.050 ± 0.005	1.036 ± 0.004	1.081 ± 0.009	1.070 ± 0.003
30 x 30	1.118 ± 0.008	1.095 ± 0.065	1.075 ± 0.008	1.082 ± 0.004	1.123 ± 0.006	1.125 ± 0.002
40 x 40	1.135 ± 0.008	1.129 ± 0.060	1.043 ± 0.007	1.039 ± 0.005	1.109 ± 0.005	1.120 ± 0.008

Table IV. Values of the fitted depth dose curves for 15 MV in the reference depth of 10 cm in water (SSD = 90 cm). The error of the measurements was about 0.5% and the statistical standard deviation is shown for the simulations.

Field size (cm^2)	Depth dose value in reference depth [%]	
	Measurements	Model 4
5 x 5	60.84 ± 0.31	61.20 ± 0.08
10 x 10	63.25 ± 0.32	63.70 ± 0.20
40 x 40	67.28 ± 0.34	67.71 ± 0.38

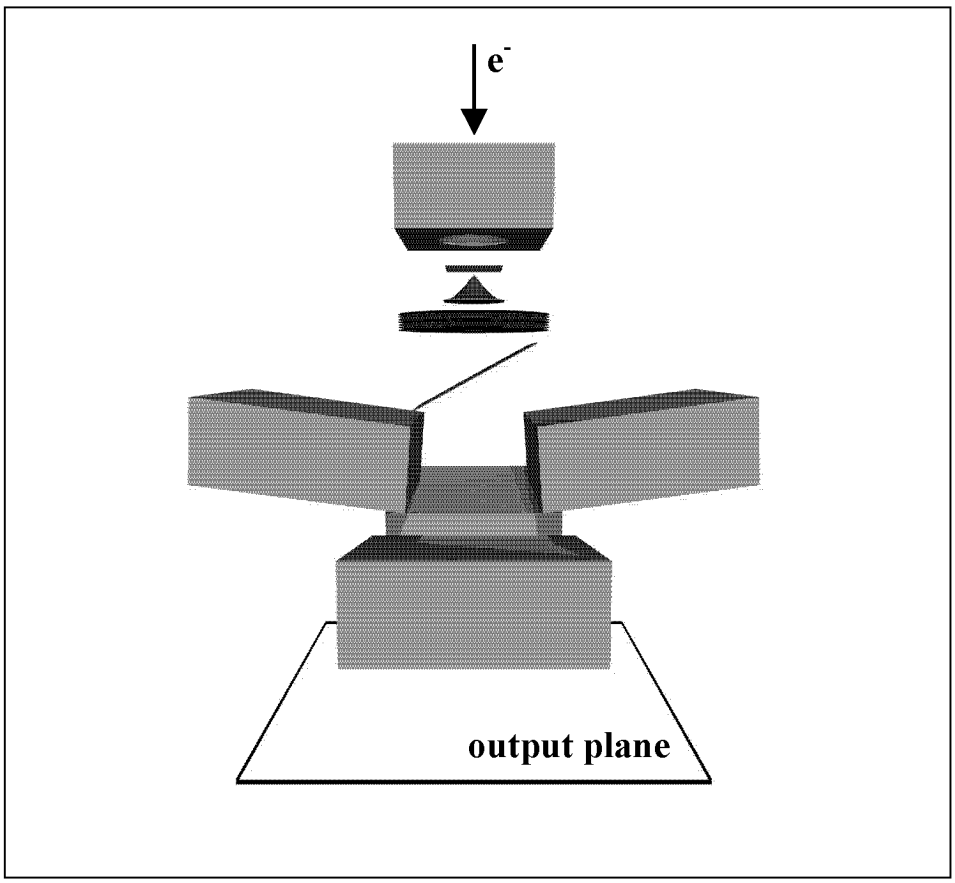

FIG. 1. Components of the accelerator head (Varian Clinac 2300 C/D) implemented in the MC code for the generation of the phase space data. From top to bottom the primary collimator, Be-window, flattening filter, monitor chamber, field light mirror, secondary collimator, and the output plane are illustrated. The arrow shows the starting direction of the electrons which hit the target (here behind the primary collimator). The central axis is equal to the *z* axis.

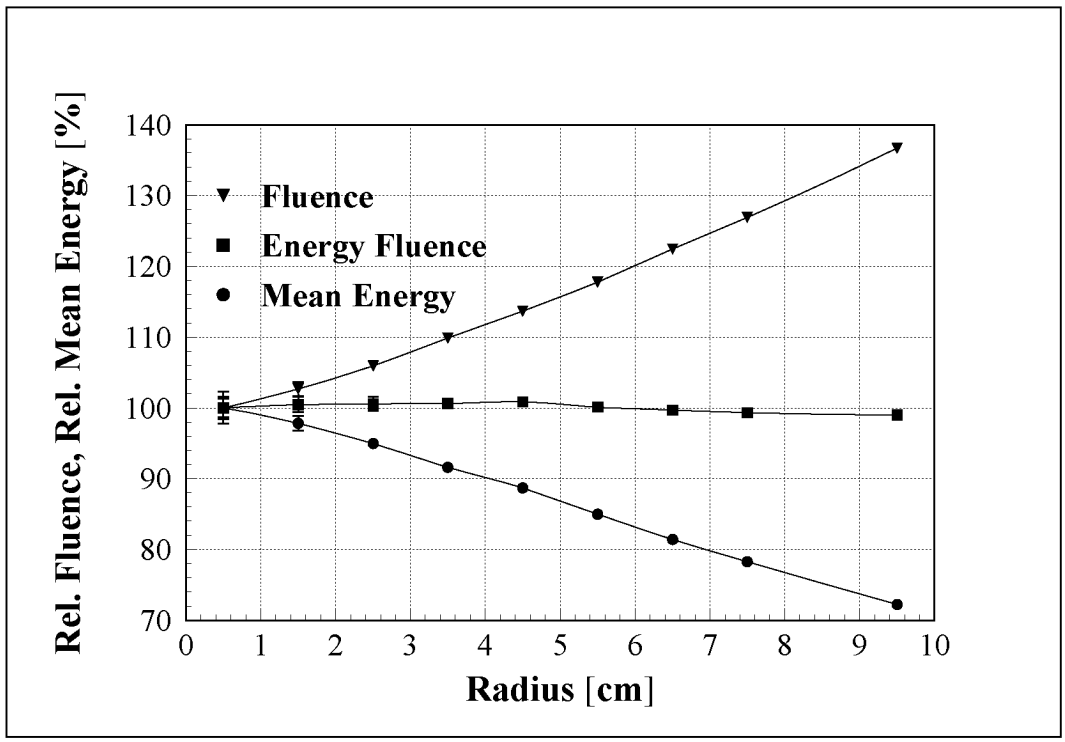

FIG. 2. The radial dependence of the fluence, the energy fluence, and the mean energy in the output plane determined from all photons in the phase space file (6 MV) for the field size of 40 x 40 cm^2 (at isocenter distance). The output plane was located in a distance of 44.7 cm from the target; the source isocenter distance was 100 cm. Each data point was evaluated by averaging over all photons in the corresponding annulus. Most error bars were smaller than the symbol size.

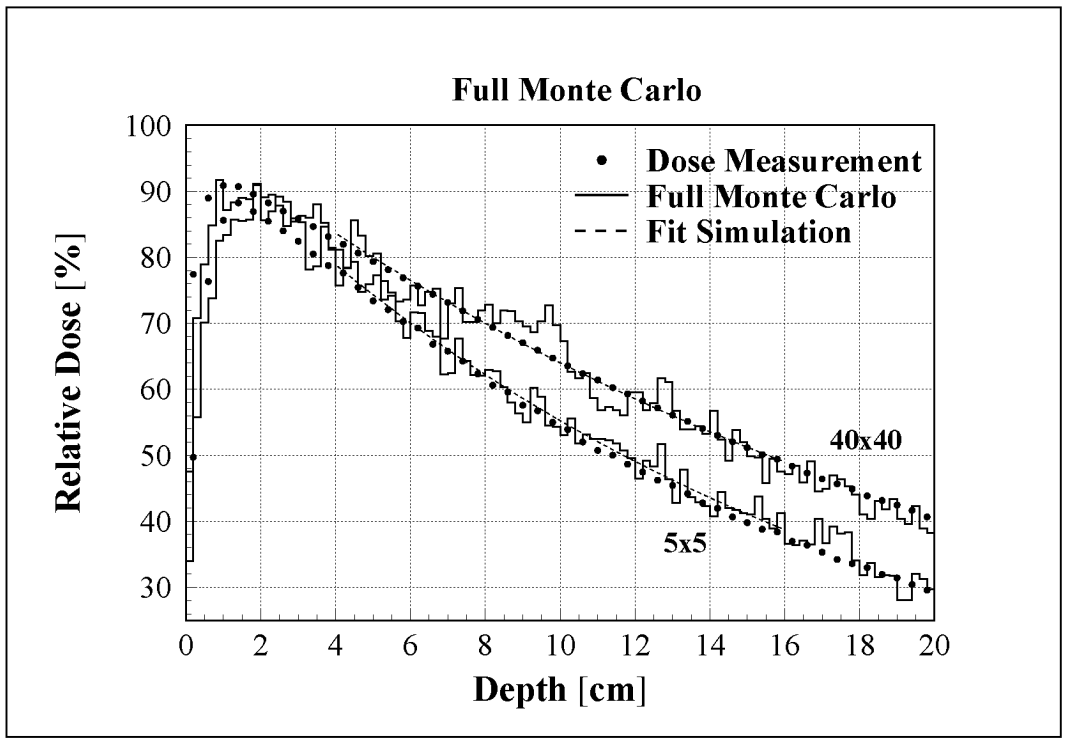

FIG. 3. Depth dose curves of the full Monte Carlo model compared with measured data for two field sizes (5 x 5 and 40 x 40 cm^2; SSD = 90 cm; 6 MV). The fitted curve ranged from 4 to 16 cm water depth and is drawn only for the MC simulation.

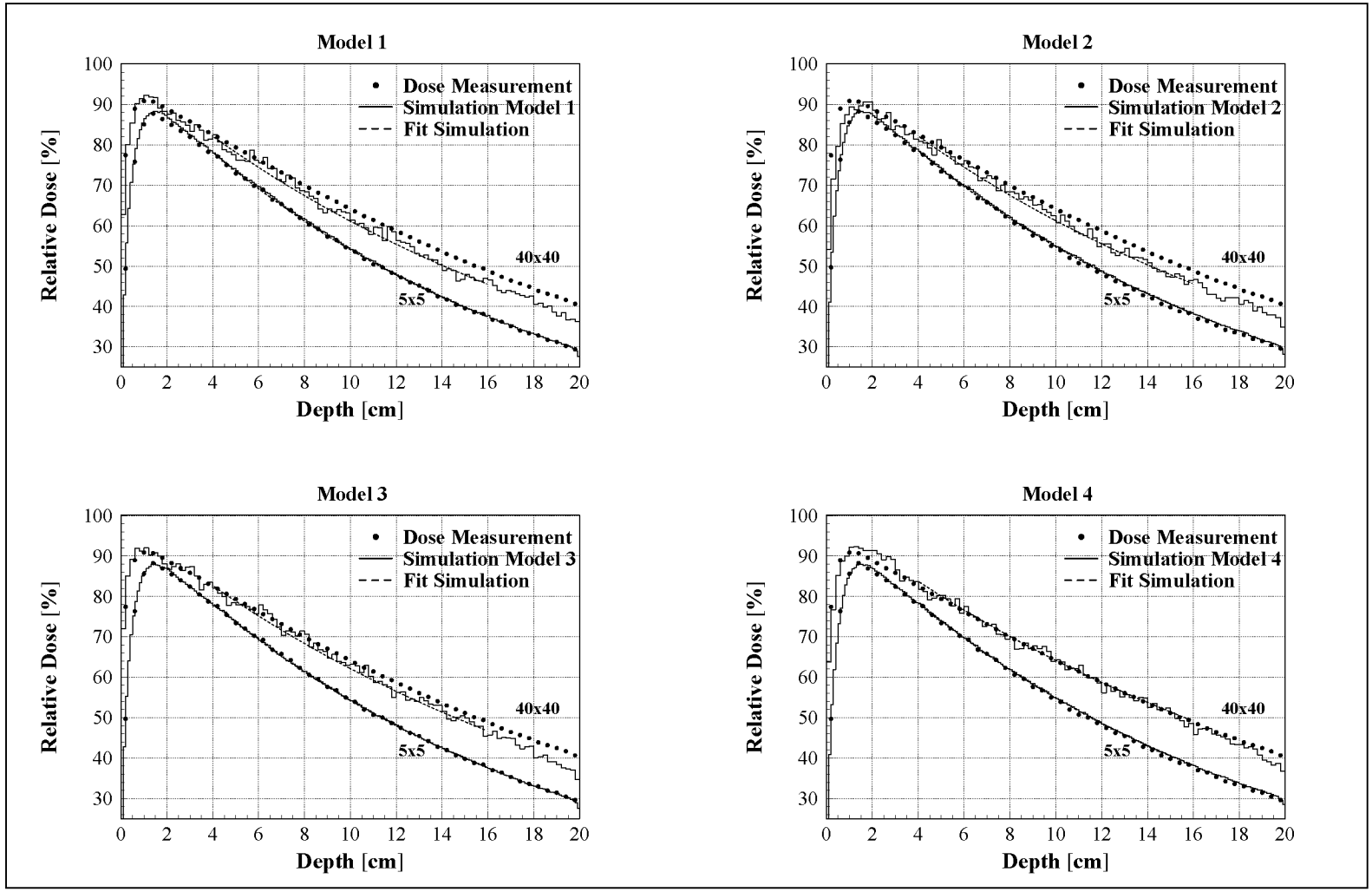

FIG. 4. Depth dose curves for the beam models compared with measured data for two field sizes (5 x 5 and 40 x 40 cm^2; SSD = 90 cm; 6 MV). The fitted curve ranged from 4 to 16 cm water depth and is drawn only for the MC simulation.

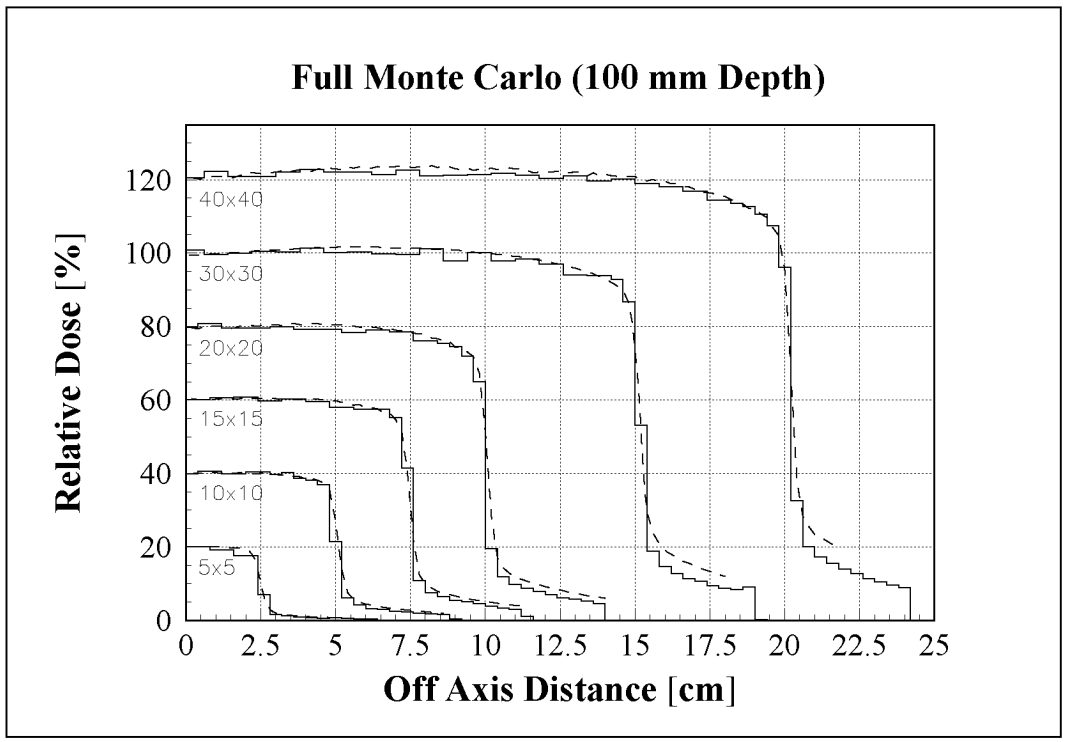

FIG. 5. Lateral dose distributions in 10 cm water depth for the full Monte Carlo model (solid lines) compared with measured data (broken lines) for several field sizes and a 6 MV beam of a Varian Clinac 2300 C/D. The SSD used was 90 cm. For better readability, the distributions for the different field sizes are normalized to different central axis values.

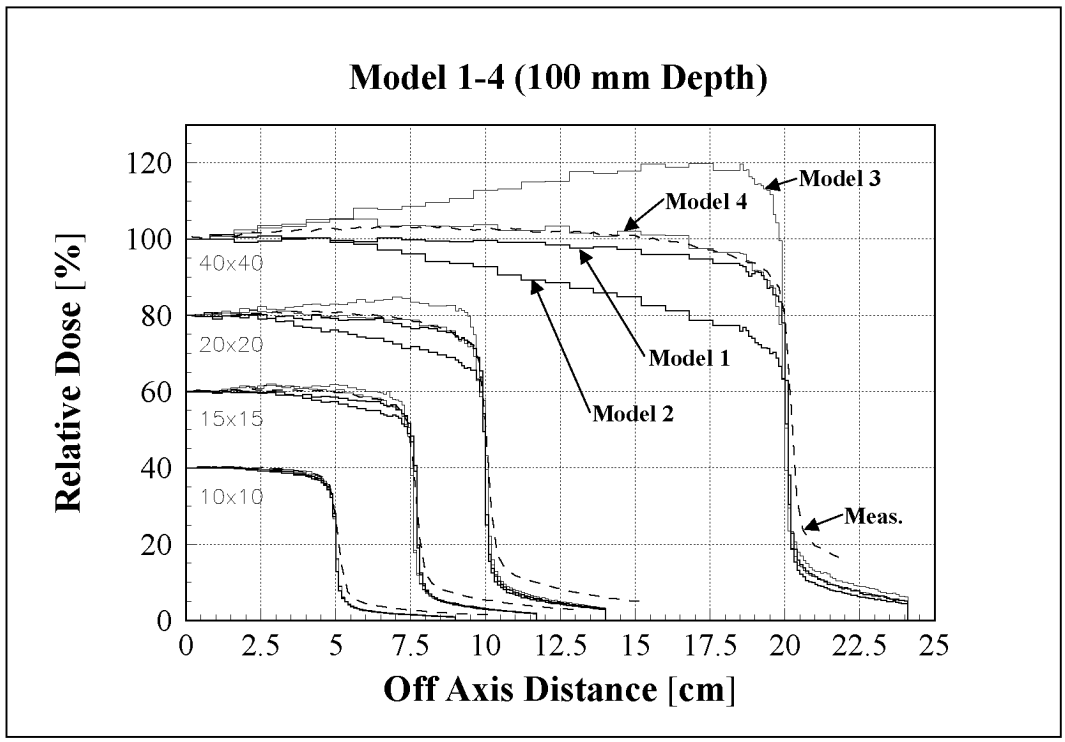

FIG. 6. Lateral dose distributions in 10 cm water depth for the beam models (solid lines) compared with measured data (broken lines) for several field sizes and the 6 MV beam. The SSD used was 90 cm. For better readability, the distributions for the different field sizes are normalized to different central axis values.

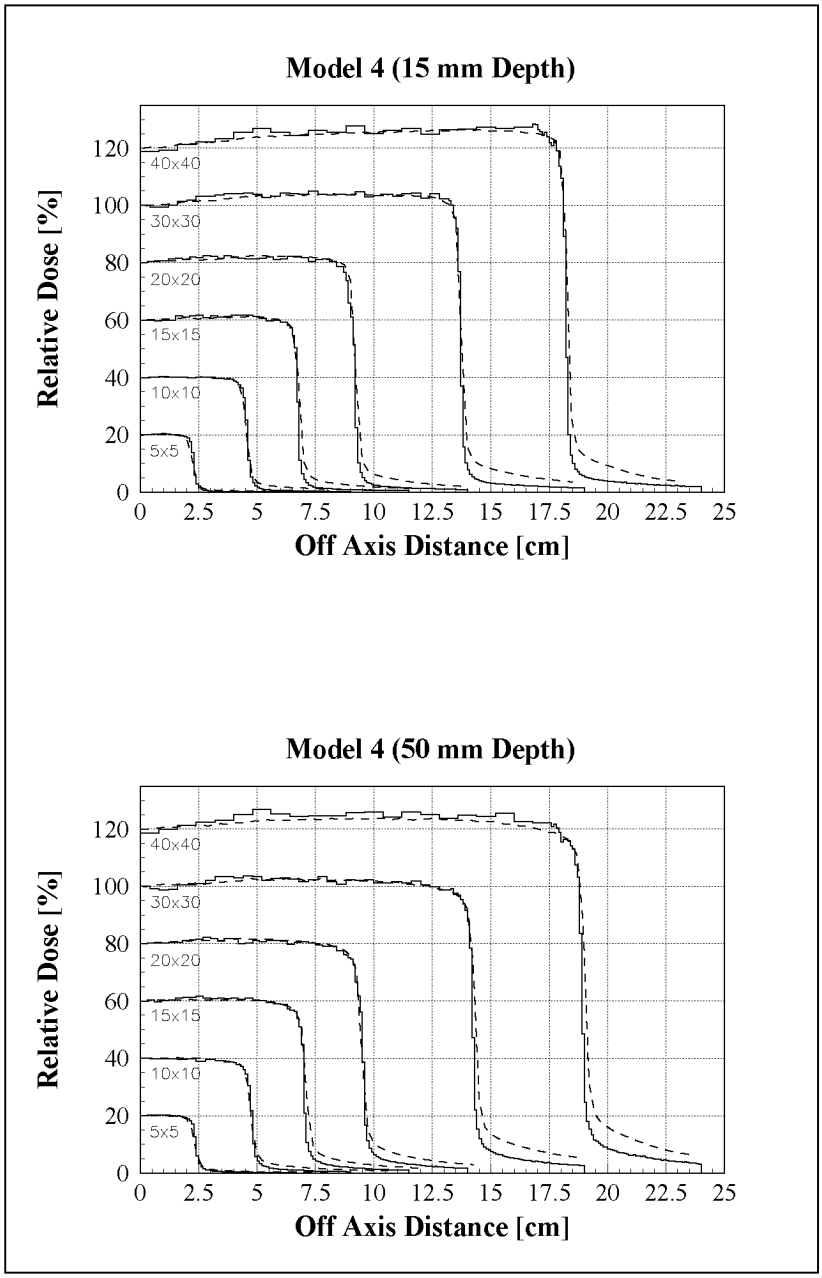

FIG. 7. Lateral dose distributions in 1.5 cm (top) and 5 cm water depth (bottom) for model 4 (solid lines) compared with measured data (broken lines) for several field sizes and the 6 MV beam. For better readability, the distributions for the different field sizes are normalized to different central axis values.

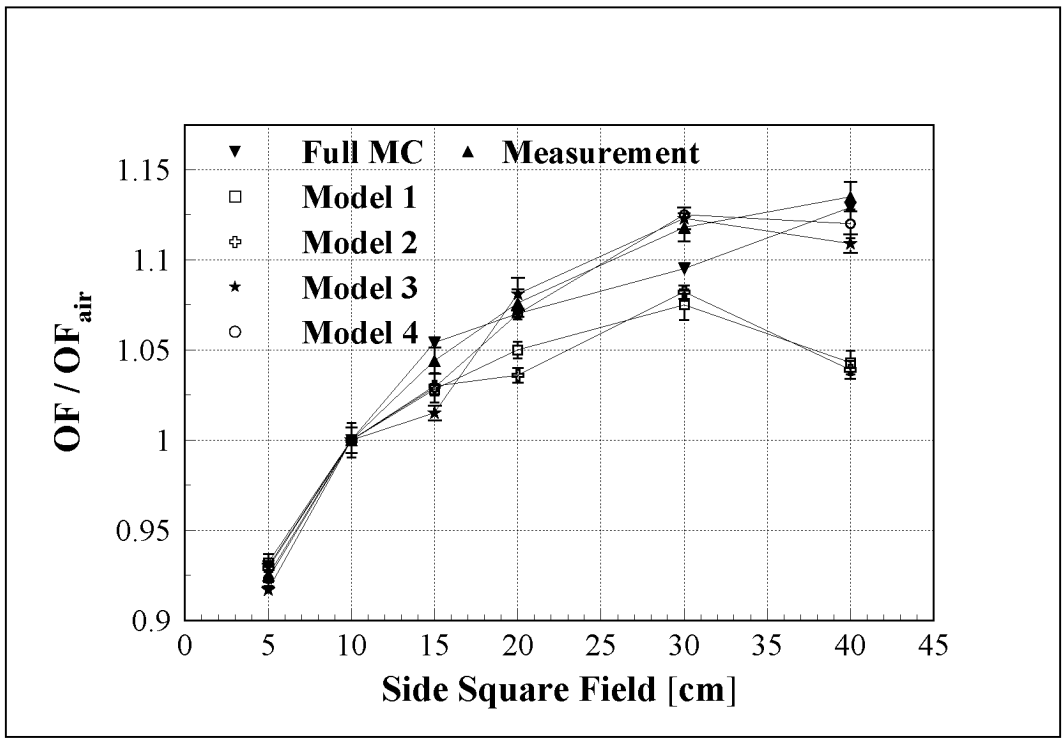

FIG. 8. Ratios of the measured output factors in water to the measured output factors in air vs field size together with the calculations for the MC models for the 6 MV beam. For better readability, the relatively large errors for the full MC model are not drawn in this figure; they are documented in Table III.

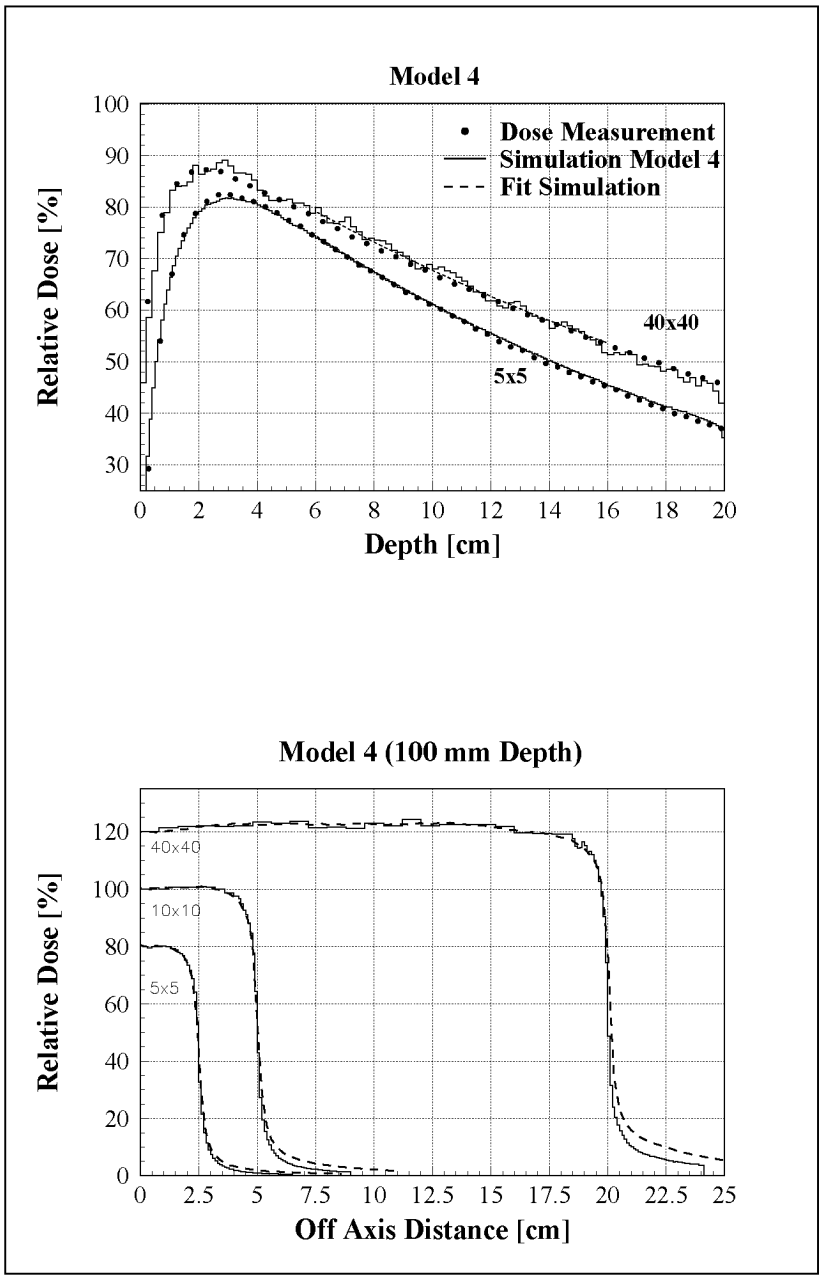

FIG. 9. On the top, depth dose curves for the beam model 4 compared with measured data for two field sizes (5 x 5 and 40 x 40 cm^2; SSD = 90 cm; 15 MV) are illustrated. The fitted curve ranged from 6 to 16 cm water depth and is drawn only for the MC simulation. At the bottom, the lateral dose distributions in 10 cm water depth for the beam model 4 (solid lines) compared with measured data (broken lines) for several field sizes and a 15 MV beam of a Varian Clinac 2300 C/D are shown. The SSD used was 90 cm. For better readability, the distributions for the different field sizes are normalized to different central axis values.

3

A multiple source model for 6 MV photon beam dose calculations using Monte Carlo

published in
Physics in Medicine and Biology
2001, Vol. 46, No. 5, 1407-1427

A multiple source model for 6 MV photon beam dose calculations using Monte Carlo

Michael K. Fix, Marco Stampanoni, and Peter Manser

Institute for Biomedical Engineering, University of Zurich and Swiss Federal Institute of Technology (ETH), Moussonstrasse 18, CH-8044 Zurich, Switzerland

Ernst J. Born, and Roberto Mini

Division of Medical Radiation Physics, Clinic of Radio-Oncology, Inselspital, University of Berne, CH-3045 Berne, Switzerland

Peter Rüegsegger

Institute for Biomedical Engineering, University of Zurich and Swiss Federal Institute of Technology (ETH), Moussonstrasse 18, CH-8044 Zurich, Switzerland

Short title: Multiple source model for MC photon dose calculations

Abstract

A multiple source model (MSM) for the 6 MV beam of a Varian Clinac 2300 C/D was developed by simulating the radiation transport through the accelerator head for a set of square fields using the GEANT Monte Carlo (MC) code. The corresponding phase space (PS) data enabled the characterization of 12 sources representing the main components of the beam defining system. By parametrizing the source characteristics and by evaluating the dependence of the parameters on field size, it was possible to extend the validity of the model to arbitrary rectangular fields which include the central 3 x 3 cm^2 field without additional precalculated PS data. Finally, a sampling procedure was developed in order to reproduce the PS data.

To validate the MSM, the fluence, energy fluence and mean energy distributions determined from the original and the reproduced PS data were compared and showed very good agreement. In addition, the MC calculated primary energy spectrum was verified by an energy spectrum derived from transmission measurements.

Comparisons of MC calculated depth dose curves and profiles, using original and PS data reproduced by the MSM, agree within 1% and 1 mm. Deviations from measured dose distributions are within 1.5% and 1 mm. However, the real beam leads to some larger deviations outside the geometrical beam area for large fields. Calculated output factors in 10 cm water depth agree within 1.5% with experimentally determined data.

In conclusion, the MSM produces accurate PS data for MC photon dose calculations for the rectangular fields specified.

1. Introduction

Accurate dose calculation algorithms are an essential prerequisite for radiation therapy. Many algorithms for photon beams in current commercial treatment planning systems are based on convolution/superposition methods (Mohan *et al* 1986, Mackie *et al* 1985, Boyer and Mok 1985, Ahnesjö *et al* 1992). Energy kernels used in these methods are either extracted from measurements or precalculated by Monte Carlo (MC) simulations and are scaled to account for tissue inhomogeneities. In addition, several approximations are commonly used to reduce calculation time, which lead to appreciable differences between calculations and measurements in the vicinity of tissue inhomogeneities (Woo and Cunningham 1990, Werner *et al* 1990).

MC simulation of the radiation transport is most accurate for dose calculations. The main drawback is the long computing time needed to achieve dose distributions of reasonable statistical accuracy, especially in the case of photon beams. However, faster computers and adapted MC methods (Sempau *et al* 2000, Fippel 1999, Neuenschwander and Born 1992, Keall and Hoban 1996, Kawrakow *et al* 1996, Lovelock *et al* 1995) will bring MC treatment planning to clinical routine in the near future. These adapted MC methods rely on detailed characterization of the beam, usually stored in the phase space (PS) file. For this purpose, the location, the direction of motion and the energy of each particle traversing a plane (here referred to as the output plane) above the body to be irradiated have to be known. These PS data are directly accessible by MC simulation of the radiation transport through the accelerator head. If patient-specific beam modifiers are not included in this transport simulation, PS data are independent of specific patient set-up and can therefore be precalculated.

Early MC simulation work for photon beams investigated the energy and angular spectra as a function of the off-axis distance and the main scatter sources (Mohan *et al* 1985, Born and Mini 1991). Later on, the BEAM software (Rogers *et al* 1995) was extensively used for electron beam modelling (Ma and Rogers 1995, Ma *et al* 1997, Scora and Faddegon 1997) and more recently for photon beams (van der Zee and Welleweerd 1999, Schach von Wittenau *et al* 1999, 2000, Deng *et al* 2000). Several hundred megabytes of disk space per field size are required to store PS data directly.

Bearing in mind that for each accelerator several beam energies and continuously variable jaw positions are used, the need to condense PS data is obvious. Therefore, compact beam data representations and algorithms to extract the PS information before or during dose calculation were investigated (Schach von Wittenau *et al* 1999, 2000, Ma *et al* 1997). For electron beams, these so-called multiple source models were shown to be scalable to different machines of the same type (Cris *et al* 1999).

Photon beam field sizes are continuously variable by the use of movable secondary collimator jaws. The jaws themselves are weak sources of scattered radiation, which mostly contribute less than 1% to the energy fluence (Ahnesjö 1995). Consequently, photon beam models take the jaws into account either by considering only their shadowing effects (Schach von Wittenau *et al* 1999) or by modelling the associated weak, field-size-dependent sources of scattered radiation.

We recently simulated the radiation transport through an accelerator head from the target to an output plane below the secondary collimator and analysed the PS data for a number of square fields. The data were used to investigate the feasibility of simple beam models (Fix *et al* 2000) representing all radiation components by one photon and one electron point source. In the present work, an attempt was made to create a multiple source model (MSM), capable of reproducing PS data in the output plane for arbitrary rectangular fields which include the central 3 x 3 cm^2 field. In contrast to beam models based on PS data in an output plane located above the secondary collimator, this eliminates the need either to separately transport the radiation through the secondary collimator for each rectangular field considered and to store corresponding PS data (van der Zee and Welleweerd 1999, Deng *et al* 2000) or to include this step in the patient-specific treatment planning (Schach von Wittenau *et al* 1999). Therefore, the proposed MSM is expected to be more efficient.

The development of the MSM consisted of the following steps:

(a) Creation of PS data: PS data for a set of square fields are generated in the output plane (figure 1).

(b) Definition of the sources: the PS data were analysed in order to define the sources of the MSM.

(c) Representation of the PS data: histograms were generated to represent and compress the PS data of the sources.

(d) Parameterization for arbitrary rectangular field sizes: an algorithm was developed to extend the validity of the model to arbitrary rectangular fields without precalculation of additional PS data.

(e) Sampling Procedure in the MSM: a sampling procedure to reproduce PS data from source histograms was developed. Thereby, the starting point is sampled from a spatial particle fluence distribution in the output plane. A starting direction is determined together with the spatial distribution of the particle origin of the corresponding head component. Finally, the energy is sampled from an energy distribution defined in the output plane.

For validation purposes, reproduced PS data, depth doses, lateral dose profiles and output factors were calculated using the MSM and compared with original PS data and measurements. In addition, the MC calculated primary energy spectrum was compared to the one derived from transmission measurements.

2. The multiple source model

2.1. Creation of PS Data

A realistic accelerator head of a Varian Clinac 2300 C/D (figure 1) was implemented in the MC code to investigate the characteristics of a 6 MV photon beam. The calculations were performed with the MC code GEANT 3.21 (release 97a) (CERN 1995a) using 10 keV as (kinetic) cut-off energy for the photons and for the charged particles. The simulations started with a pencil beam of primary electrons along the z-axis hitting the target perpendicularly. The energy of the primary electrons was tuned in order to obtain correct depth dose data for the 10 x 10 cm^2 field. For this purpose, depth dose curves for primary electrons with initial energy of 5, 6 and 7 MeV were calculated. Interpolation of these depth dose curves and comparison with measurements led to an effective potential of 6.05 MeV for the primary electrons. The radiation transport was followed through the complete geometry of the accelerator head providing PS data for all particles crossing a plane perpendicular to the beam axis below the secondary collimator at a distance of 44.7 cm from the target (output plane; figure 1). For each particle traversing the output plane the position, the charge, the energy, the direction of motion and the head component of the last interaction were stored. In this way, PS files for a set of eight square fields (3 x 3, 5 x 5, 8 x 8, 10 x 10, 15 x 15, 20 x 20, 30 x 30 and 40 x 40 cm^2 at isocentre distance) were generated.

The number of primary electrons ranged from 4000 million for the 3 x 3 cm^2 field to 400 million for the 40 x 40 cm^2 field. The resulting number of entries in the PS files increases from 1 million to about 15 million for the 3 x 3 cm^2 and 40 x 40 cm^2 field respectively, leading to a total amount of disk space for all PS files of about 4 Gbyte.

2.2. Definition of the sources

Twelve sources were defined on the basis of a detailed analysis of the PS files (table 1). The target was modelled as a line source along the beam axis. This is equivalent to an extended planar source at the target with a radius of about 1 mm, which is consistent with the work of Schach von Wittenau *et al* (1999). The primary collimator was

modelled as a source located on the inner surface of its truncated cone. The planar source which represented the flattening filter was positioned at the lower surface of the filter. Although the creation of electrons and positrons reaching the output plane mainly occurs in the flattening filter, monitor chamber or air, the last interaction takes place mostly in the mirror. For this reason, all electrons and positrons registered in the PS file were summarized in one planar source located on the mirror. The behaviour of the secondary collimator changes with field size which was modelled by defining two planar sources. The sources corresponded to the beam edge defining surface and to the bottom surface of the jaw respectively. Since the relative number of particles in the PS files from the Be window and the monitor chamber together is about 1% for all field sizes, as shown in figure 2, these head components were neglected.

2.3. Representation of the PS data

The weights of both the particle type and the source were determined from the PS data. The latter were based on the relative number of particles from the head components illustrated in figure 2. These data result in an unscatter to scatter ratio of 6.3 (20 x 20 cm^2) and 7.6 (30 x 30 cm^2), where photons from the target are referred to as unscattered photons and all others as scattered photons. These ratios can be compared with data from Dunscombe and Nieminen (1992), who used an empirical model to calculate this ratio, and Chaney *et al* (1994), who found 11.5 (20 x 20 cm^2) and 10.4 (28.6 x 28.6 cm^2) respectively. However, they formed the ratio in a plane at the isocentre, which leads to a lower scatter contribution, and Chaney *et al* (1994) used a kinetic energy cut-off of 100 keV for the electrons. Three different distributions were then determined for each source of the MSM: (a) the spatial distributions of the fluence of the particles in the output plane, (b) the spatial distributions of the points of origin and (c) the energy distributions.

2.3.1. Fluence distributions in the output plane. Spatial fluence distributions in the output plane extracted from the PS data were represented as histograms. Throughout this work the term fluence means planar particle fluence integrated over energy. Figure 3 shows these fluences in the output plane for the target, the primary collimator,

the flattening filter and all jaws of the secondary collimator for the field size of 20 x 20 cm^2. A distinct asymmetry between the upper and lower jaws is visible for the secondary collimator.

2.3.2. Distributions of particle origin. The distribution of spatial origin of particles was obtained by backwards ray tracing all particles reaching the output plane to the surface of the corresponding head component of the linear accelerator. The distributions for all planar sources were represented by two one-dimensional distributions. Figures 4 and 5 illustrate the distributions of spatial origin for the primary and the lower secondary collimator for a field size of 10 x 10 cm^2. Due to the radial symmetry of the truncated cone surface in the primary collimator, the distribution in the plane perpendicular to the beam axis is constant. The other represents the distribution of the points of origin along the beam axis (figure 4). The distribution of spatial origin of the photons reaching the output plane from the lower jaw of the secondary collimator is depicted in figure 5. While figures 5(*a*) and (*b*) show the distributions for the beam edge defining surface, (*c*) and (*d*) correspond to the distributions for the bottom surface of a secondary collimator jaw. One distribution is along the *x*-axis and the other along the beam axis, where the zero point marks the upper edge of the surface considered. For the beam edge defining surface, the brightness of the source increases strongly from the upper edge of the jaw downwards, reaches a maximum and decreases exponentially towards the lower edge of the secondary collimator jaw. This is in contrast to the bottom surface of the secondary collimator. In that case, there is a peak at the lower edge of the jaw with a broad shoulder for regions farther away from the beam defining surface. This shoulder is located where the secondary collimator is exposed to the primary beam.

2.3.3. Energy distributions in the output plane. Figure 6 illustrates some energy spectra for photons of the 40 x 40 cm^2 field in the output plane coming from the target. For these photons, the output plane was divided in several annuli of radial width 1 cm. The three annuli referred to in figure 6 correspond to the radii of 0-1 cm, 6-7 cm and 11-12 cm. The spectral off-axis softening is clearly visible. Similar distributions result for the primary collimator and the flattening filter. For this reason, the radial variation

of the photon energy distribution in the output plane was taken into account in the characterization of the corresponding sources. Similar results were found by Mohan *et al* (1985) and recently by Schach von Wittenau *et al* (1999). In figure 7 the energy spectra for the upper pair of jaws of the secondary collimator for the smallest and the largest field size are depicted. The shape of the energy spectrum in the output plane depends on field size. However, for a fixed field size only a small off-axis dependence of the energy spectrum is observed (see also figure 12). The energy spectra of the charged particles for the 10 x 10 and 40 x 40 cm^2 field are illustrated in figure 8. They show the same behaviour as the photon energy spectra of the secondary collimator. The spectra become harder for decreasing field size. For these sources, the secondary collimator and the mirror, we used an averaged spectrum. This approximation is acceptable because PS analysis showed small differences in the energy distribution outside the geometrical beam for all field sizes (see also figure 12).

2.4. Parameterization for arbitrary rectangular field sizes

In order to extend the validity of the model for arbitrary rectangular fields without producing additional PS data, we developed a fitting algorithm. Since the MSM samples the starting parameters from several distributions, the fitting algorithm has to define analogous distributions for an arbitrary rectangular field from the set of PS data described in the last section. Thus, four distributions have to be determined for each field size and source in the MSM:

(a) the particle type and source distributions;
(b) the spatial distributions of the fluence of the particles in the output plane;
(c) the spatial distributions of the points of origin and
(d) one or more energy distributions.

The whole fitting algorithm was implemented in a PAW (CERN 1995c) routine with the PS files as input and with an output file that contained all distributions required to describe the MSM for any arbitrary field size.

2.4.1. Distribution of particle type and source. The weights of the particle type were stepwise linearly interpolated on the basis of the PS data set obtained from the eight square fields. For a requested rectangular field in the xy plane (x, y), an effective square field size $a = 2xy/(x+y)$ was determined in analogy to the equivalent field size concept in dosimetry (Patomaki 1968). In the same way, the weights of the different sources were determined, except for the secondary collimator. In this case, the number of photons per area directly irradiated on the upper surface of the secondary collimator was interpolated to determine the weights for the sources in the MSM for the rectangular field.

2.4.2. Fluence distributions in the output plane. To interpolate the spatial distribution of fluence in the output plane for sampling the starting point, first the next larger field size (containing the rectangular field) with available PS data was determined. For example, for a field size of 9 x 17 cm^2 the next largest field size is the 20 x 20 cm^2 field. The corresponding fluence distribution of these PS data in the output plane was truncated in each direction according to the geometrical field size considered. The contribution outside the geometrical beam size was then merged using the PS data outside the geometrical field size of the next smaller field, which was enclosed in the rectangular field.

2.4.3. Distributions of particle origin. Several steps were necessary to determine the spatial distributions of the points of origin for each source. All planar sources were represented by two one-dimensional distributions. Each of them was divided into one or more sections, within which the distribution was fitted analytically. The parameters of these fitting functions as well as the positions of the points of intersection were then interpolated linearly between two adjoining PS data sets. In the following, a more detailed description of the fitting algorithm is given on the basis of one example (primary collimator). The planar source modelling the primary collimator shows cylindrical symmetry. Thus, only the one-dimensional distribution of the z-coordinates of the points of origin had to be fitted (figure 4). This distribution was split into two parts by a point of intersection: one part was fitted with a polynomial, the other with an exponential function. The result and the point of the intersection are displayed in figure 4

for the 10 x 10 cm^2 field. The parameters of these functions as well as the location of the point of intersection were interpolated to get the distribution for any arbitrary rectangular field. The distribution of points of origin resulting from this fitting procedure for a 9 x 17 cm^2 field is shown in figure 9 (full curve) together with the result from original PS data (calculated only for purposes of verification) for this field size. This comparison suggests that the fitting and interpolation work very accurately. The method was similarly applied to all other distributions of the points of origin. The fits were performed with the software package MINUIT (release 96.03) (CERN 1995b) and the following fitting functions were used: polynomials of order 0 to 3, exponential functions and Gaussian functions. The resulting analytical functions from the fitting algorithm were transformed into histograms, out of which GEANT can sample directly.

2.4.4. Energy distributions in the output plane. For an arbitrary rectangular field size, two sets of energy spectra of the PS data were used. One set was chosen by considering the largest square field size with available PS data, which was included in the rectangular field. The second set was taken from the data, which belong to the smallest square field size including the rectangular field. Only one set of energy spectra was chosen if the field size considered was identical to a field size for which PS data were available. Based on these energy spectra, the energy of the starting particle was determined during the sampling procedure described in the following section.

2.5. Sampling procedure in the MSM

The particle type and the source of the particle were sampled according to the weights determined from the PS data. The starting point of the particle in the output plane was sampled using the spatial distribution of fluence of the corresponding source. The direction of motion of the starting particle was determined by the line from the point of origin (sampled from the spatial distribution of points of origin of the corresponding source) to the starting position in the output plane. Finally, the energy of the starting particle was sampled from the corresponding energy distribution. Thereby, the spatial variation of the photon energy spectrum in the output plane was taken into account for

the target, the primary collimator and the flattening filter, as described in section 2.3.3. For all other photon sources, as well as for the charged particle source, a spatially averaged energy spectrum was used. In the MSM sampling procedure for an arbitrary field size, the set of energy spectra (see section 2.4.4) depended on the starting point in the output plane. If the starting point was located within the geometrical beam, the energy spectra for the larger squared field size were used. Otherwise, the sampling of the energy of the starting particle was based on the set of energy spectra corresponding to the smaller squared field size. When the set of energy spectra was determined, the energy was sampled from the spectrum which corresponded to the starting point in the output plane.

3. Phase space comparisons

In order to investigate the accuracy of the MSM, PS data were reproduced with the MSM and compared with the original PS data for the 40 x 40 cm^2 (figures 10 to 12) and the 9 x 17 cm^2 (figure 13) field. These comparisons were made for some integral quantities (fluence, energy fluence, mean energies) and not for differential quantities (energy and angle distributions). However, the comparisons of dose distributions discussed in section 4 suggest that the differential fluences are also sufficiently accurate for dose calculations.

To validate the MC simulations the primary energy spectrum of the linear accelerator was measured using an independent method and compared with the MC calculated spectrum (figure 14).

Figure 10 shows the spatial distribution of fluence along the *x*-axis (respectively *y*-axis) of the PS data reproduced with the MSM compared with the original PS data for the 40 x 40 cm^2 field. The contributions of the different components are normalized to the target fluence, which is set to 100% on the beam axis. The plot on the right shows the different contributions in more detail. Unsharp boundaries with a slightly asymmetric shape are seen for the flattening filter. This is due to scattered radiation of this extended source and because distance from the target to the secondary collimator is different for the two pairs of secondary collimator jaws. This effect is partly cancelled out for the primary collimator since this component is located close to the target. The influence of the different target to secondary collimator distance on the spatial distribution of fluence of photons from the secondary collimator along the *x*- and *y*-axis is obvious. The increase along the *y*-axis is due to the smaller distance of the lower pair of secondary collimator jaws to the output plane. The magnitude of this increase is largest for the largest field size. Figures 11 and 12 depict the corresponding information for the distribution of energy fluence and the mean energy respectively. The distribution of energy fluence is very similar to the spatial distribution of fluence except for the target, where the spectral off-axis softening is compensated by an enhanced fluence resulting in a constant energy fluence. As expected from the definition of the MSM, the mean energy is constant for the secondary collimator and the charged particles whereas for the other sources the radially dependence of the energy distribution is

visible. Beam hardening by the secondary collimator jaws leads to an increase of the mean energy outside the geometrical field size. Overall, the MSM describes the distribution of energy fluence and the mean energy correctly.

With the aim of testing the fitting algorithm, original PS data were compared with the reproduced PS data from the MSM for the 9 x 17 cm^2 field. Figure 13 shows the good agreement for the distribution of energy fluence along the *y*-axis, which validates the fitting algorithm. In general the MSM reproduces the original PS data very well and the accuracy of the fluence distribution is better than 1%.

In order to validate the MC simulation of the PS data the MC calculated energy spectrum for target photons was compared with the results obtained from an empirical numerical method introduced by Francois *et al* (1993). They performed the reconstruction of the energy spectrum from transmission data by direct resolution of a matrix system by using spectral algebra. Following the description of the method in Francois *et al* (1993) and Catala *et al* (1995) the reconstruction algorithm was implemented in Mathematica (Stampanoni *et al* 2001). The attenuator as well as the build-up cap for the transmission measurement were made of high-purity aluminium (>99.7%). For this measurement a Farmer ionisation chamber (type 2571) was used for which the chamber response function was determined as described in Catala *et al* (1995). The left plot in figure 14 shows the measured transmission curve, whereas the right one compares the MC calculated spectrum with the reconstructed spectrum. The good agreement within 2.5% (except for the value of the highest energy bin) suggests the correctness of PS data generated with MC.

4. MSM dose calculations

4.1. Methods and materials

Besides comparing PS data from direct simulations with those from the MSM, the feasibility of a beam model for radiotherapy treatment planning has ultimatively to be proven by comparing calculated dose distributions to measurements. Therefore, measured and calculated depth doses as well as dose profiles and output factors were compared for several field sizes.

The measurements were performed for a 6 MV beam with a 50 x 50 x 40 cm^3 water phantom. In addition to the measurements for the set of square field sizes, a 9 x 17 cm^2 field was examined. For field sizes larger than 20 x 20 cm^2 dose was measured by a Scanditronix 0.12 cm^3 RK ionisation chamber and for all other measurements, a Scanditronix p-type shielded Si diode detector was utilized. The source to surface distance (SSD) was set to 90 cm for all measurements and MC calculations.

The corresponding dose calculations were performed with the MC Code GEANT 3.21 (release 99) (CERN 1995a). The related (kinetic) energy cut-off for the photons and the charged particles were 10 keV. The dimension of the water phantom was 50 x 50 x 20 cm^3. The calculated depth dose curves were determined from water depths of 0 to 20 cm in voxels of 1 x 1 x 0.1 cm^3 around the central axis of the beam. The depth dose curves were normalized to 100% at dose maximum. As lateral dose distributions are more sensitive to variations of the beam characteristics than depth dose curves (Fix *et al* 2000, Faddegon *et al* 1999), profiles were calculated in depths of 1.5, 5, 10, and 15 cm. For the MC calculations, a slab of 48 x 48 x 1 cm^3 was positioned to score the absorbed energy in voxels of 0.1 x 0.1 x 1 cm^3 at each depth. For statistical reasons, these profiles were averaged over a strip of about 10% of the field size enclosing the profile. In addition, the three bins of the profiles located around the beam axis were used for normalization.

The output factor in water is defined as the dose D per monitor unit MU in a given depth and at a given SSD on the central axis of the field relative to the same quantity for a reference field. Additionally the output factor can be separated into a head scatter and a phantom scatter component as described in the works of Liu *et al* (1997b) and

Fix *et al* (2000). These components were simulated with the MSM following the work of Liu *et al* (1997b). For comparison with measured data the backscatter to the monitor chamber has to be taken into account (Liu *et al* 2000). This correction factor was calculated by using data from the work of Lam *et al* (1998).

4.2. Results and discussion

4.2.1. Depth dose. Figure 15 illustrates the calculated and measured depth dose curves for the field sizes of 5 x 5, 10 x 10, and 20 x 20 cm^2. The agreement between MSM and measurements is better than 1.5% and between MSM and calculations using the original PS data better than 1%. For field sizes up to 15 x 15 cm^2 the deviations are less than 1%. This is of the same order as in the works of Liu *et al* (1997a) and Ma *et al* (1998,1999) using a dual-photon-beam model or a multiple-subsource model respectively. The dose decrease near a water depth of 20 cm is due to the lack of backscatter, because the depth of the water phantom for the MSM dose calculations is only 20 cm. The statistical accuracy varies from 0.4% (1 SD; 3 x 3 cm^2) to 0.6% (1 SD; 40 x 40 cm^2) in water of 10 cm depth.

The depth dose curve for the 10 x 10 cm^2 field is given in more detail in figure 16. In addition to measured and calculated total depth dose values (MSM and original PS data), all contributions of the different sources of the MSM are depicted. The target supplies more than 90% to the total depth dose values. In the build-up region the electron contamination is about 6%. Zhu and Palta (1998) found 9.0% for an 8 MV beam with an SSD of 100 cm; however, they used a special fit procedure, which in our case leads to 7.5% dose value on the surface. The main scatter contributions below the surface region are due to the flattening filter and the primary collimator.

Analogous MSM calculations and measurements were done for the field size of 9 x 17 cm^2. The calculated depth dose curve agreed within 1% compared with measurements, and consequently the fitting algorithm is confirmed. The electron contamination increases because of the larger field size. This is in agreement with the works of van der Zee and Welleweerd (1999), Zhu and Palta (1998) and Sjögren and Karlsson (1996). Although the dose from the secondary collimator increases, its relative contribution only reaches 0.7%.

4.2.2. Dose profiles. Figure 17 shows profiles in a water depth of 10 cm for several field sizes. For better readability they are normalized to different central axis values ranging from 40% to 140%. All MSM calculated profiles are in very good agreement with profiles calculated with the original PS data. Within the geometrical field size the difference between the MSM calculated profiles and the measurements are within 1.5% and 1 mm. For large field size some discrepancies are visible outside the geometrical beam. Since they also exist for calculated profiles using the original PS data, they must be a consequence of the real beam. In figure 18 profiles in various depths are illustrated for the 10 x 10 cm^2 field. All calculations accurately follow the changes of the measurements in the shape of the profiles. This indicates that the energy distributions of the MSM correctly represent the original PS data and the beam. The deviations between the measured and calculated profiles are less than 1% and 1 mm for all depths. Figure 19 shows the profile of the 10 x 10 cm^2 field for water depths of 1.5 and 15 cm in more detail to illustrate the changes in contributions of the different sources with depth. Apart from the primary radiation of the target, the contribution of the flattening filter is most prominent. For 1.5 cm water depth, the contributions from the flattening filter and the target are of the same order in the lower penumbra region. In addition, the electron contamination is still present. For greater water depths the electron contamination disappears and, due to phantom scatter, the shape of the source profiles flattens off. For a water depth of 15 cm the target is the dominant source even outside the geometrical beam area, the flattening filter is still the main scatter contributor. Similar results were found by Faddegon *et al* (1999) for a Siemens MXE 6 MV beam and by Chaney *et al* (1994) for a 6 MV beam of a Siemens MD2 for small field sizes. The latter showed that for larger fields the primary collimator became the main contributor of scatter radiation for their accelerator. For all depths, the width of the dose profile caused by the primary collimator is less than that of the flattening filter. This is due to the different distances of the primary collimator and the flattening filter from the secondary collimator jaws. Thus, better agreements with measurements can be achieved by using the MSM in the lower penumbra region compared with point source models studied in a previous work (Fix et al 2000).

The results for the profiles in the y-direction of a 9 x 17 cm^2 field are displayed in figure 20 for several depths. The agreement between the calculations and the meas-

urements is very good. Figure 21 illustrates the contributions of the different sources for the depth of 10 cm. The deviation between the measurement and the calculation is less than 1.5% and 1 mm. A more detailed depiction of the profile is shown in figure 22 for the depths of 1.5 and 15 cm. The behaviour of the sources is similar to the case of the 10 x 10 cm^2 field. However, the contribution to the dose from the upper pair of secondary collimator jaws increases to 0.5%, whereas the contribution from the lower pair is negligible. This is due to the rectangular field size, which increases the primary photon fluence incident only on the upper pair of secondary collimator jaws whereas the photon fluence incident only on the lower pair of secondary collimator jaws is reduced. The opposite effect occurs for the 17 x 9 cm^2 field. The results shown in figures 20 to 22 confirm the feasibility of the fitting algorithm.

4.2.3. Output factors. Output factors obtained by measurements are illustrated in figure 23 together with the corresponding values from calculations using the MSM and the original PS data. The deviations between calculated and measured output factors are less than 1.5% and are all within the statistical fluctuations. This is comparable with data from Liu *et al* (1997b) and Sharpe *et al* (1995) yielding an agreement within 1% between calculated and measured output factors for slightly different conditions using a convolution/superposition dose calculation algorithm. For the 9 x 17 cm^2 field the output factor with the MSM is 1.010 ± 0.007 which agrees well with the measured value of 1.012 ± 0.005.

5. Conclusions

In this work we investigated a multiple source model for a 6 MV photon beam of a Varian Clinac 2300 C/D. On the basis of a detailed analysis of the precalculated PS data for a set of square fields, the MSM is defined for arbitrary rectangular field sizes. The use of the MSM reduces requirements on disk space by a factor of 200. It is shown that the MSM reproduces the original PS data very accurately. Furthermore, the PS data were validated by comparing the energy spectrum for target photons with a measured one. The dose distributions and output factors calculated using the MSM are in good agreement with dose distributions resulting from original phase space data and with the measurements.

The applicability to other linear accelerators of the same type and the same nominal accelerating potential can be achieved easily by tuning the energy spectra used in the MSM. For this purpose, the effective potential of the accelerator considered has to be determined as described. Together with the potential used for generating the PS data, a scale factor can be determined to be applied to the energy spectra used in the MSM.

In summary, the MSM enables us to reproduce accurate PS data for MC photon dose calculations. No additional PS data are needed to extend the validity to arbitrary rectangular fields which include the central 3 x 3 cm^2 field. Further developments of the MSM can be made to extend the fitting algorithm to all asymmetric fields. Additional patient-specific beam modifiers such as blocks, wedges, compensators and multileaf collimators can be taken into account using an MC dose calculation algorithm.

References

Ahnesjö A 1995 Collimator scatter in photon therapy beams *Med. Phys.* **22** 267-78

Ahnesjö A, Saxner M and Trepp A 1992 A pencil beam model for photon dose calculation *Med. Phys.* **19** 263-73

Born E J and Mini R 1991 Simulation of radiation transport through treatment unit heads: photon beam results for three medical accelerators *Med. Biol. Eng. Comput.* **29** (suppl part 2) 1152

Boyer A L and Mok E C 1985 A photon dose distribution model employing convolution calculations *Med. Phys.* **12** 169-77

Catala A, Francois P, Bonnet J and Scouarnec C 1995 Reconstruction of 12 MV bremsstrahlung spectra from measured transmission data by direct resolution of the numeric system *AF=T Med. Phys.* **22** 3-10

CERN Application Software Group Computing and Network Division 1995a GEANT–detector description and simulation tool *CERN Program Library Long Writeup* W5013 Genf

——1995b MINUIT–function minimization and error analysis *CERN Program Library Long Writeup* D506 Genf

——1995c PAW–physics analysis workstation *CERN Program Library Long Writeup* Q121 Genf

Chaney E L, Cullip T J and Gabriel T A 1994 A Monte Carlo study of accelerator head scatter *Med. Phys.* **21** 1383-90

Cris C, Born E, Frei D, Neuenschwander H, Volken W and Mini R 1999 The dose distribution model *Phys. Med.* **15** 174

Deng J, Jiang S B, Kapur A, Li J, Pawlicki T and Ma C M 2000 Photon beam characterization and modelling for Monte Carlo treatment planning *Phys. Med. Biol.* **45** 411-27

Dunscombe P B and Nieminen J M 1992 On the field-size dependence of relative output from a linear accelerator *Med. Phys.* **19** 1441-4

Faddegon B A, O'Brien P and Mason D L D 1999 The flatness of Siemens linear accelerator x-ray fields *Med. Phys.* **26** 220-8

Fippel M 1999 Fast Monte Carlo dose calculation for photon beams based on the VMC electron algorithm *Med. Phys.* **26** 1466-75

Fix M K, Keller H, Born E J and Rüegsegger P Simple beam models for Monte Carlo photon dose calculations in radiotherapy *Med. Phys.* **27** 2739-47

Francois P, Catala A and Scouarnec C 1993 Simulation of x-ray spectral reconstruction from transmission data by direct resolution of the numeric system *AF=T Med. Phys.* **20** 1695-703

Kawrakow I, Fippel M and Friedrich K 1996 3D electron dose calculation using a voxel based Monte Carlo algorithm (VMC) *Med. Phys.* **23** 445-57

Keall P J and Hoban P W 1996 Super-Monte Carlo: a 3-D electron beam dose calculation algorithm *Med. Phys.* **23** 2023-34

Lam K L, Muthuswamy S and Haken R K T 1998 Measurement of backscatter to the monitor chamber of medical accelerators using target charge *Med. Phys.* **25** 334-8

Liu H H, Mackie T R and McCullough E C 1997a A dual source photon beam model used in convolution/superposition dose calculations for clinical megavoltage x-ray beams *Med. Phys.* **24** 1960-74

——1997b Calculating output factors for photon beam radiotherapy using a convolution/superposition method based on a dual source photon beam model *Med. Phys.* **24** 1975-85

——2000 Modeling photon output caused by backscattered radiation into the monitor chamber from collimator jaws using a Monte Carlo technique *Med. Phys.* **27** 737-44

Lovelock D M J, Chui C S and Mohan R 1995 A Monte Carlo model of photon beams used in radiation therapy *Med. Phys.* **22** 1387-94

Ma C M, Faddegon B A, Rogers D W O and Mackie T R 1997 Accurate characterization of Monte Carlo calculated electron beams for radiotherapy *Med. Phys.* **24** 401-16

Ma C M, Mok E, Kapur A, Brain S, Findley D and Boyer A 1998 Clinical implementation of a Monte Carlo treatment planning system *Med. Phys.* **25** A128

Ma C-M, Mok E, Kapur A, Pawlicki T, Findley D, Brain S, Forster K and Boyer A L 1999 Clinical implementation of a Monte Carlo treatment planning system *Med. Phys.* **26** 2133-43

Ma C M and Rogers D W O 1995 Beam characterization: a multiple-source model *National Research Council of Canada Report* PIRS 0509C (Ottawa: NCR)

Mackie T R, Scrimger J W and Battista J J 1985 A convolution method of calculating dose for 15 MeV x rays *Med. Phys.* **12** 188-96

Mohan R, Chui C and Lidofsky L 1986 Differential pencil beam dose computation model for photons *Med. Phys.* **13** 64-73

Mohan R, Chui C and Lidofsky L 1985 Energy and angular distribution of photons from medical linear accelerators *Med. Phys.* **12** 592-97

Neuenschwander H and Born E J 1992 A macro Monte Carlo method for electron beam dose calculations *Phys. Med. Biol.* **37** 107-25

Patomaki L K 1968 The equivalent field principle and its use in beam therapy dose calculations *Br. J. Radiol.* **41** 381-3

Rogers D W O, Faddegon B A, Ding G X, Ma C M and We J 1995 BEAM: a Monte Carlo code to simulate radiotherapy treatment units *Med. Phys.* **22** 503-25

Schach von Wittenau A E, Cox L J, Bergstrom P M, Chandler W P, Siantar C L and Mohan R 1999 Correlated histogram representation of Monte Carlo derived medical accelerator photon-output phase space *Med. Phys.* **26** 1196-211

Schach von Wittenau A E, Bergstrom P M and Cox L J 2000 Patient-dependent beam-modifier physics in Monte Carlo photon dose calculations *Med. Phys.* **27** 935-47

Scora D and Faddegon B A 1997 Monte Carlo based phase-space evolution for electron dose calculation *Med. Phys.* **24** 177-87

Sempau J, Wilderman S J and Bielajew A F 2000 DPM, a fast, accurate Monte Carlo code optimized for photon and electron radiotherapy treatment planning dose calculations *Phys. Med. Biol.* **45** 2263-391

Sharpe M B, Jaffray D A, Battista J J and Munro P 1995 Extrafocal radiation: a unified approach to the prediction of beam penumbra and output factors for megavoltage x-ray beams *Med. Phys.* **22** 2065-74

Sjögren R and Karlsson M 1996 Electron contamination in clinical high energy photon beams *Med. Phys.* **23** 1873-81

Stampanoni M, Fix M K, Francois P and Rüegsegger P 2001 Computer algebra for x-ray spectral reconstruction between 6 and 25 MV *Med. Phys.* **28** 325-27

van der Zee W and Welleweerd J 1999 Calculating photon beam characteristics with Monte Carlo techniques *Med. Phys.* **26** 1883-92

Werner B L, Das I J and Salk W N 1990 Dose perturbation at interfaces in photon beams: secondary electron transport *Med. Phys.* **17** 212-26

Woo M K and Cunningham J R 1990 The validity of the density scaling method in primary electron transport for photon beams *Med. Phys.* **17** 187-94

Zhu T C and Palta J-R 1998 Electron contamination in 8 and 18 MV photon beams *Med. Phys.* **25** 12-19

Table 1. List of all sources defined in the MSM. Each jaw of the secondary collimator was defined as two planar sources, corresponding to the beam defining surface and to the bottom surface of the jaw respectively. Electron and positron contamination in the beam was considered by defining one source at the bottom surface of the mirror.

Head component	Type of source	Number of source(s)	Particle type
Target	Line	1	Photons
Primary collimator	Planar	1	Photons
Flattening filter	Planar	1	Photons
Mirror	Planar	1	Electrons/positrons
Secondary collimator X1	Planar	2	Photons
Secondary collimator X2	Planar	2	Photons
Secondary collimator Y1	Planar	2	Photons
Secondary collimator Y2	Planar	2	Photons

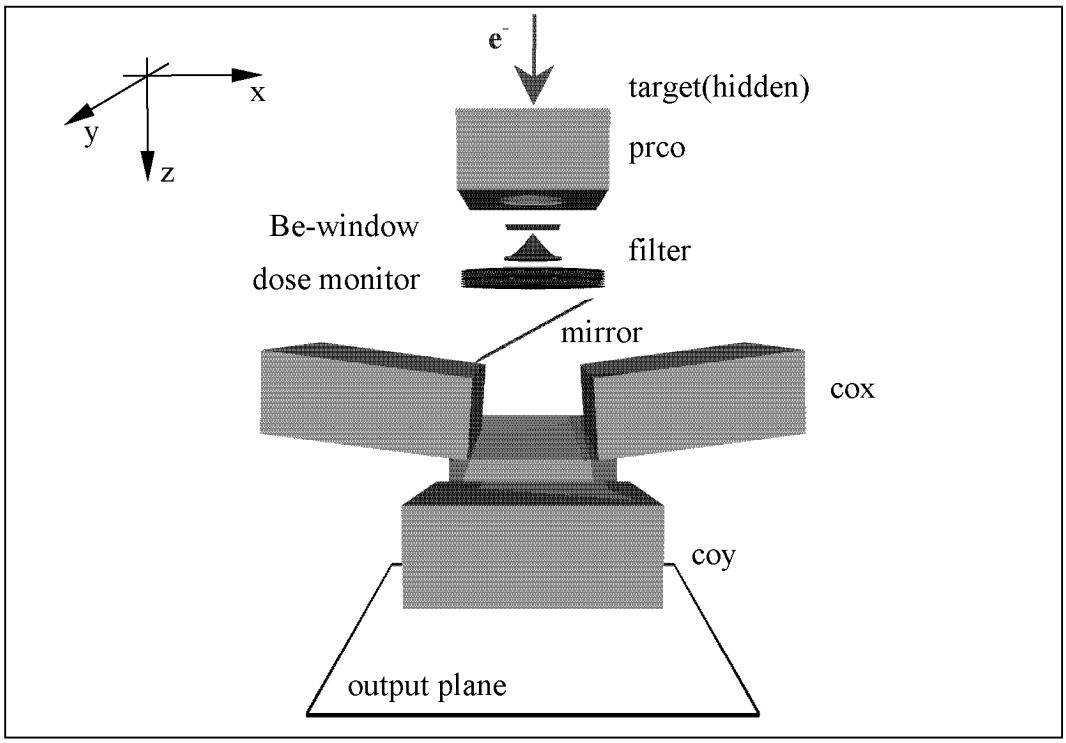

FIG. 1. Geometry of the accelerator head implemented in the MC code to generate the phase space data (prco = primary collimator, filter = flattening filter, cox = the upper pair of jaws of the secondary collimator, coy = the lower pair of jaws of the secondary collimator). An electron pencil beam hit the target at the beam axis. Below the two pairs of secondary collimator jaws, the output plane was located perpendicularly to the beam axis and used as the scoring plane for the phase space files.

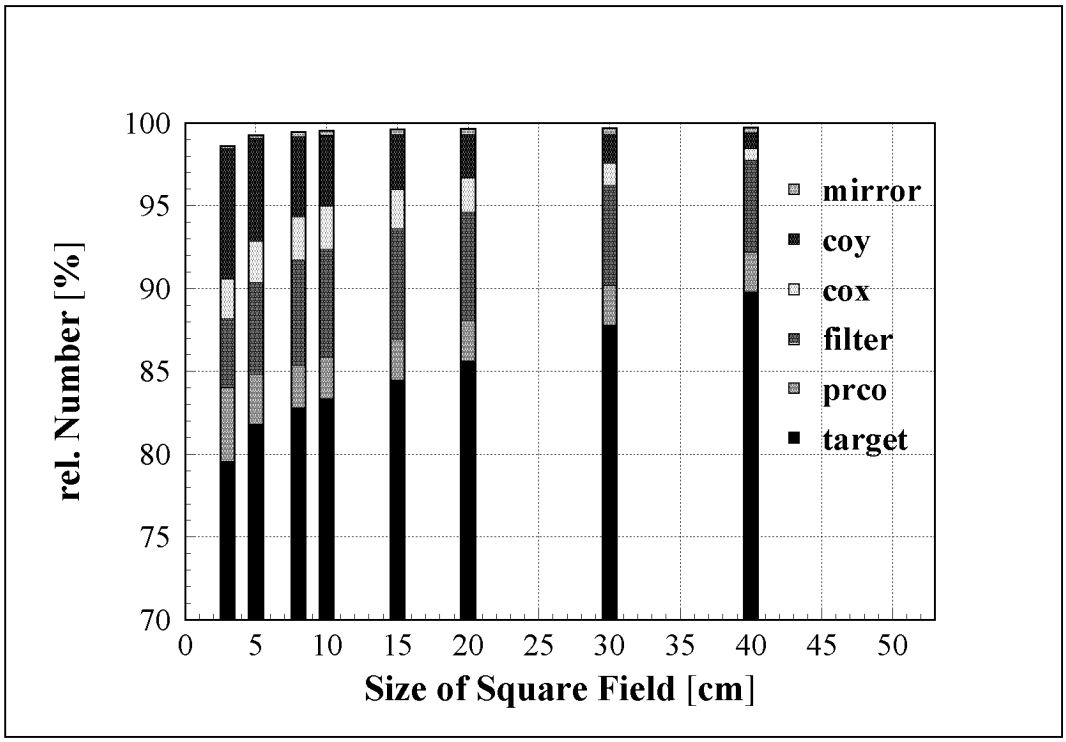

FIG. 2. Relative number of particles from the sources defined in the MSM resulting from the phase space data in the output plane. The contribution of the primary radiation (target) was increasing with increasing field size, whereas the scatter contribution was decreasing (especially the secondary collimator scatter). The remaining part up to 100% is due to the contributions from other head components, such as the dose monitor or the Be window. These data were used to determine the weights of the different sources in the MSM. (Abbreviations as in caption to figure 1.)

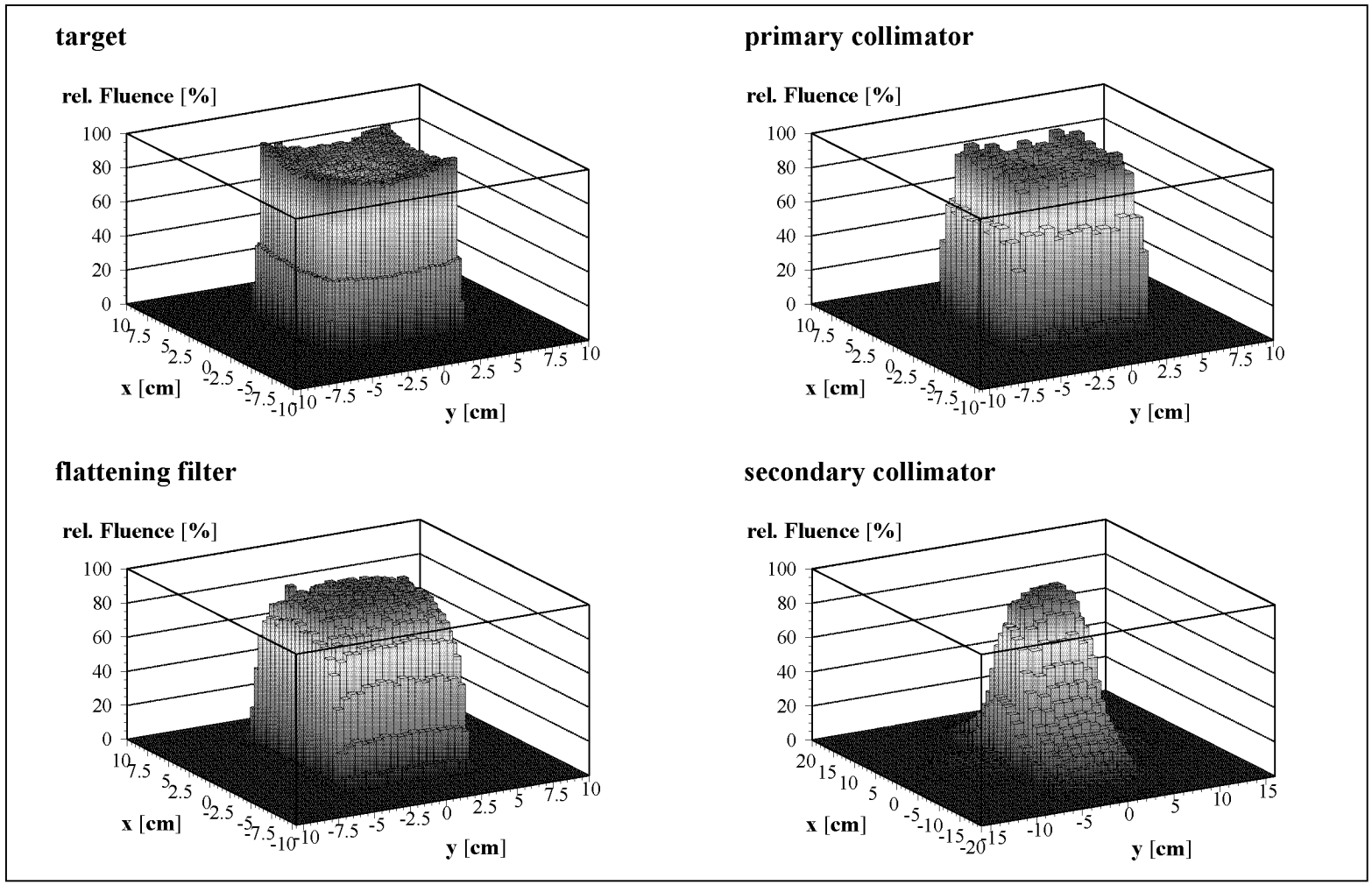

FIG. 3. Histograms representing the spatial photon fluence distributions of the phase space data in the output plane for the 20 x 20 cm^2 field for the target, the primary collimator, the flattening filter, and the secondary collimator (sum of the contributions of all jaws).

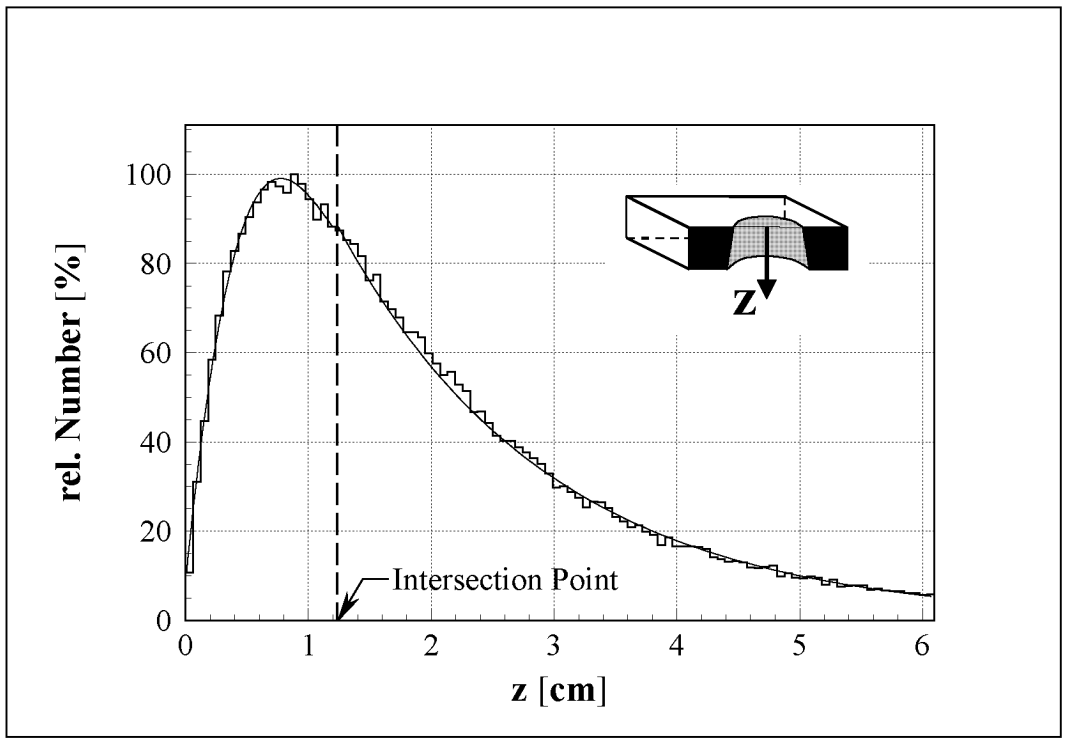

FIG. 4. The spatial distribution of points of origin of the planar photon source of the primary collimator was described as two one-dimensional distributions. The figure shows the distribution of the z coordinates of the points of origin of the particles for the 10 x 10 cm^2 field ($z = 0$ marks the upper surface of the primary collimator). The two fitting functions as well as the point of intersection were used in the fitting algorithm described in section 2.4.3.

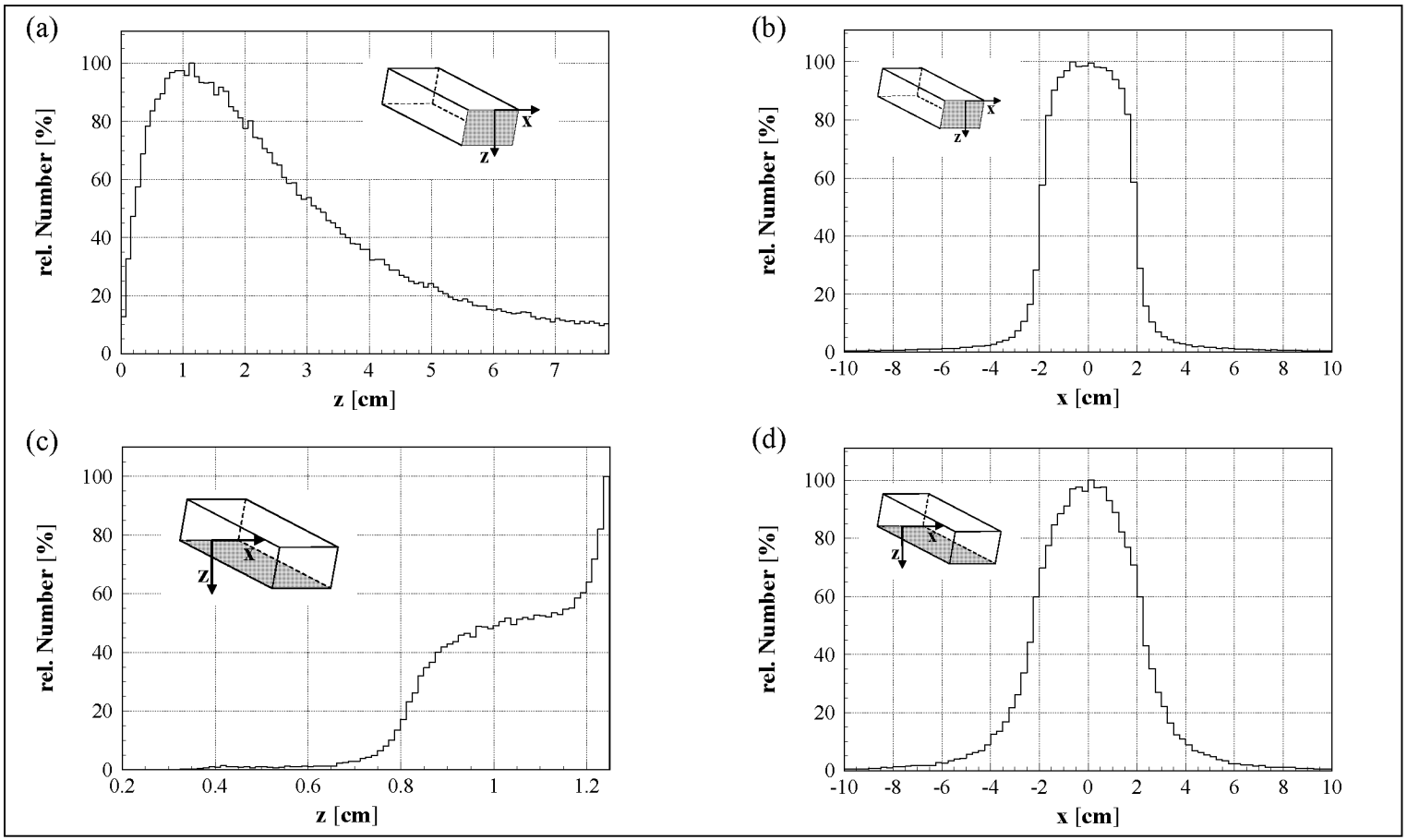

FIG. 5. The spatial distributions of points of origin of the two planar sources of the lower pair of secondary collimator jaws for the 10 x 10 cm^2 field are displayed as two one-dimensional distributions in the z and x-direction respectively. (*a*), (*b*) The distributions for the beam edge defining surface ($z = 0$ marks of the upper edge of the beam defining surface). (*c*), (*d*) The same for the bottom surface of the jaws ($z = 0$ marks the upper edge of the bottom surface). The shoulder shown in (*c*) is due to the opening of the truncated cone of the primary collimator.

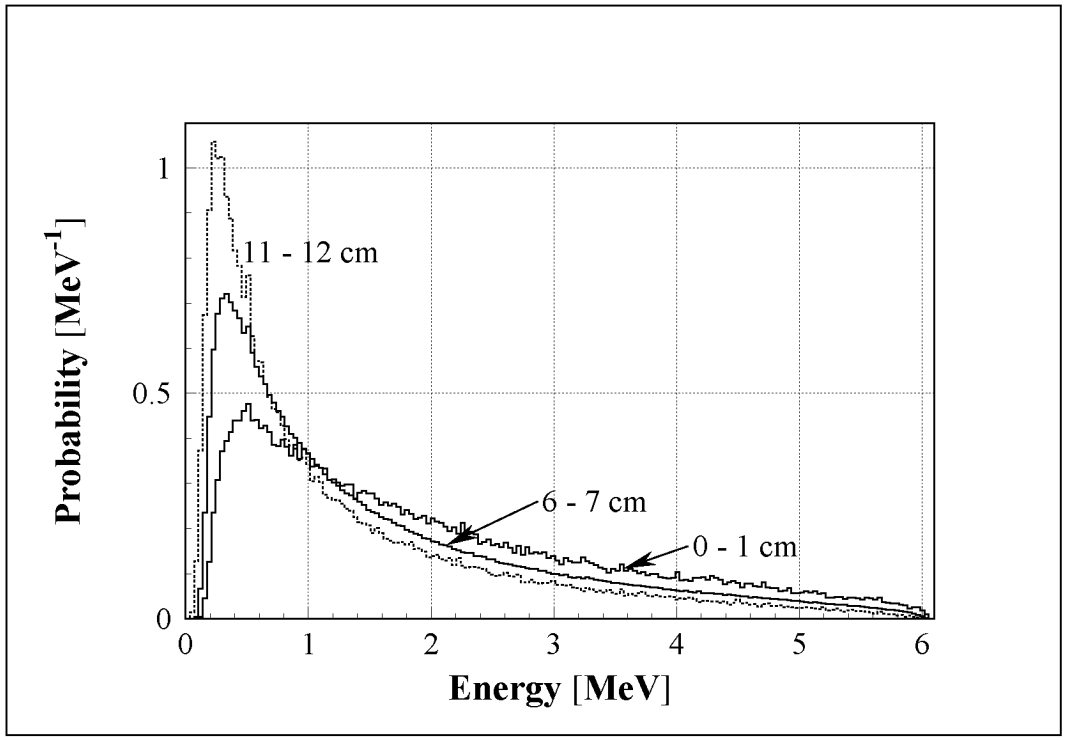

FIG. 6. Three examples of photon energy spectra in different annuli around the beam axis in the output plane coming directly from the target for the 40 x 40 cm^2 field. The off-axis softening of the beam is obvious.

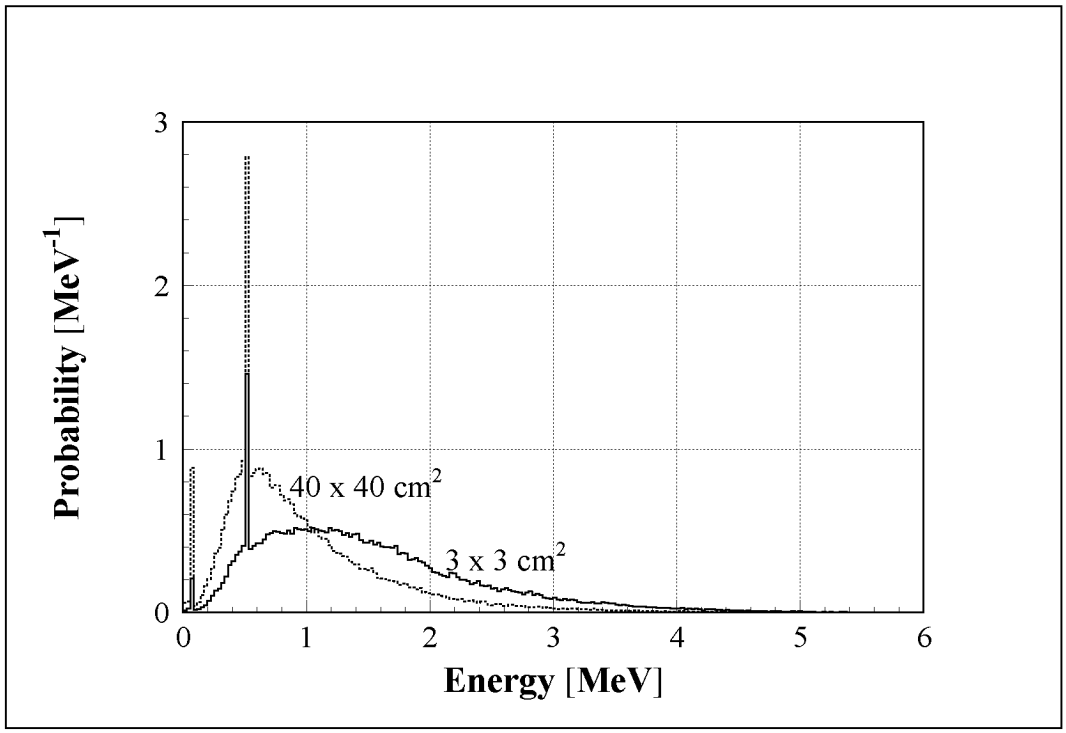

FIG. 7. Energy spectra of photons reaching the output plane directly from the upper pair of jaws of the secondary collimator for two different field sizes. The peaks in the spectra are due to characteristic radiation and annihilation radiation respectively.

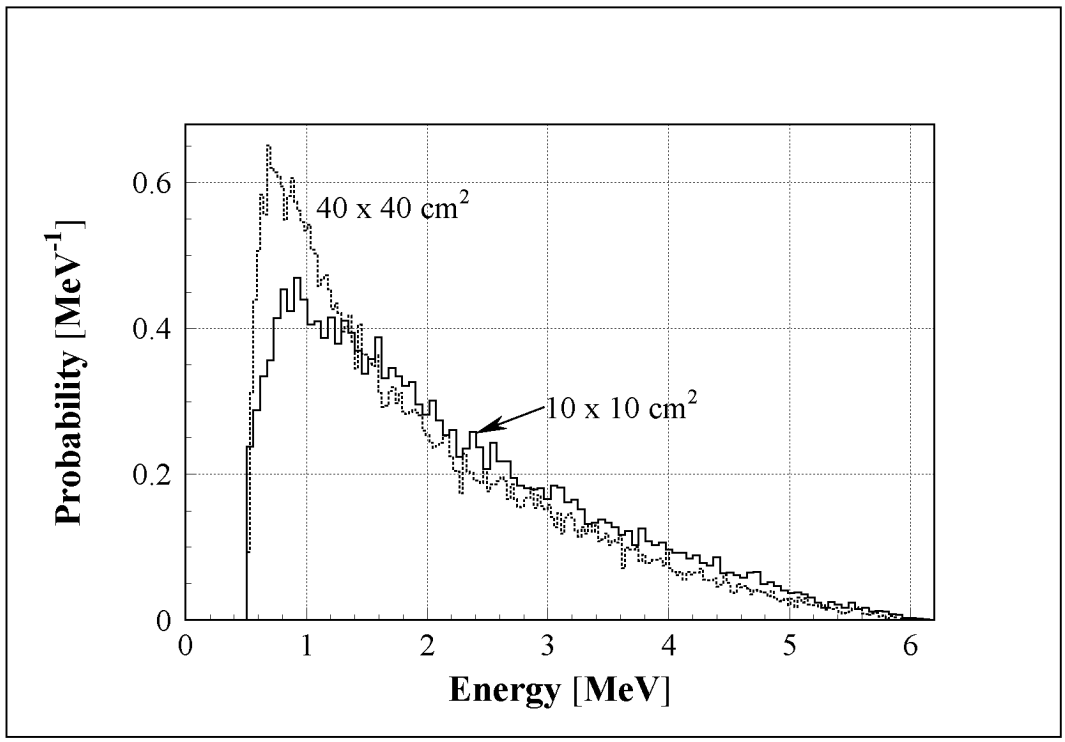

FIG. 8. Energy spectra (total energy) of the charged particles reaching the output plane for two different field sizes.

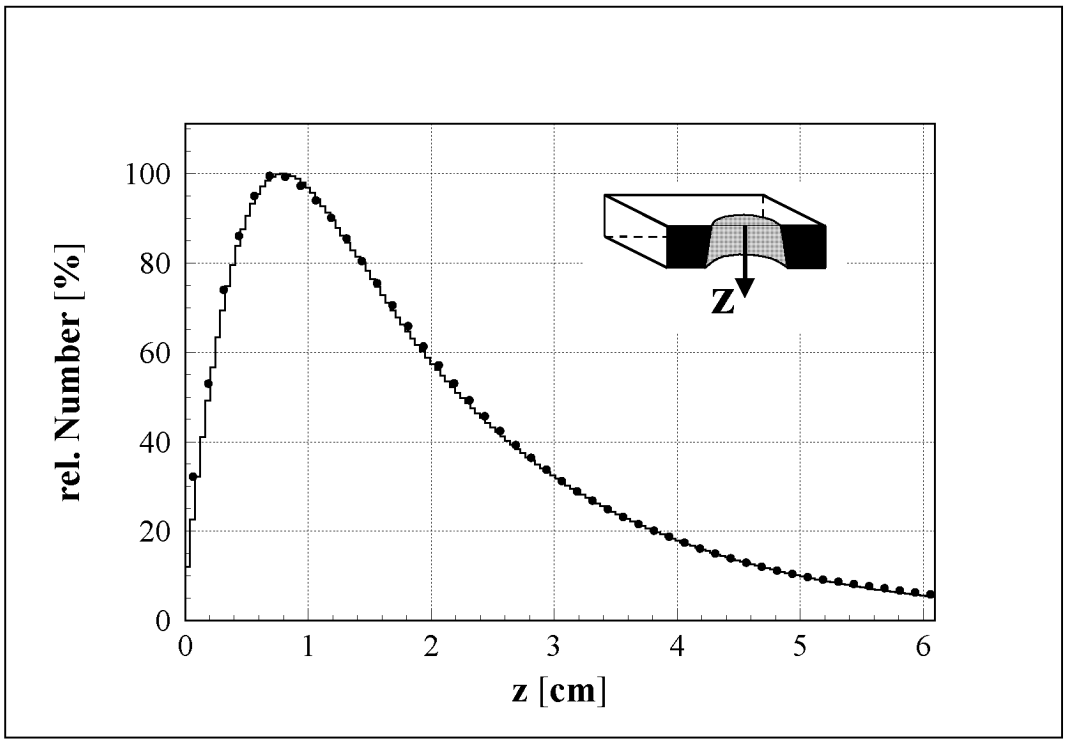

FIG. 9. An example of the results of the fitting algorithm for the primary collimator (9 x 17 cm^2 field). The figure shows the distributions of the *z* coordinates of the points of origin of the particles (full curve) together with the corresponding distribution resulting from the original PS data (dots).

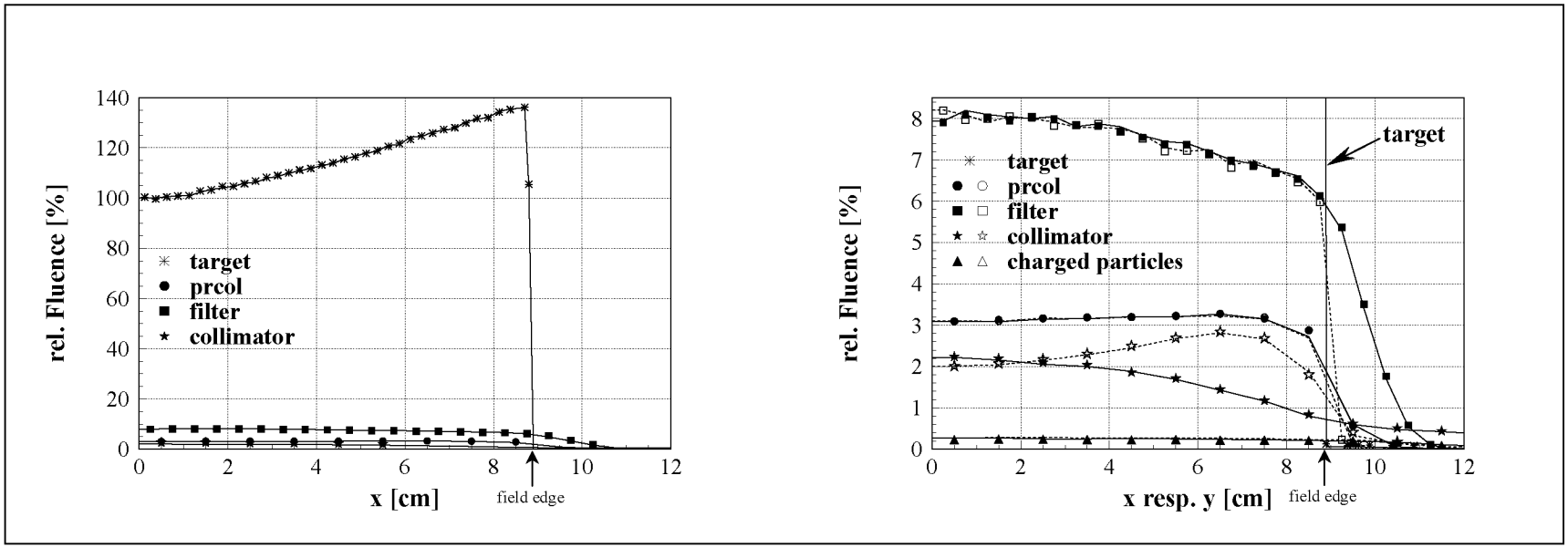

FIG. 10. Spatial fluence distributions in the output plane for the 40 x 40cm^2 field of the MSM (curves) and the original PS data (symbols). The right side gives some more details of the scatter components. The full curves together with the full symbols represent the spatial fluence distribution along the *x*-axis, the broken curves and the open symbols that along the *y*-axis. The target is only shown along the *x*-axis. (prcol = primary collimator.)

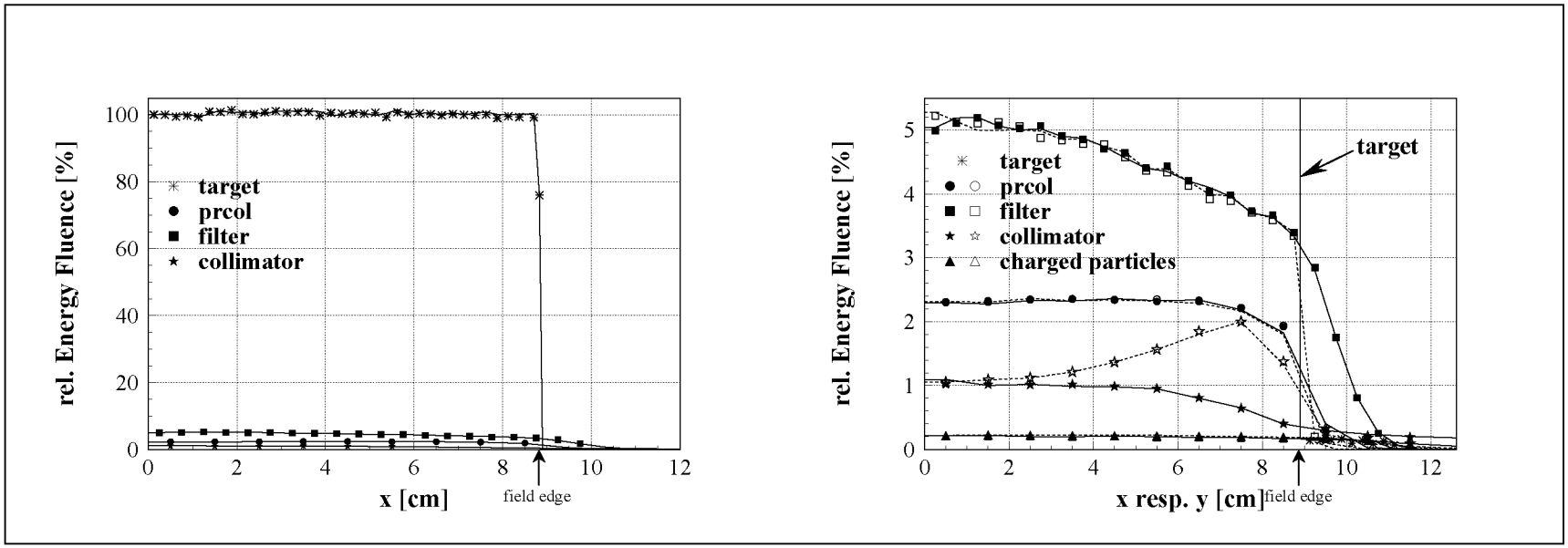

FIG. 11. Energy fluence distributions in the output plane for the 40 x 40 cm^2 field of the MSM (curves) and the original PS data (symbols). The right-hand side gives some more details of the scatter components. The full curves together with the full symbols represent the distribution of energy fluence along the *x*-axis, the broken curves and the open symbols that along the *y*-axis. The target is only shown along the *x*-axis. (prcol = primary collimator.)

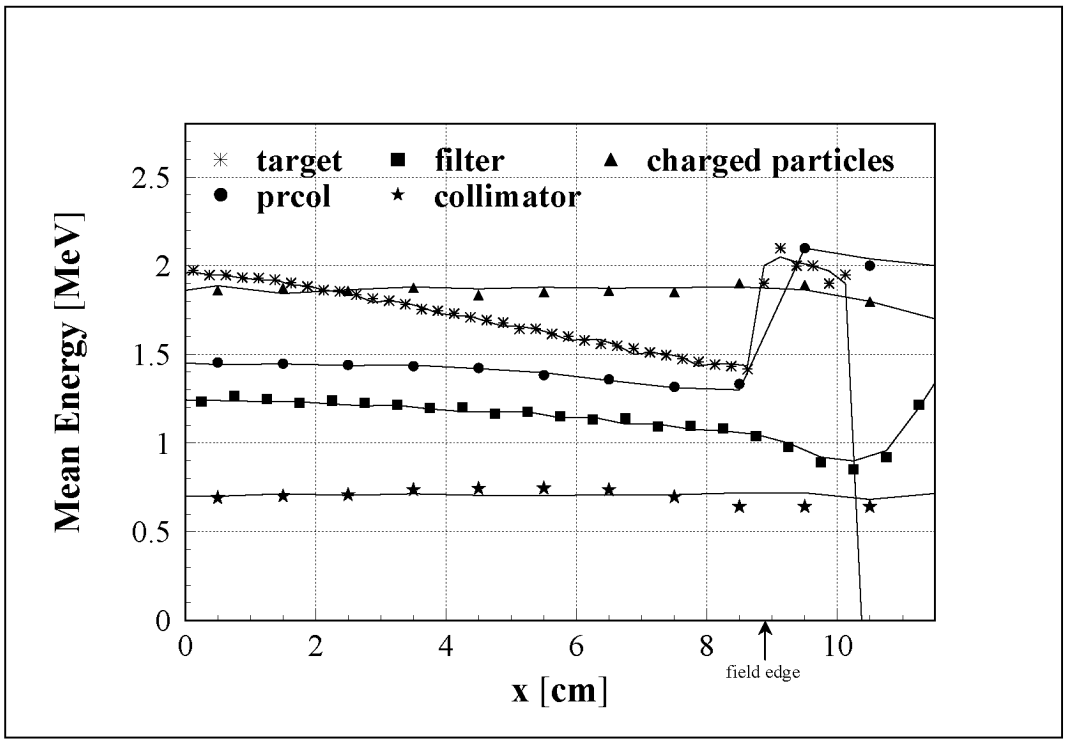

FIG. 12. Mean energy distributions in the output plane for the 40 x 40 cm^2 field of the MSM (full curves) and the original PS data (symbols) along the *x*-axis. (prcol = primary collimator.)

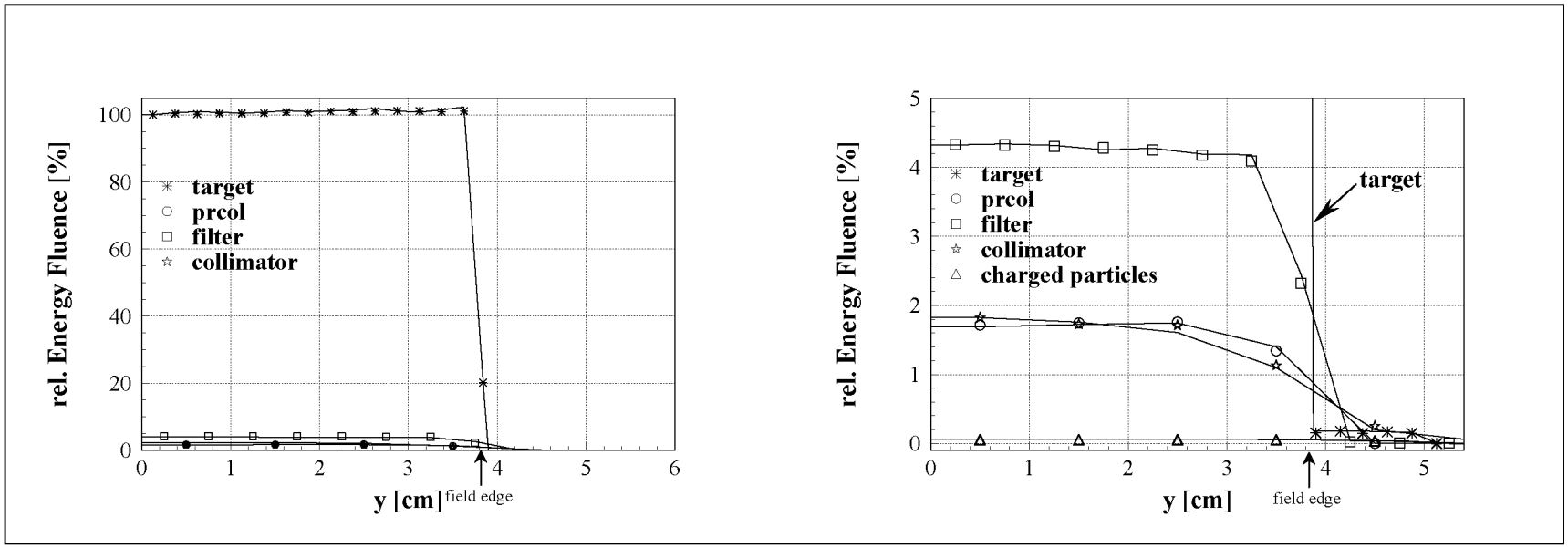

FIG. 13. Distributions of energy fluence in the output plane for the 9 x 17cm^2 field of the MSM (full curves) and the original PS data (symbols). The right-hand side gives some more details of the scatter components. (prcol = primary collimator.)

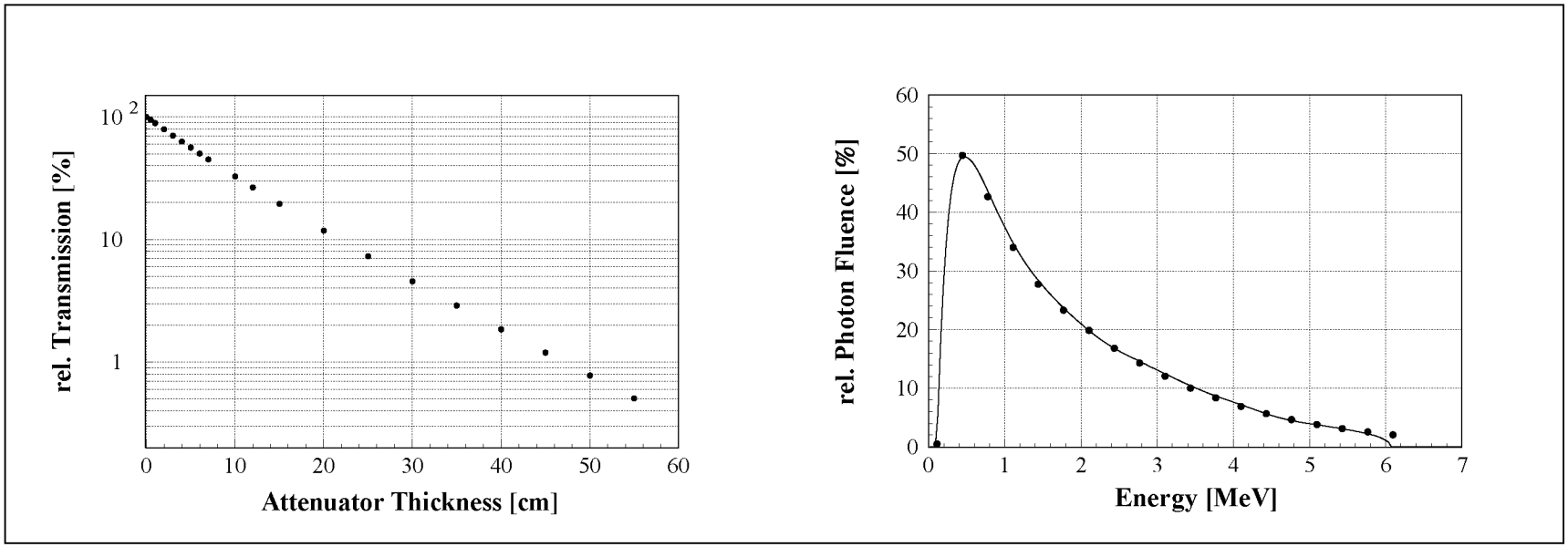

FIG. 14. Transmission curve (left) and reconstructed energy spectrum (right) of a 6 MV photon beam using an empirical numerical method introduced by Francois *et al* (1993). Aluminium was used for the attenuator and the build-up material. The full curve is the MC calculated spectrum whereas the dots result from the reconstruction of the transmission curve. The error bars for the measurements are smaller than the markers.

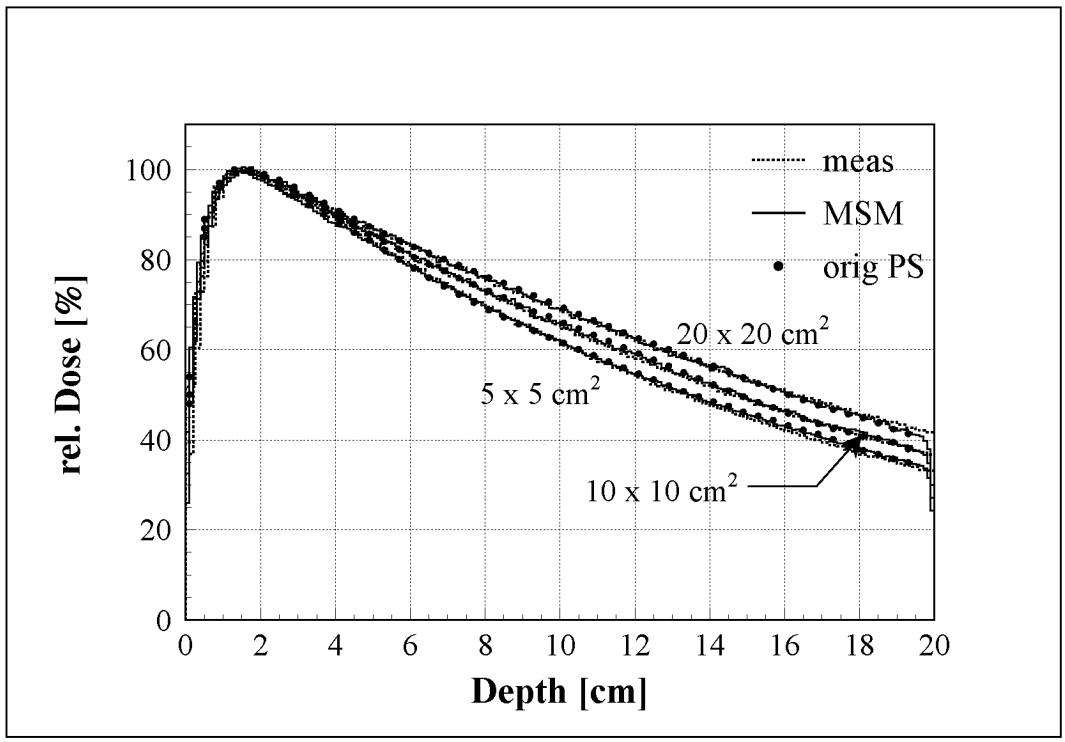

FIG. 15. Examples of calculated depth dose curves together with the corresponding measurements for three different field sizes of a 6 MV photon beam. The dots represent the depth dose calculation using the original PS data. The decrease at 20 cm water depth is due to the lack of backscatter, because the thickness of the phantom in the calculation was 20 cm.

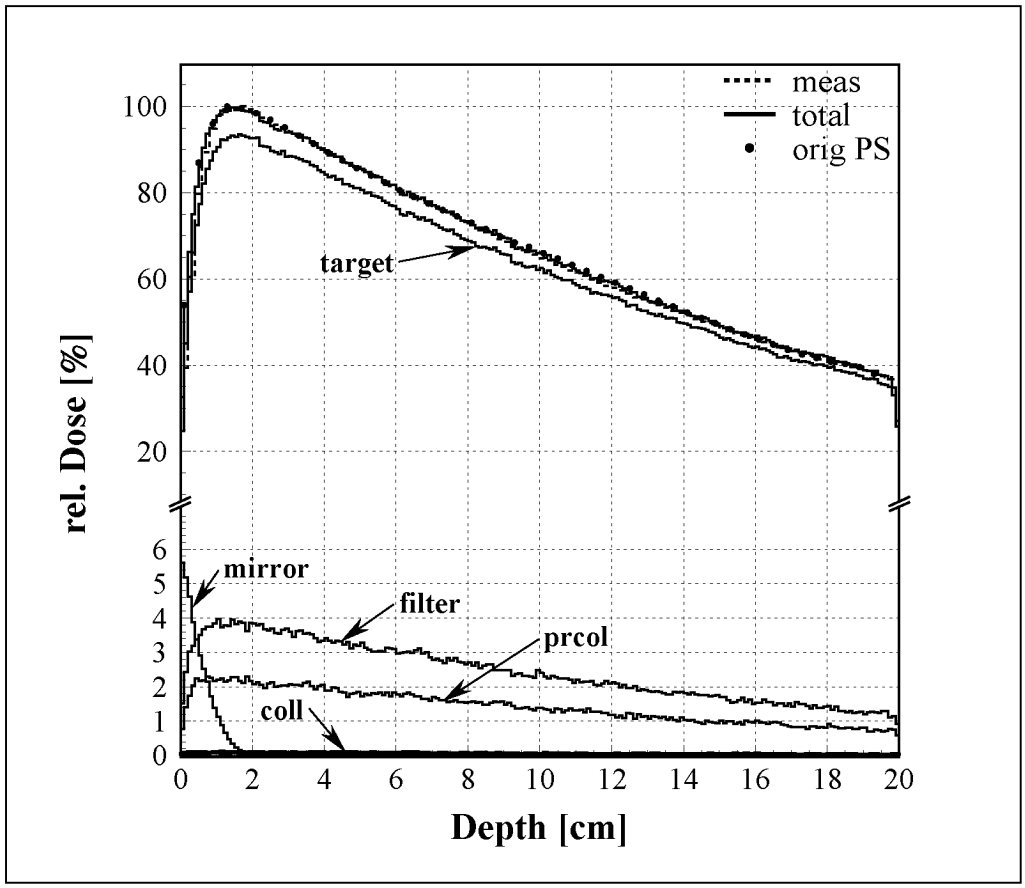

FIG. 16. Contribution of all sources defined in the MSM to the calculated depth dose curve together with the corresponding measurement for the 10 x 10 cm^2 field. The dots represent the depth dose calculation using the original PS data. The scatter components are shown in detail in the lower part. (prcol = primary collimator, coll = secondary collimator.)

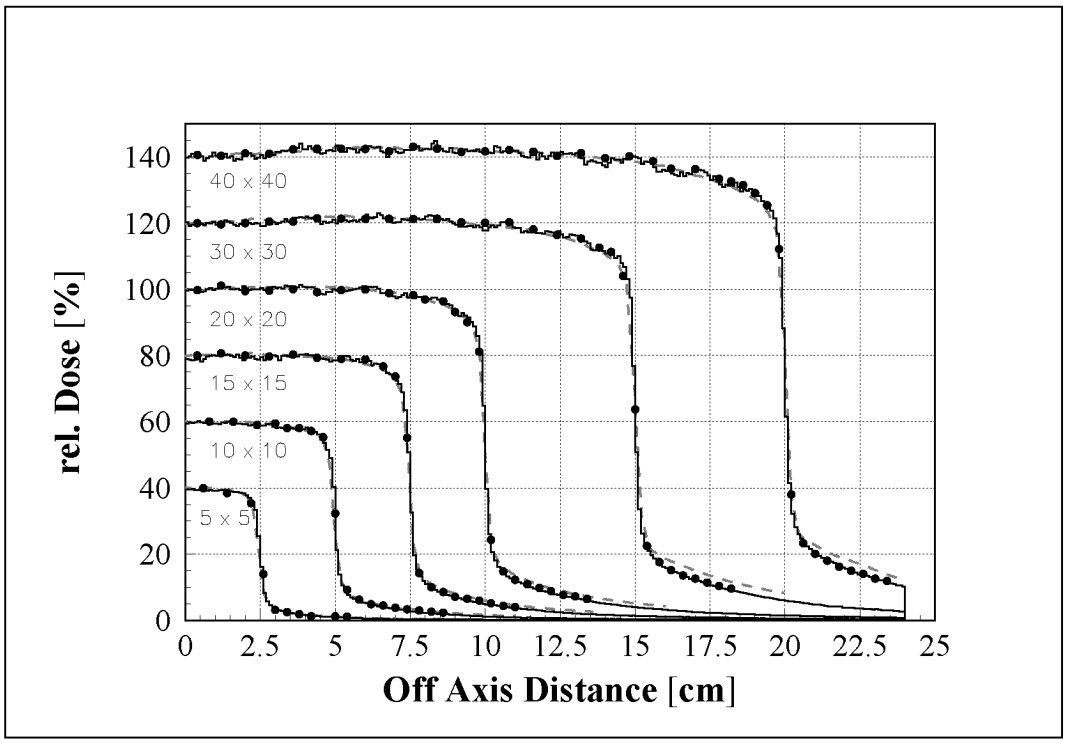

FIG. 17. Comparison of calculated (full curves) and measured (broken curves) dose profiles for several field sizes in a water depth of 10 cm for a 6 MV photon beam. The dots represent the calculation of the profiles using the original PS data. For better readability, the profiles for the different field sizes are normalized to different central axis values.

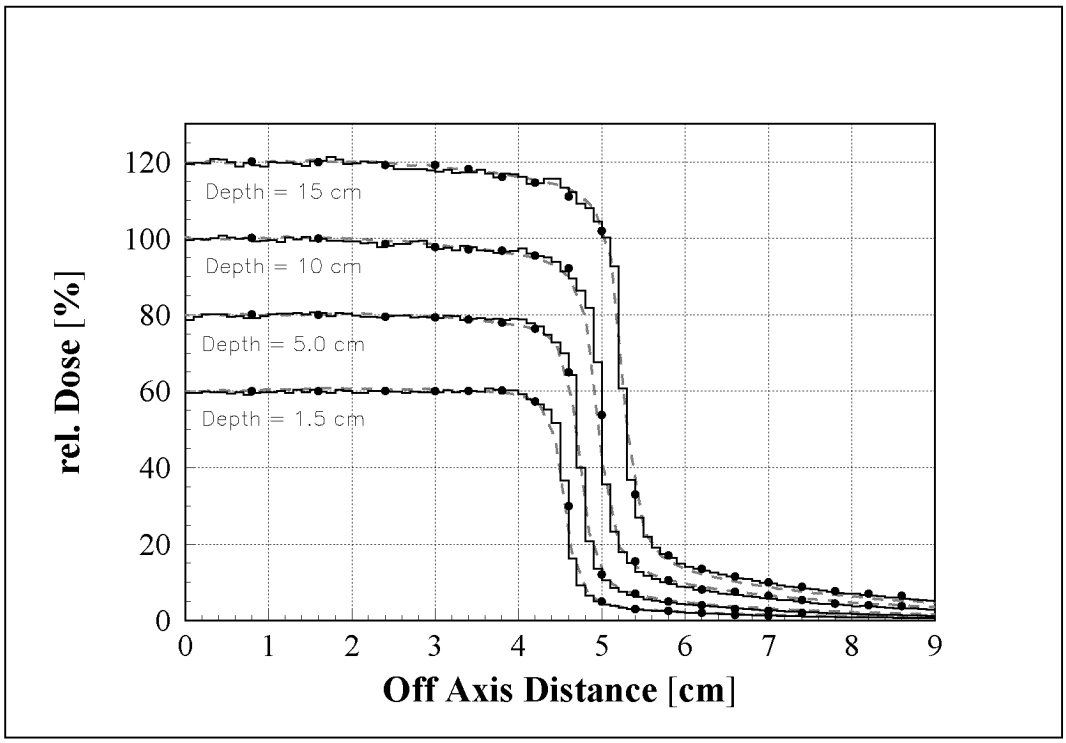

FIG. 18. Calculated dose profiles (full curves) in four different depths together with the corresponding measurements (broken curves) for the 10 x 10 cm^2 field of a 6 MV photon beam. The dots represent the calculation of the profiles using the original PS data. For better readability, the profiles for the different depths are normalized to different central axis values.

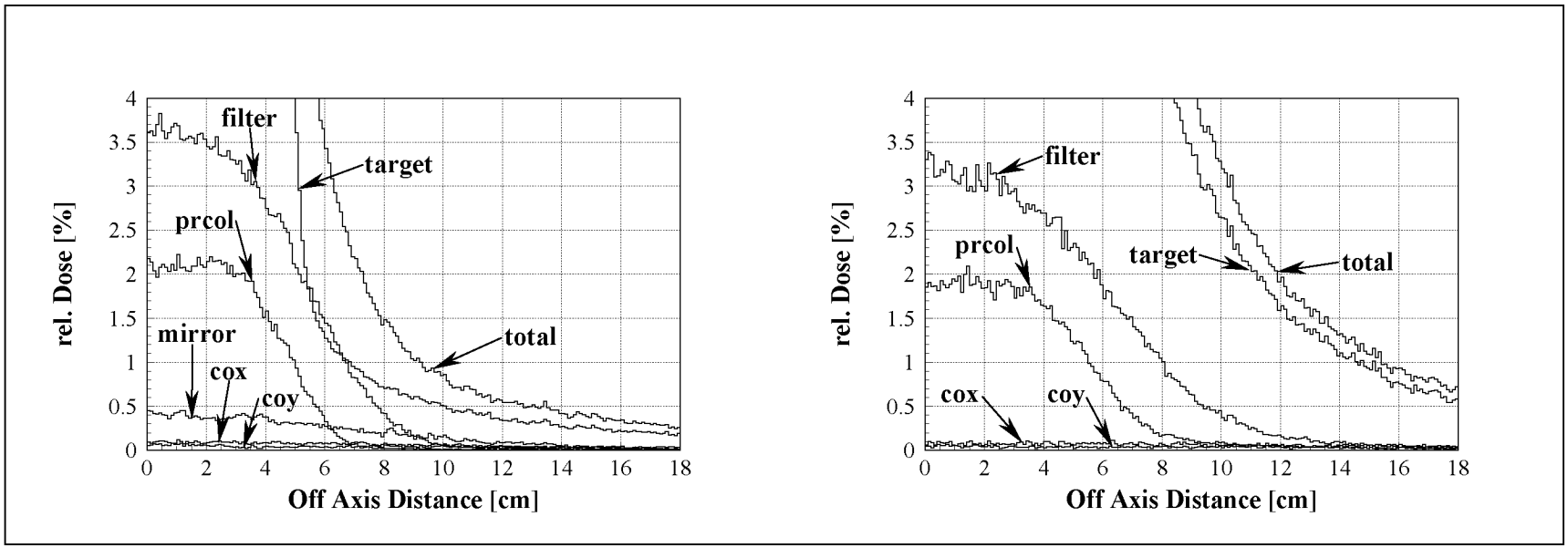

FIG. 19. Details of the dose profiles in water depths of 1.5 cm (left) and 15 cm (right) for the 10 x 10 cm^2 field. The flattening filter is the main scatter source in the 6 MV photon beam. The contribution of the mirror occurs only for 1.5 cm water depth. (prcol = primary collimator, cox = the upper pair of jaws of the secondary collimator, coy = the lower pair of jaws of the secondary collimator.)

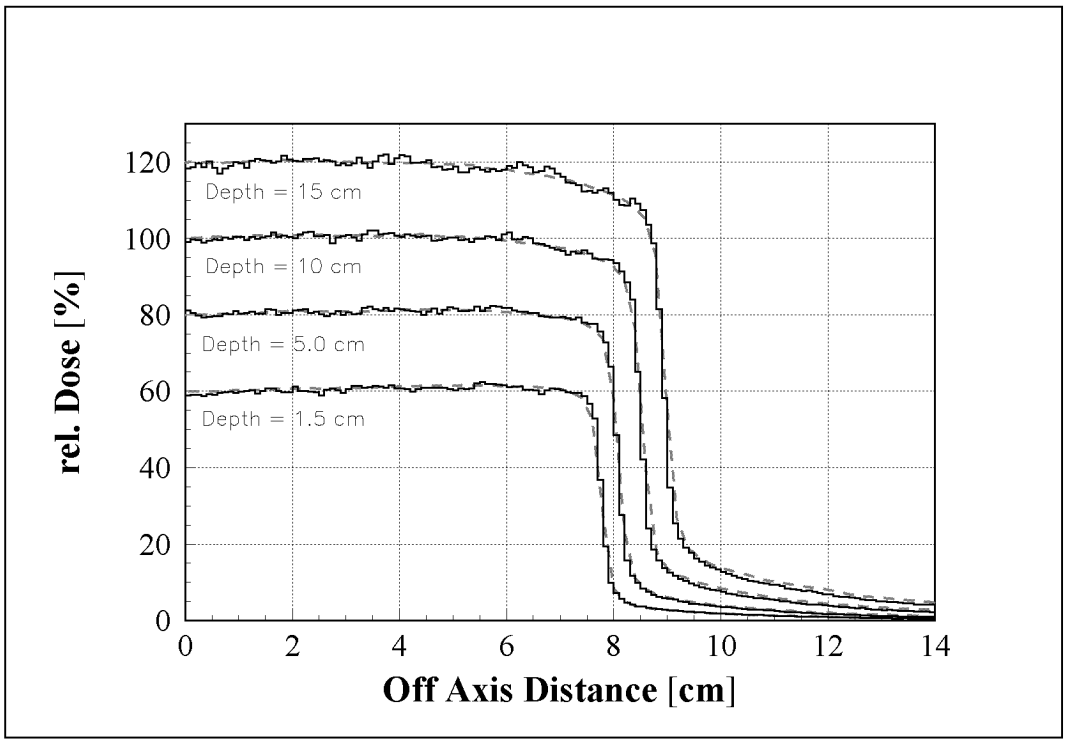

FIG. 20. Calculated dose profiles (full curves) for four depths together with corresponding measurements (broken curves) for the 9 x 17 cm^2 field of a 6 MV photon beam. For better readability, the profiles for the different depths are normalized to different central axis values.

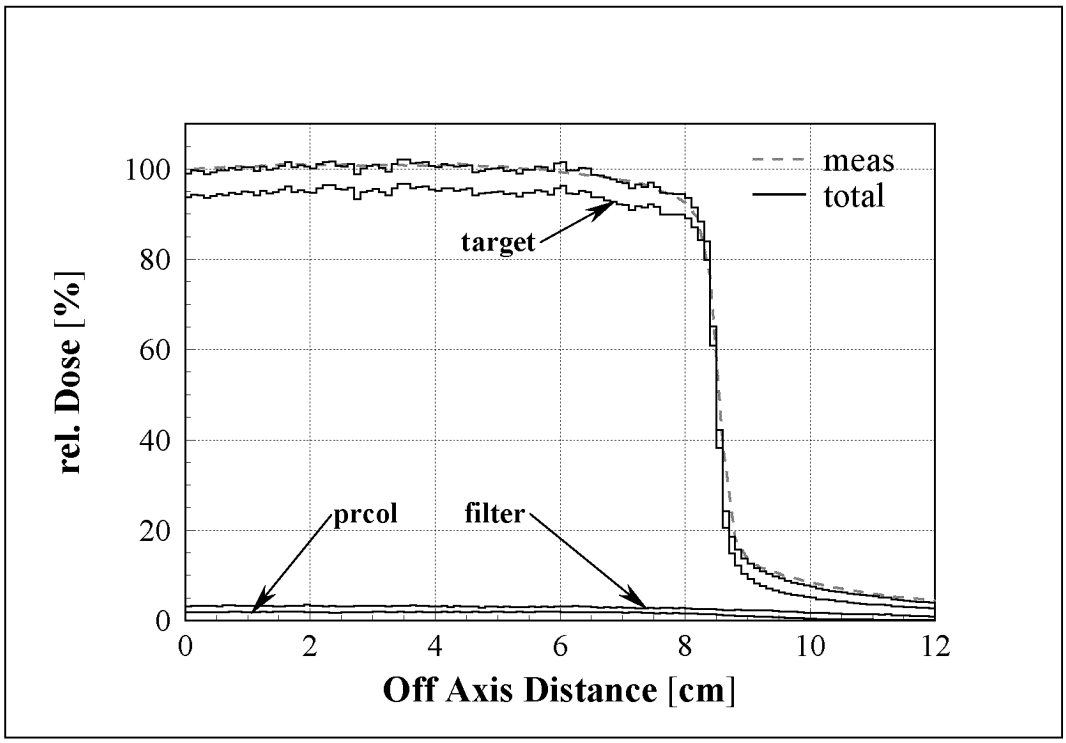

FIG. 21. Contribution of the main sources defined in the MSM to the total dose profile for the 9 x 17 cm^2 field in 10 cm water depth together with the corresponding measurements. (prcol = primary collimator.)

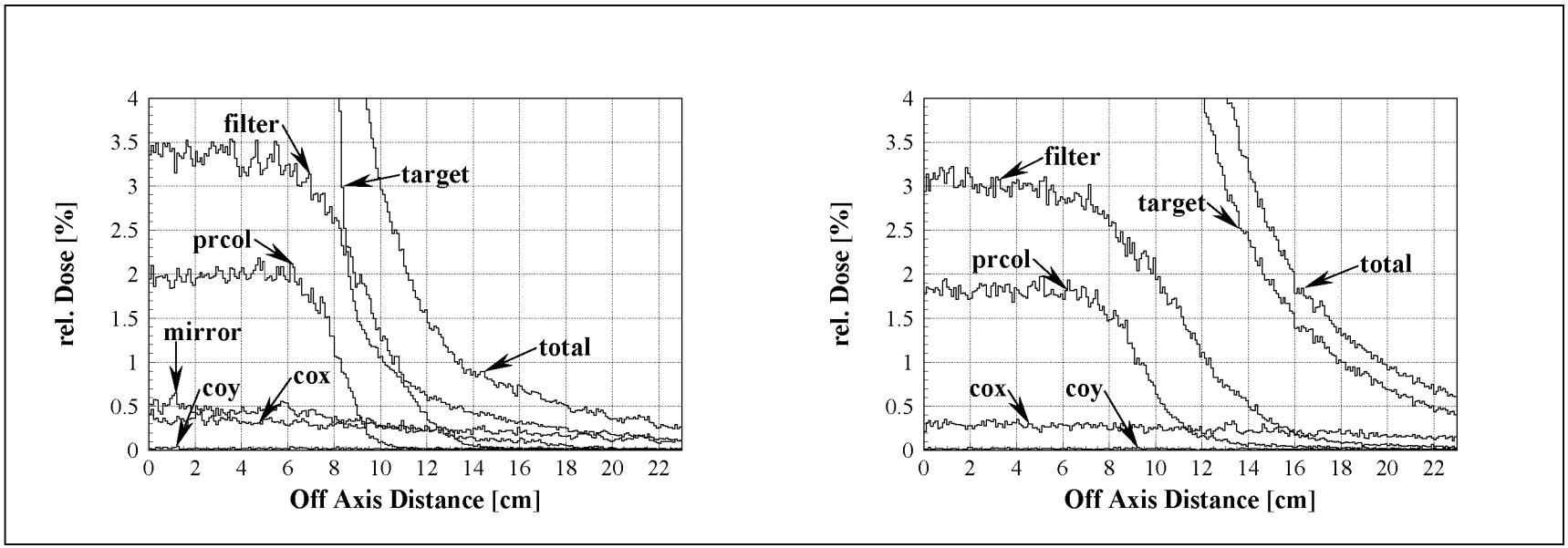

FIG. 22. Details of the dose profiles in 1.5 cm (left) and 15 cm water depth (right) for the 9 x 17 cm^2 field. The flattening filter is the main scatter source in the 6 MV photon beam. The contribution of the mirror occurs only in 1.5 cm water depth. (prcol = primary collimator, cox = the upper pair of jaws of the secondary collimator, coy = the lower pair of jaws of the secondary collimator.)

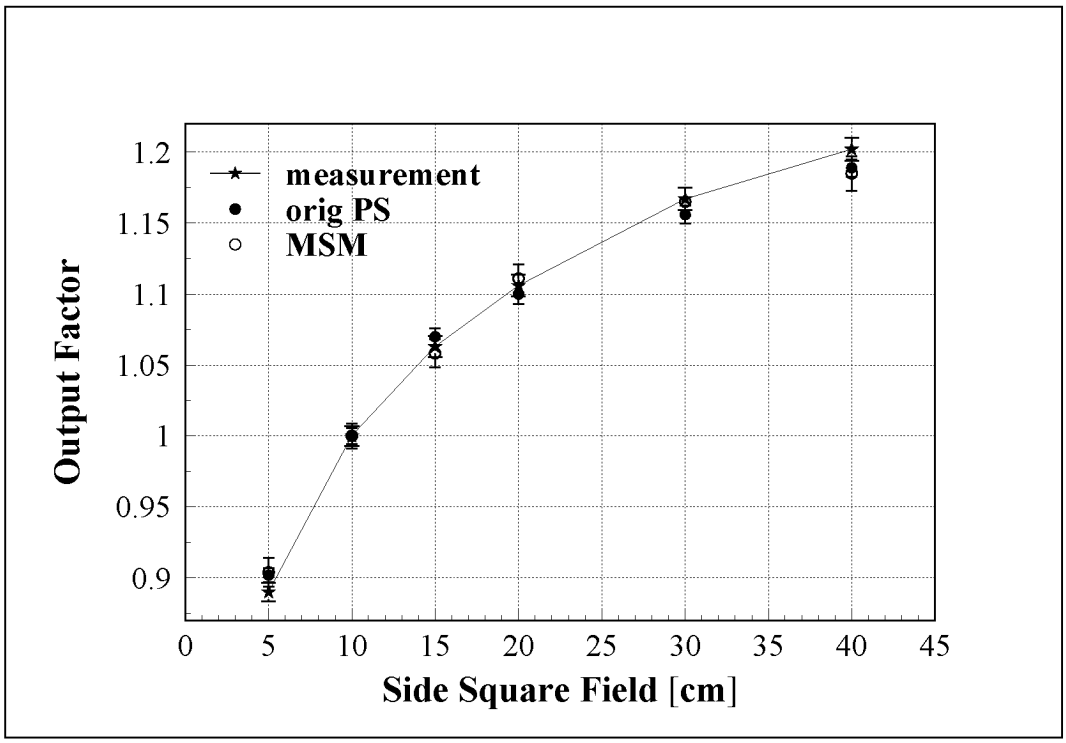

FIG. 23. Output factors in water (SSD = 90 cm, depth = 10 cm). The full curve connects the data points from measurements, the discrete points (symbols) are from the Monte Carlo simulations.

4

Computer algebra for x-ray spectral reconstruction between 6 and 25 MV

published in
Medical Physics
2001, Vol. 28, No. 3, 325-327

Computer algebra for x-ray spectral reconstruction between 6 and 25 MV

Marco Stampanoni[a)] and Michael Fix

Institute for Biomedical Engineering, University of Zürich and Swiss Federal Institute of Technology (ETH), Moussonstrasse 18, CH-8044 Zürich, Switzerland

Pascal Francois

Institut Claudius Regaud, Unité de Physique, Département de Radiothérapie, 20-24 Rue du Pont St Pierre, 31052 Toulouse, France

Peter Rüegsegger

Institute for Biomedical Engineering, University of Zürich and Swiss Federal Institute of Technology (ETH), Moussonstrasse 18, CH-8044 Zürich, Switzerland

Short title: Computer algebra for x-ray spectral reconstruction

Abstract

A previously presented algorithm for the reconstruction of bremsstrahlung spectra from transmission data has been implemented into MATHEMATICA®. Spectral vectorial algebra has been used to solve the matrix system $A * F = T$. The new implementation has been tested by reconstructing photon spectra from transmission data acquired in narrow beam conditions, for nominal energies of 6, 15, and 25 MV. The results were in excellent agreement with the original calculations. Our implementation has the advantage to be based on a well-tested mathematical kernel. Furthermore it offers a comfortable user interface.

Key words: photon energy spectra, transmission measurements, spectral vectorial algebra, numerical reconstruction

Good knowledge of high-energy photon spectra produced by medical accelerators is important for different aspects of the clinical routine work such as beam quality determination, beam calibration, or dose calculations in media.[1-3]

One approach consists in estimating the photon spectrum starting from transmission data measured in narrow beam conditions. Between the different numerical techniques proposed for the reconstruction of the spectrum,[1-5] the method of Francois *et al.*[6] shows many advantages and has fewer limitations. Francois *et al.*[6] reduced the physical problem to a matrix system $A*F=T$ which is directly solved by using spectral vectorial algebra.[6-8]

We transferred the main calculating steps of the code implemented by Francois *et al.*[6] into a MATHEMATICA notebook.[9] One of the many advantages of MATHEMATICA is the use of a symbolic language that can manipulate a wide range of objects using a small number of basic primitives. For example, it is possible to compute eigenvalues and eigenvectors of a matrix with an arbitrary precision, without deterring the numerical stability of the calculations. This also improves the clarity of the code.

Our work summarizes the physical and mathematical aspects of the method, gives a short description of the logical implementation, and shows the validity of the results by comparing photon spectra of different nominal energies calculated with both implementations.

The relative transmission function $T(x)$ is defined as the ratio between the chamber signal $S(x)$, measured with an absorber of thickness x, and the signal $S(x=0)$, without absorber:

$$T(x)=\frac{S(x)}{S(0)}=\int_0^{E_{\max}}\exp\left[-\mu(E)\cdot x\right]\cdot F(E)dE. \tag{1}$$

$\mu(E)$ is the linear attenuation coefficient of the attenuator for the energy E, $F(E)$ is the fraction of the signal produced by photons with energy between E and $E+dE$ of the unattenuated beam, and $E_{\max}$ is the maximum energy of the spectrum.

Equation (1) is rewritten in form of a linear system of order n using Simpson's approximation:

$$A*F=T. \tag{2}$$

T is the relative transmission vector whose components are

$$T_i = \sum_{j=1}^{n} A_{ij} \cdot F_j, \tag{3}$$

$$A_{ij} = \alpha \cdot \frac{\Delta E}{3} \cdot e^{-\mu_j x_i}$$

with

$$\alpha = \begin{cases} 1 & \text{for} \quad j = 1 \quad \text{and} \quad n \\ 4 & \text{for} \quad j = 2,4,\ldots,n-1 \\ 2 & \text{for} \quad j = 3,5,\ldots,n-2 \end{cases}$$

and

$$\Delta E = \frac{(E_n - E_1)}{(n-1)}$$

is an element of the attenuation matrix A.

Following the theory of spectral vectorial algebra, the solution of the linear system (2) is expressed as a numerical sum of the projector matrices π_k (associated to the kth eigenvalue s_k of A) by[6]

$$F(E_j) = F_j = \left[\sum_{k=1}^{4} \frac{1}{s_k} [\pi_k T] \right]_j, \tag{5}$$

where F_j represents the jth component of the vector F and the projectors π_k are calculated directly from the matrix A using

$$\pi_k = \frac{X_k {}^t Y_k}{{}^t Y_k X_k}, \tag{6}$$

where X_k is a right and ${}^t Y_k$ a left eigenvector of A.

The photon fluence • •is calculated from F with the following relationship:

$$\Phi(E) = \frac{1}{R(E) \cdot E} \cdot F(E), \tag{7}$$

where the function $R(E)$ gives the chamber response per unit energy fluence and is described in the work of Catala *et al.*[10]

The main steps of the reconstruction algorithm are described in Fig. 1. Transmission curve and chamber response are entered first as input. XCOM[11] supplies the attenuation coefficients for the user defined but arbitrary energy bins. The elements of the matrix A are calculated according to Eq. (4). In a third step, eigenvalues and

eigenvectors of A are determined using well-tested build-in functions of MATHEMATICA. The associated projectors π_k are computed following Eq. (6) and finally the photon spectrum is reconstructed using expression (7). The reconstruction is performed almost instantaneously (<5 s) on a 400 MHz Pentium II.

In order to test the MATHEMATICA implementation,[12] the spectra for three different nominal energies (6, 15, and 25 MV) were reconstructed using the same input data as for the code of Francois *et al.*[6]

The comparison between the spectra calculated with the two codes shows excellent agreement as depicted in Fig. 2 for a 6 MV photon beam. Figures 3 and 4 show the same comparison for nominal energies of 15 MV and 25 MV, respectively.

In order to compare quantitatively the results of the two codes, we calculated relative errors defined as

$$\left| \left(1 - \frac{\Phi_{\text{Francois}}}{\Phi_{\text{MATHEMATICA}}} \right) \times 100 \right|,$$

where Φ_{Francois} and $\Phi_{\text{MATHEMATICA}}$ represent the relative photon fluences obtained using Eq. (7) with the code of Francois *et al.*[6] and our code, respectively.

We found relative errors of less than 1% for all the reconstructed spectra except for two values before the modal energy of the 15 MV spectrum. These small discrepancies can be explained by the fact that the algorithm of Francois *et al.*[6] is very sensitive to measurement errors for energies lying just before the modal energy as depicted in Fig. 10 of Ref. 6. On the other hand, our implementation works with a higher numerical precision, which reduces the numerical errors of the reconstruction. In any case the modal energy is founded exactly (relative error <0.1%) for the three nominal energies investigated, which further confirms the validity of our implementation.

With this work we validate the calculations of Francois *et al.*[6] and offer a new, fast, and user-friendly software for the reconstruction of photon spectra.

References

[a] Electronic mail: stampanoni@biomed.ee.ethz.ch

1 P. H. Huang, K. R. Kase, and B. E. Bjärngard, "Spectral characterization of 4 MV Bremsstrahlung by attenuation analysis," Med. Phys. **8**, 368-374 (1981).

2 A. Piermattei, G. Arcovito, L. Azario, C. Bacci, L. Bianciardi, E. De Sapio, and C. Giacco, "A study of quality of Bremsstrahlung spectra reconstructed from transmission measurements," Med. Phys. **17**, 227-233 (1982).

3 R. G. Waggener, M. M. Blough, J. A. Terry, D. Chen, N. E. Lee, S. Zhang, and W. D. McDavid, "X-ray spectra estimation using attenuation measurements from 25 kVp to 18 MV," Med. Phys. **26**, 1269-1278 (1999).

4 M. Krmar, J. Slivka, I. Bikit, M. Veskovic, L. Conkic, M. Bistrovic, and A. Rudic, "A new method for the measurement of bremsstrahlung spectra," Phys. Med. Biol. **38**, 533-544 (1993).

5 C. R. Baker, B. Ama'ee, and N. M. Spyrou, "Reconstruction of megavoltage photon spectra by attenuation analysis," Phys. Med. Biol. **40**, 529-542 (1995).

6 P. Francois, A. Catala, and Ch. Scouarnec, "Simulation of x-ray spectral reconstruction from transmission data by direct resolution of the numeric system *AF=T*," Med. Phys. **20**, 1695-1703 (1993).

7 P. Francois, F. Coste, J. Bonnet, and O. Caselles, "Validation of reconstructed bremsstrahlung spectra between 6 MV and 25 MV from measured transmission data," Med. Phys. **24**, 769-773 (1997).

8 Ch. Scouarnec, *Algebre spectrale*, (Ed. Publisud, Paris tome 1, 1987), pp. 166-171.

9 S. Wolfram, *Das Mathematica Buch*, 3rd ed. (Addison-Wesley, Bonn, 1997).

10 A. Catala, P. Francois, J. Bonnet, and Ch. Scouarnec, "Reconstruction of 12 MV bremsstrahlung spectra from measured transmission data by direct resolution of the numeric system *AF=T*," Med. Phys. **22**, 3-10 (1995).

11 J. H. Hubbell, "Photon mass attenuation and energy-absorption coefficients from 1 keV to 20 MeV", Int. J. Appl. Radiat. Isot. **33**, 1269-1290 (1982).

12 See EPAPS Document No. E-MPHYA6-28-006103 for mathematical notebook, data, and sample files for spectral reconstruction. This documet may be retrieved

via the EPAPS homepage (http://www.aip.org/pubservs/epaps.html) or from ftp.aip.org in the directory/epaps. See the EPAPS homepage for more information.

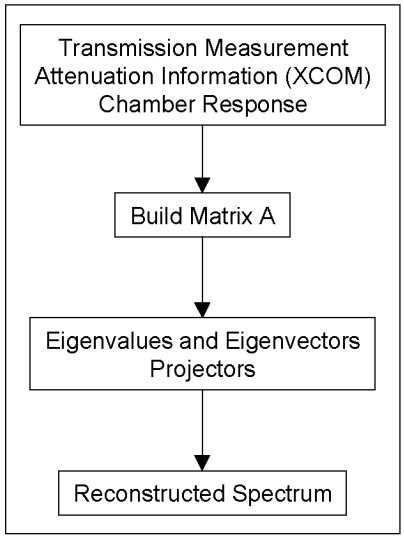

FIG. 1. Schematic representation of the main steps performed by the algorithm in order to calculate the photon spectrum.

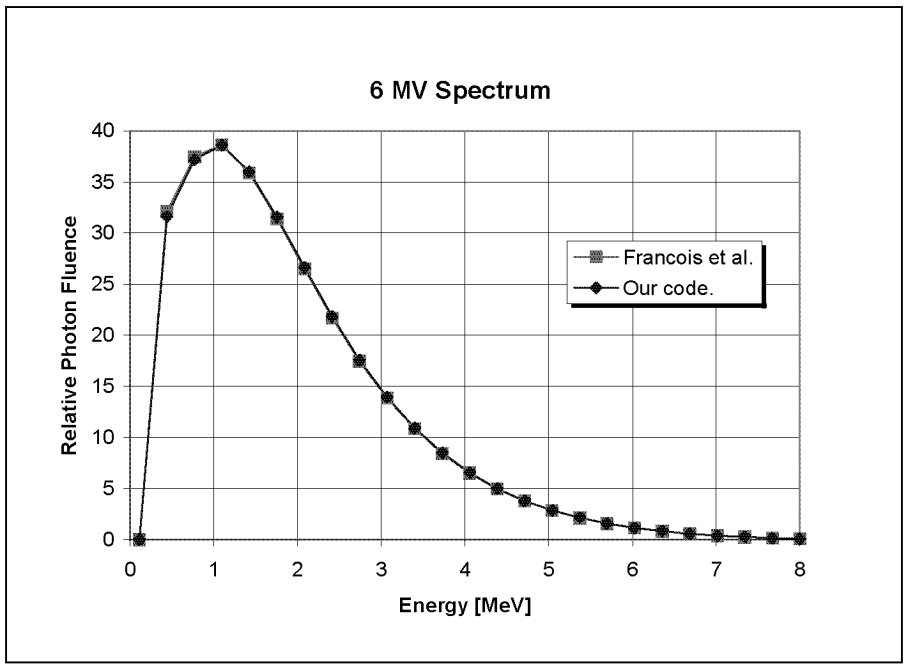

FIG. 2. Recalculated spectrum of a 6 MV Saturne 43 photon beam. Dark diamonds represent the MATHEMATICA output and light squares are the results of Francois *et al.* (Ref.6).

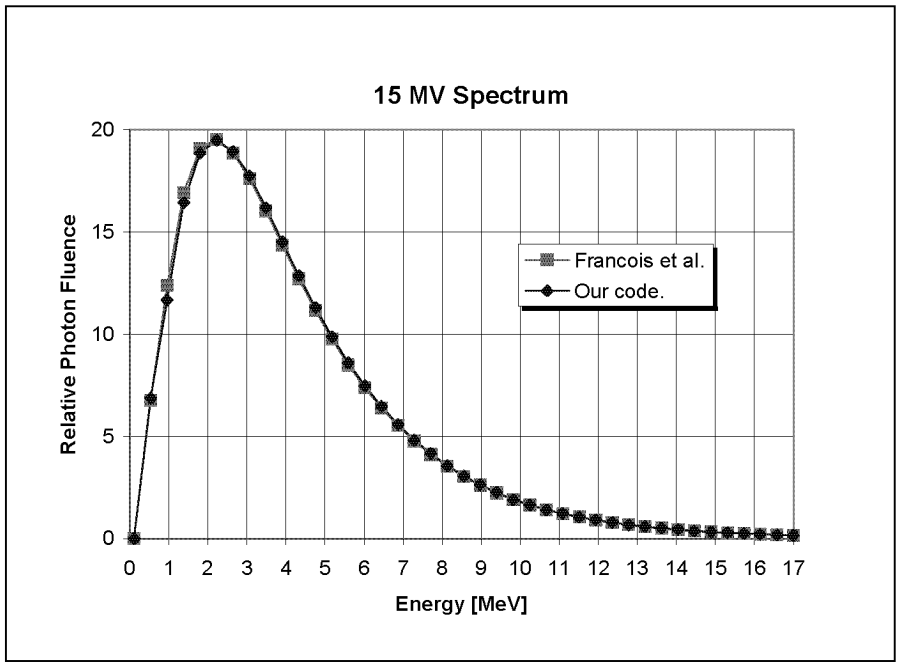

FIG. 3. Recalculated spectrum of a 15 MV Saturne 43 photon beam. Dark diamonds represent the MATHEMATICA output and light squares are the results of Francois *et al.* (Ref.6).

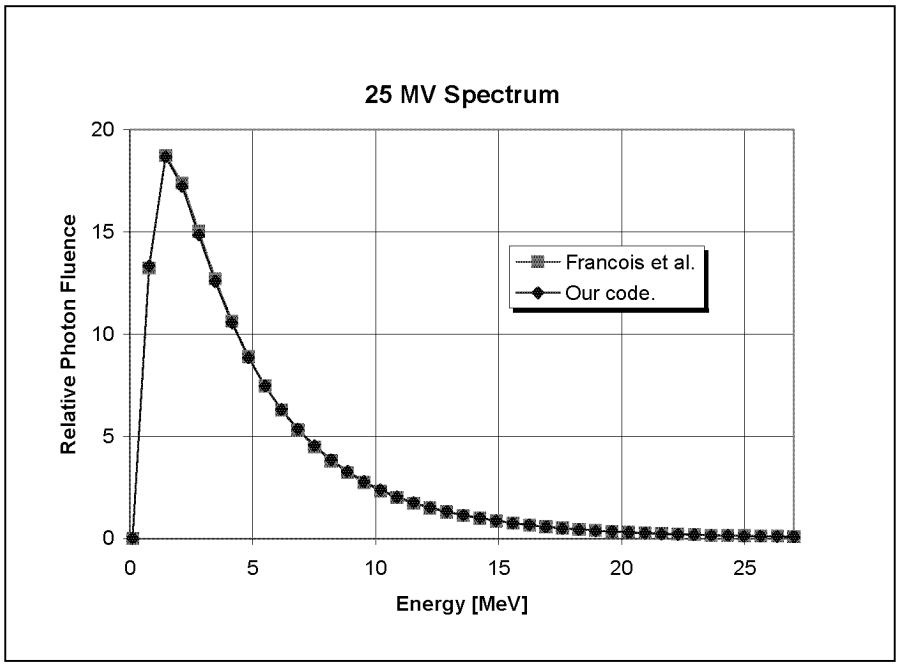

FIG. 4. Recalculated spectum of a 25 MV Saturne 43 photon beam. Dark diamonds represent the MATHEMATICA output and light squares are the results of Francois *et al.* (Ref.6).

5

Monte Carlo Simulation of a Dynamic MLC: Implementation and Applications

published in
Zeitschrift für Medizinische Physik
2001, Vol. 11, 163-170

Monte Carlo Simulation of a Dynamic MLC: Implementation and Applications

Monte Carlo Simulation eines dynamischen MLC: Implementation und Anwendungen

M. K. Fix[1], P. Manser[1], E. J. Born[2], D. Vetterli[2], R. Mini[2], P. Rüegsegger[1]

[1] Institute for Biomedical Engineering, University of Zurich and ETH

[2] Division of Medical Radiation Physics, Clinic of Radio-Oncology, Inselspital and University of Berne

Abstract

Purpose: Study of behavior and influence of a multileaf collimator (MLC) on dose calculation, verification, and portal energy spectra in the case of intensity-modulated fields obtained with a step-and-shoot or a dynamic technique.

Methods: The 80-leaf MLC for the Varian Clinac 2300 C/D was implemented in a previously developed Monte Carlo (MC) based multiple source model (MSM) for a 6 MV photon beam. Using this model and the MC program GEANT, dose distributions, energy fluence maps and energy spectra at different portal planes were calculated for three different MLC applications.

Results: The comparison of MC-calculated dose distributions in the phantom and portal plane, with those measured with films showed an agreement within 3% and 1.5 mm for all cases studied. The deviations mainly occur in the extremes of the intensity modulation. The MC method allows to investigate, among other aspects, dose components, energy fluence maps, tongue-and-groove effects and energy spectra at portal planes.

Conclusion: The MSM together with the implementation of the MLC is appropriate for a number of investigations in intensity-modulated radiation therapy (IMRT).

Key words: Monte Carlo Simulation, beam model, dynamic MLC, IMRT

Zusammenfassung

Ziel: Das Verhalten und der Einfluss des Mehrlamellenkollimators (MLC) in intensitätsmodulierten Feldern sollen unter dem Aspekt von Dosisberechnungen, Verifikation und portalen Energiespektren untersucht werden. Dabei wird die Intensitätsmodulation durch die step-and-shoot oder eine dynamische Technik realisiert.
Methode: Der 80-Lamellen-Kollimator für den Linearbeschleuniger Varian Clinac 2300 C/D wurde in ein bereits existierendes Monte-Carlo(MC)-basiertes Mehrkomponentenmodell (MSM) für einen 6-MV-Photonenstrahl implementiert. Mit Hilfe dieses Modells und des MC Programms GEANT wurden für 3 verschiedene MLC Konfigurationen Dosisverteilungen, Matrizen von Energiefluenzen und Energiespektren in mehreren Portalebenen berechnet.
Resultate: Der Vergleich der gerechneten Dosisverteilungen im Phantom und in der Portalebene mit den entsprechenden Filmmessungen zeigen eine Übereinstimmung innerhalb von 3% und 1.5 mm für alle betrachteten Situationen. Die MC-Berechnungen erlauben die Untersuchung von Dosiskomponenten, Matrizen von Energiefluenzen, Tongue-and-groove-Effekt, Energiespektren in Portalebenen, usw.
Schlussfolgerung: Das MSM mit dem zusätzlich implementierten MLC ist für eine Vielzahl von Untersuchungen im Bereich der intensitätsmodulierten Radiotherapie (IMRT) geeignet.

Schlüsselwörter: Monte-Carlo-Simulationen, Strahlmodelle, dynamischer MLC, IMRT

Introduction

An accurate prediction of dose distribution is essential in radiation therapy. Treatment planning systems often deal with algorithms based on the method of convolution/superposition, where precalculated or measured energy kernels are used [1, 10, 11]. Although these algorithms are quite fast, inaccuracies are their main drawback in the vicinity of tissue inhomogeneities [16, 17]. In addition, the requirements in accuracy are even higher when using new application methods. These methods make use of the multileaf collimator (MLC) as for instance the sliding window techniques in the intensity modulated radiotherapy (IMRT) [12, 13, 15]. In order to avoid systematic errors when large numbers of small radiation fields are superimposed in IMRT, accurate knowledge about the influence of the beam defining MLC leaves on the radiation field is essential. The measurement of two-dimensional dose distributions of all radiation field segments that might contribute to an IMRT treatment is impractical. A more powerful approach for detailed investigations are Monte Carlo (MC) simulations of the IMRT fields. This requires an exact model of the MLC leaves in combination with an accurate beam model above the MLC. As MC simulation of the radiation transport is most accurate for dose calculations, the beam would be best characterized by an MC beam model. Simple beam models have shown reasonable accuracy within the geometrical field, but these models were not flexible in field size and had some limitations in modeling the head scatter [6, 7]. Therefore a multiple source model is necessary to be able to calculate more general beam geometries.

In this work, a previously developed multiple source model (MSM) [8] is supplemented with an additional source representing an 80-leaf MLC. With this extended model, energy fluences and dose distributions can be calculated for static, step and shoot, and dynamic MLC fields. Whereas dose distributions are useful in checking treatment planning systems, energy fluence maps could be used as reference images for electronic portal imaging devices (EPIDs). In addition, energy spectra can be calculated in portal planes, which might be important for dose calibration of EPIDs.

Methods

Multiple Source Model (MSM)

The main input for the accurate simulation of a dynamic MLC is a detailed characterization of the beam in form of an MSM. To develop the MSM, simulations of a 6 MV photon beam of a Varian Clinac 2300 C/D were performed using the MC code GEANT 3.21 (Release 99). For this purpose, the main elements of the beam defining system were implemented in the MC code (Fig. 1 left part). An electron pencil beam hits the target at the central axis. The output plane located at the distance of 44.7 cm from the target (just below the secondary collimator jaws) is perpendicular to the central axis and is used as scoring plane for the phase space (PS) files. For each particle traversing the output plane the position, the charge, the energy, the direction of motion, and the head component of the last interaction are stored. PS data were generated for a set of square fields using 10 keV as the (kinetic) cutoff energy for the photons and for the charged particles. Thereafter, these data were analyzed in order to define the sources of the MSM (Table 1).

Furthermore, an interpolation algorithm was developed to extend the availability of the MSM to arbitrary rectangular fields without precalculation of additional PS data. Finally, a sampling procedure reproduces PS data from the MSM. Thereby, the starting point of a particle is sampled from a spatial particle fluence distribution in the output plane. The starting direction is determined by the line between the starting point and a sampled origin point of the particle on the corresponding head component. The distribution of the origin points was established by ray tracing the particles backwards from the PS files to the surface of the head component of the accelerator head. At last, an energy is sampled using an energy distribution defined in the output plane.

Comparisons between calculated PS data, depth doses and lateral dose profiles with measured and original PS data respectively, showed good agreement as presented in a previous work [8].

Implementation of the MLC

In this study, an 80-leaf Varian MLC with a leaf width of 1 cm at isocenter distance for the accelerator considered was modeled. Since it is important to model the MLC very accurately, the tongue and groove design used to reduce inter-leaf radiation leakage was taken into account. Figure 2 illustrates a cross section of the MLC leaves.

Each leaf consists of 7 partitions of tungsten. Since the definition of rounded forms for the leaf front ends is not straightforward in GEANT, they were modeled as plane surfaces, which were inclined according to the beam divergence depending on the actual leaf position. Therefore, the model does not account for the rounded form of the leaf front ends. However, an additional shift between opposite leaves independent on the leaf position was implemented as a correction in order to overcome this limitation. The concept as well as the accuracy of this correction has been investigated by several groups [2, 9, 14]. In our MLC model a shift of 1.2 mm was used as suggested by the measurements of Arnfield [2], whose method is based on dynamic uniform fields instead of static fields. The MLC is located below the output plane (Figure 1 right part). If a starting particle from the MSM interacts with a leaf of the MLC, this particle, as well as all secondary particles produced, are tagged to be assigned to the MLC source.

Applications of the extended MSM

The extended MSM was used to calculate energy fluences, dose distributions and energy spectra in planes perpendicular to the central axis of the field.

Energy fluence distributions were scored in a plane 80 cm from the target. A water phantom (30 x 30 x 25 cm^3) at SSD = 90 cm was used to calculate lateral dose distributions in water depths of 1.5, 5, 10 and 20 cm. In addition, a 30 x 30 x 9 cm^3 portal water phantom at 140 cm distance from the target was implemented in order to calculate portal dose distributions in a water depth of 3 cm (Fig. 1). The calculation of the portal dose distributions was performed with and without a water phantom (30 x 30 x 25 cm^3; SSD= 90 cm) containing two inhomogeneities: one half of the centered 4 cm thick layer consisted of air and the other half of bone (Fig. 1). Energy spectra were determined in portal planes at 100 and 140 cm distance from the target

with a 30 x 30 x 10 cm^3 water phantom (SSD = 90 cm) in the beam, i.e. directly below the water phantom and behind an additional air gap of 40 cm.

As an example of a static field, the MLC configuration shown in Figure 3 was used. For this static case, the energy fluence, dose distributions in the 10 cm thick water phantom and the energy spectra below each of the apertures were calculated. For the MC calculations, the number of starting particles was 100 Mio. In a second case, dose distributions in the 25 cm thick water phantom for a step and shoot arrangement of two segments were considered which complement one another to a 10 x 10 cm^2 field in order to show the tongue and groove effect. Additionally, portal dose distributions in the portal water phantom with and without the inhomogeneous phantom in the beam were calculated. The number of primary particles in the MC calculations was 200 Mio. per segment. These dose distributions were compared with corresponding film measurements using Kodak X-Omat V films. For a third example, a lateral dynamic MLC field taken from a potential five field treatment plan of a head and neck carcinoma created with the Helios system (Varian Medical Systems) was simulated in order to test the model in a clinical situation of IMRT. In principle each dynamic field can be discretized in a sufficiently high number of static fields, which are then computed in a sequential manner. In this example the 196 static fields were used which defined the dynamic field in the MLC control software. MC dose calculations in the 25 cm thick water phantom and portal dose distributions were compared to measured data from film dosimetry. The number of primary particles in the MC calculation was 20 Mio. per segment.

The dose scoring voxels were 0.1 x 0.1 x 1.0 cm^3 in all MC simulations and for the fluence distributions a grid size of 0.2 x 0.2 cm^2 was used. The (kinetic) cut-off energy for the photons and for the charged particles were set to 10 keV in all MC calculations. The CPU time of the simulation for the IMRT fields was about 7 minutes per segment on an Alpha XP 1000 workstation for 1 million primary particles per segment.

For film dosimetry phantoms consisted of slabs of Solid Water RMI 451 and bone material RMI 450 (Gammex RMI) with films positioned between the slabs. Film scanning was done by a VXR-16 film scanner (Vidar Systems Cooperation) connected to an RFA300 system (Scanditronix Medical). This scanning device was calibrated to optical density and the conversion of optical densities to dose was done by use of a

film calibration curve. The film calibration curve was determined by exposing 11 films to known doses from 5 to 120 cGy under calibration conditions. These conditions were: field size 10 x 10 cm^2, SSD 100 cm, depth of measurements 1.5 cm (6 MV). A correction for film fog and base was taken into account. Film registration was done using markers, which were set according to the positioning lasers. All films were taken from the same batch.

Results

The energy fluence distributions of the static case for all the MSM sources are shown on the left side of Figure 4. In addition, on the right side of Figure 4 the contribution to the energy fluence of the primary collimator is presented. The influence of the scatter radiation from the primary collimator on the sharpness of the field boundaries is clearly visible. The energy fluence contribution of the primary collimator is about 3% in the center of the open beam area. Figure 5 displays the corresponding dose distributions in a water depth of 5 cm for all MSM sources (left) and for the flattening filter (right). Apart from the primary radiation of the target, the radiation components of the flattening filter and of the primary collimator are most prominent and constitute the main contributions in the penumbra region, since the radiation from these head components have a wider angular distribution. As the energy spectra of the primary collimator and the flattening filter is softer than the one of the target, the relative contributions of the head scatter components decreases with increasing water depth, where the target radiation (including phantom scatter) becomes most prominent. For more details see also [8]. Clearly noticeable is the contribution to dose between the leaf edges in the left plot (see also Fig. 4). This example documents the correct implementation of the MLC.

To test the tongue and groove effect, a step and shoot case was simulated. Some results are illustrated in Figure 6 together with film measurements. In the left part of the radiation field, the tongue and groove effect takes place between all leaves. In the right part, two pairs of adjacent leaves were moved together, thus no tongue and groove effect occurs between these leaves. This effect results in a dose reduction between the leaves of about 15% in a water depth of 20 cm and about 25% in the depth of dose maximum. The deviations between the measured and calculated profiles are within 2% and 1 mm for all water depths. Some discrepancies occur outside the geometrical field, which has been already discussed in a previous work [8]. In order to avoid hot spots, the points of contact of the closed leaf pairs were located underneath the secondary collimator. To show the possibility of the extended MSM to precalculate portal dose distributions, the results of the portal dose distributions in 140 cm distance from the

target are depicted Figure 7. The dose values below the air inhomogeneity increase whereas the bone inhomogeneity absorbs more radiation leading to lower dose values in the area underneath, as expected. The increase and decrease in dose is about 10% compared with calculations done without a phantom in the beam. The results for the latter case are shown as a dose profile along the x-direction in Figure 7. The calculated and measured portal dose profiles show a good agreement within 2.5% and 1.5 mm.

The result of the MC dose calculation in a water depth of 10 cm for the IMRT field in the head and neck test case is presented in Figure 8. The calculated profiles agree within 3% and 1 mm for all water depths considered in comparison with the corresponding film measurements. The deviations mainly appear in the extremes of the intensity modulations. At the left boundary of the radiation field (see profile in x-direction) two low dose peaks of interleaf leakage appear superimposed on transmitted and scattered radiation. Figure 9 illustrates a comparison of calculated and measured portal dose profiles for the head and neck case in a portal plane 140 cm from the target, where an inhomogeneous phantom was in the beam. In contrast to the dose distribution depicted in Figure 8, the dose values below the air inhomogeneity increase, whereas the doses underneath the bone inhomogeneity decrease, as shown in Figure 7. The deviations between measured and calculated dose profiles are about 2% and 1 mm. In summary, all MC simulations of dynamic MLC fields coincide very well with film measurements for all cases studied.

Another application of the model is the calculation of energy spectra in portal planes, which is important for the calibration of EPIDs to dose. As an example, the energy spectra in the static case under the small and the big aperture of the MLC field (see Fig. 3) were calculated directly below the 10 cm thick water phantom (100 cm from the target) and behind an additional air gap of 40 cm. These spectra are shown in Figure 10. While the energy spectra change appreciably with distance from the target, the differences between the energy spectra for the small and large aperture are decreasing for increasing air gap. Therefore it might be necessary to do dose calibrations of an EPID for several air gaps, whereas a spatial variability of the spectrum within the portal plane might be negligible. These issues will depend critically on the degree of the energy dependence of the EPID itself.

Conclusion

The extended MSM offers the possibility to calculate dose distributions, energy fluence maps, and energy spectra for static and dynamic MLC fields by MC simulation. Comparisons to results from film dosimetry show good agreement for all cases investigated in this study. The extended MSM is not only able to calculate accurate dose distributions in the patient or phantom. The calculations of energy fluence maps allows the comparison with fluence maps used in treatment planning systems for IMRT and in other MC models for arbitrary MLC fields [3, 4, 5]. The possibility to precalculate portal dose distributions is important in terms of IMRT verification. These distributions could also be used as reference images for EPIDs. Furthermore, the extended MSM can serve for more investigational purposes, such as the analysis of the scatter contribution of the leaves for very small slits or of the influence of the leaf sequence on the energy spectra. Another possible usage is benchmarking and calibration of portal imaging devices. In summary, the MSM is a very flexible tool to investigate in detail a variety of dosimetric questions in radiotherapy.

References

[1] Ahnesjö, A., Saxner, M., Trepp, A.: A pencil beam model for photon dose calculation. Med. Phys. **19** (1992) 263-273.

[2] Arnfield, M., Siebers, J., Kim, J., Wu, Q., Keall, P., Mohan, R.: A method for determining multileaf collimator transmission and scatter for dynamic intensity modulated radiotherapy. Med. Phys. **27** (2000) 2231-2241.

[3] Bakai, A., Laub, W. U., Nüsslin, F.: Compensators for IMRT-An Investigation in Quality Assurance. Z. Med. Phys. **11** (2001) 15-22.

[4] Chetty, I., DeMarco, J., Solberg, T.: A virtual source model for Monte Carlo modeling of arbitrary intensity distributions. Med. Phys. **27** (2000) 166-172.

[5] Deng, J., Pawlicki, T., Chen, Y., Li, J., Jiang, S., Ma, C.: The MLC Tongue-and-Groove Effect on IMRT Dose Distributions. At: World Conference in Chicago, July 23-28 2000. Med. Phys. **27** (2000).

[6] Fix, M., Keller, H., Born, E., Rüegsegger, P.: Single source models for Monte Carlo dose calculations in radiotherapy. Med. Phys. **25** (1998) A187.

[7] Fix, M. K., Keller, H., Rüegsegger, P., Born, E. J.: Simple beam models for Monte Carlo photon beam dose calculations in radiotherapy. Med. Phys. **27** (2000) 2739-2747.

[8] Fix, M. K., Stampanoni, M., Keller, H., Born, E. J., Mini, R., Ruegsegger, P.: A Multiple Source Model for 6 MV photon beam dose calculations using Monte Carlo. Phys. Med. Biol. **46** (2001) 1407-27.

[9] LoSasso, T., Chui, C., Ling, C.: Physical and dosimetric aspects of a multileaf collimation system used in the dynamic mode for implementing intensity modulated radiotherapy. Med. Phys. **25** (1998) 1919-1927.

[10] Mackie, T., Scrimger, J., Battista, J.: A convolution method of calculating dose for 15 MeV x rays. Med. Phys. **12** (1985) 188-196.

[11] Mohan, R., Chui, C., Lidofsky, L.: Differential pencil beam dose computation model for photons. Med. Phys. **13** (1986) 64-73.

[12] Spirou, S., Chiu, C.: Generation of arbitrary intensity profiles by dynamic jaws or multileaf collimators. Med. Phys. **21** (1994) 1031-1041.

[13] Stein, J.: Investigations on intensity modulated treatment techniques in conformal radiotherapy. Ph.D. Thesis University of Heidelberg (1997).

[14] Wang, X., Spirou, S., LoSasso, T., Stein, J., Chui, C., Mohan, R.: Dosimetric verification of intensity modulated fields. Med. Phys. **23** (1996) 317-327.

[15] Webb, S.: Intensity-modulated radiation therapy. Chapter 3-4, pp 75-297, Institute of Physics Publishing, Bristol and Philadelphia.

[16] Werner, B., Das, I., Salk, W.: Dose perturbation at interfaces in photon beams: Secondary electron transport. Med. Phys. **17** (1990) 212-226.

[17] Woo, M., Cunningham, J.: The validity of the density scaling method in primary electron transport for photon beams. Med. Phys. **17** (1990) 187-194.

Correspondence to:

Michael Fix
Institute for Biomedical Engineering
University and ETH Zurich
Moussonstrasse 18
CH-8044 Zurich

Table 1. List of all sources defined in the MSM. Each jaw of the secondary collimator was defined as two planar sources, corresponding to the beam size defining surface and the bottom surface of the jaw, respectively. The electron and positron contamination of the beam was considered by defining one source at the bottom surface of the mirror.

head component	source type	# of source(s)	particle type of the source
target	line	1	photons
prim. collimator	planar	1	photons
flattening filter	planar	1	photons
mirror	planar	1	electrons/positrons
sec. collimator X1	planar	2	photons
sec. collimator X2	planar	2	photons
sec. collimator Y1	planar	2	photons
sec. collimator Y2	planar	2	photons

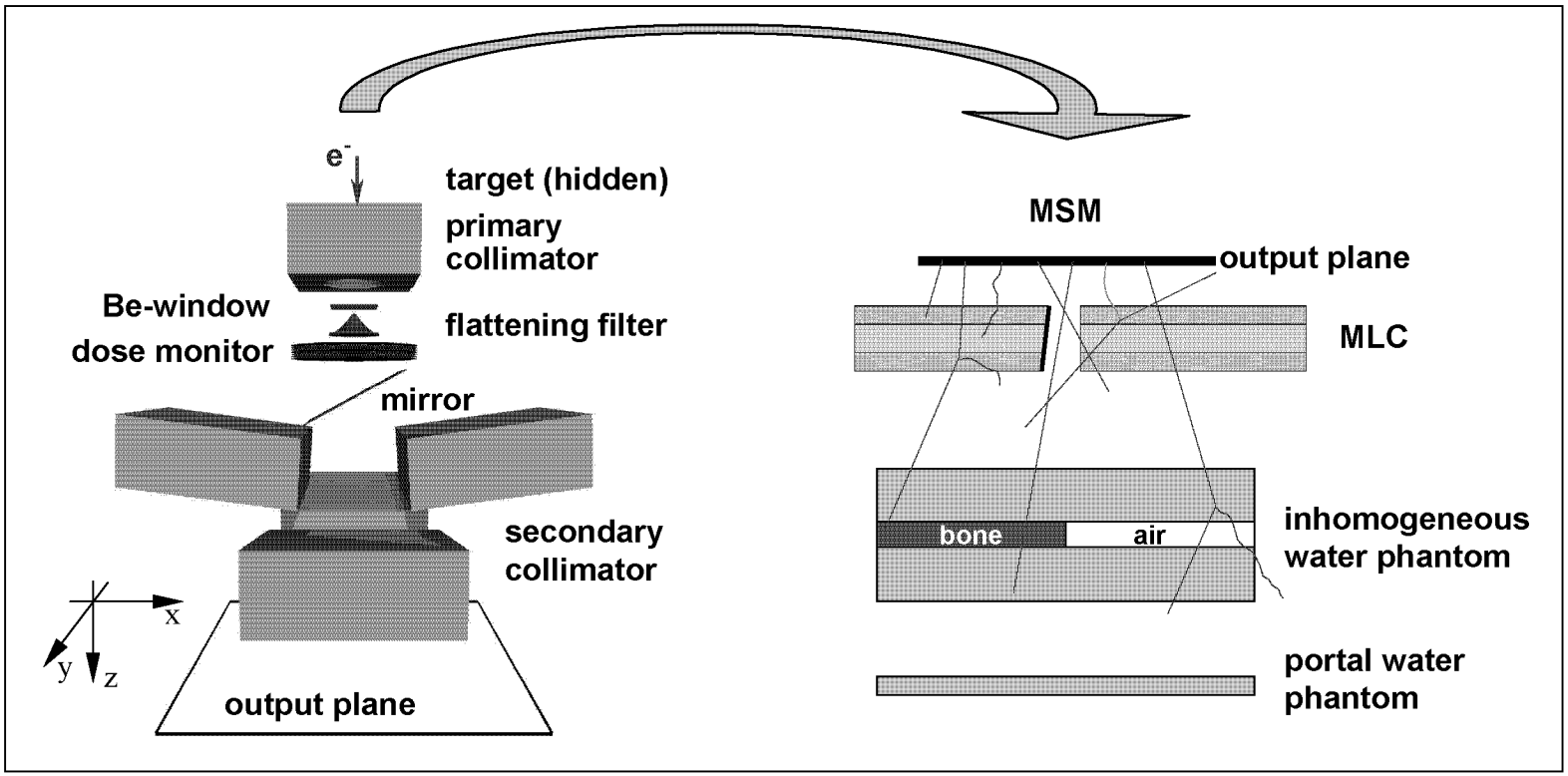

FIG. 1. Geometry of the accelerator head implemented in the MC code to generate the phase space data (left). An electron pencil beam hits the target at the central axis. Below the two pairs of secondary collimator jaws, the output plane is located perpendicularly to the central axis and used as the scoring plane for the phase space files. The MSM defines the particles' starting parameters in the output plane (right) downstream to the MLC and the phantom configuration.

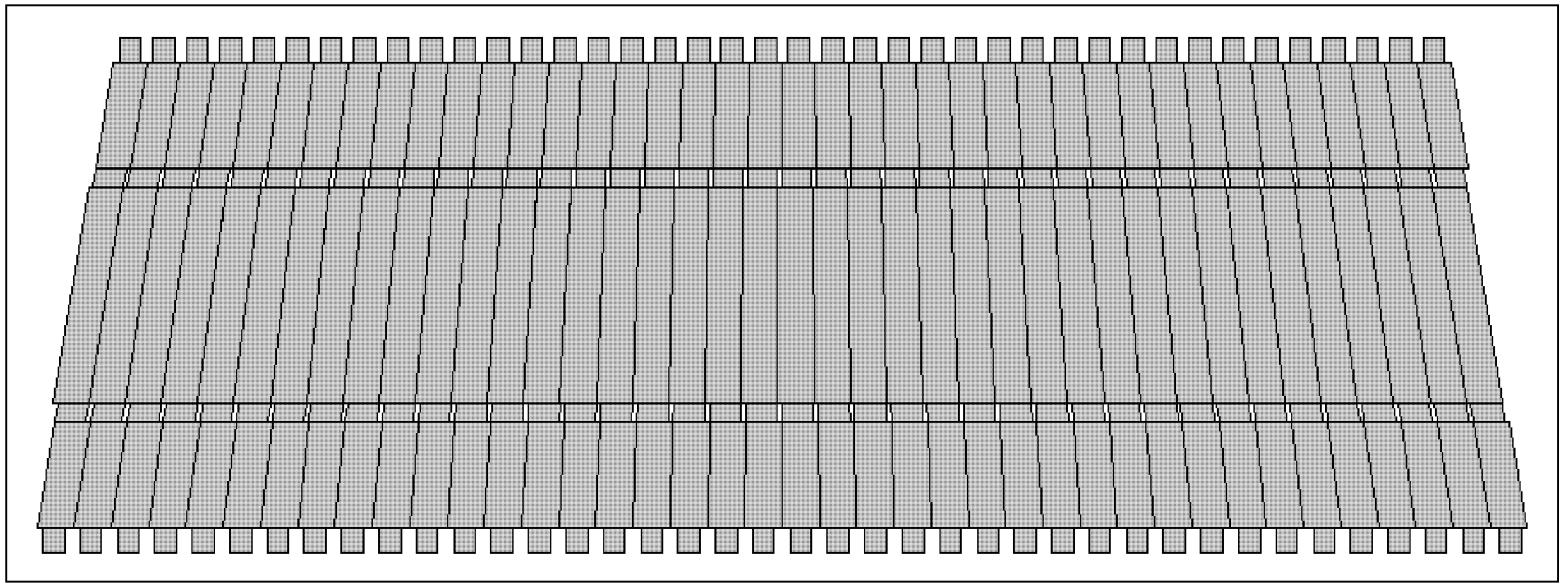

FIG. 2. Cross section of the MLC modeled for the MC simulations. The tongue and groove of the leaves were fully modeled.

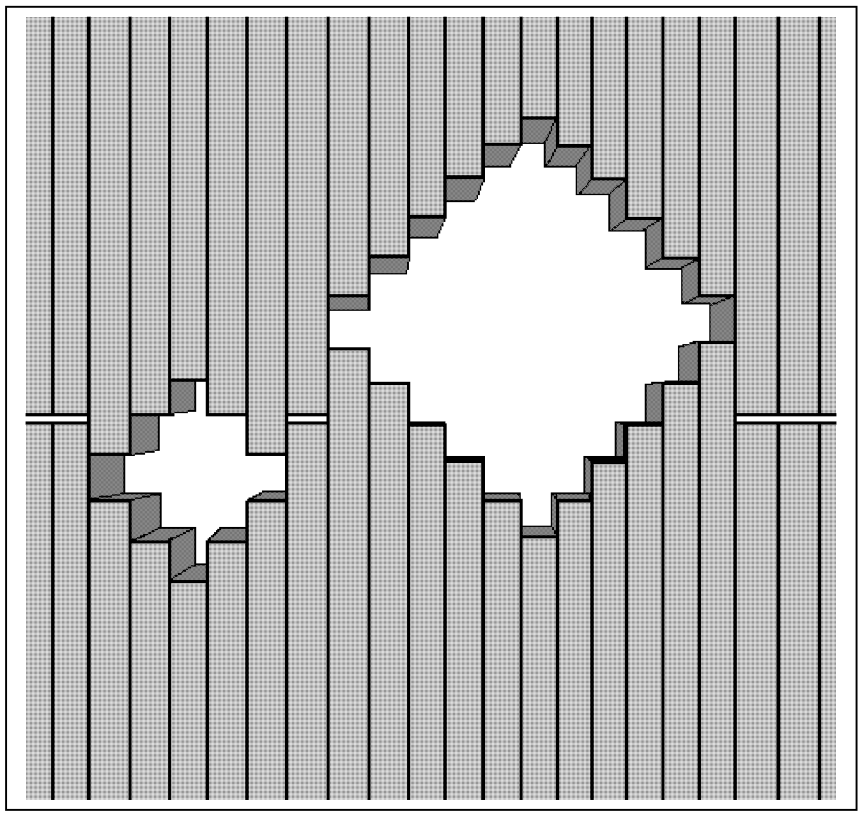

FIG. 3. MLC shape of the static field used to simulate energy fluence and dose distributions. The MLC is shown as seen from the isocenter.

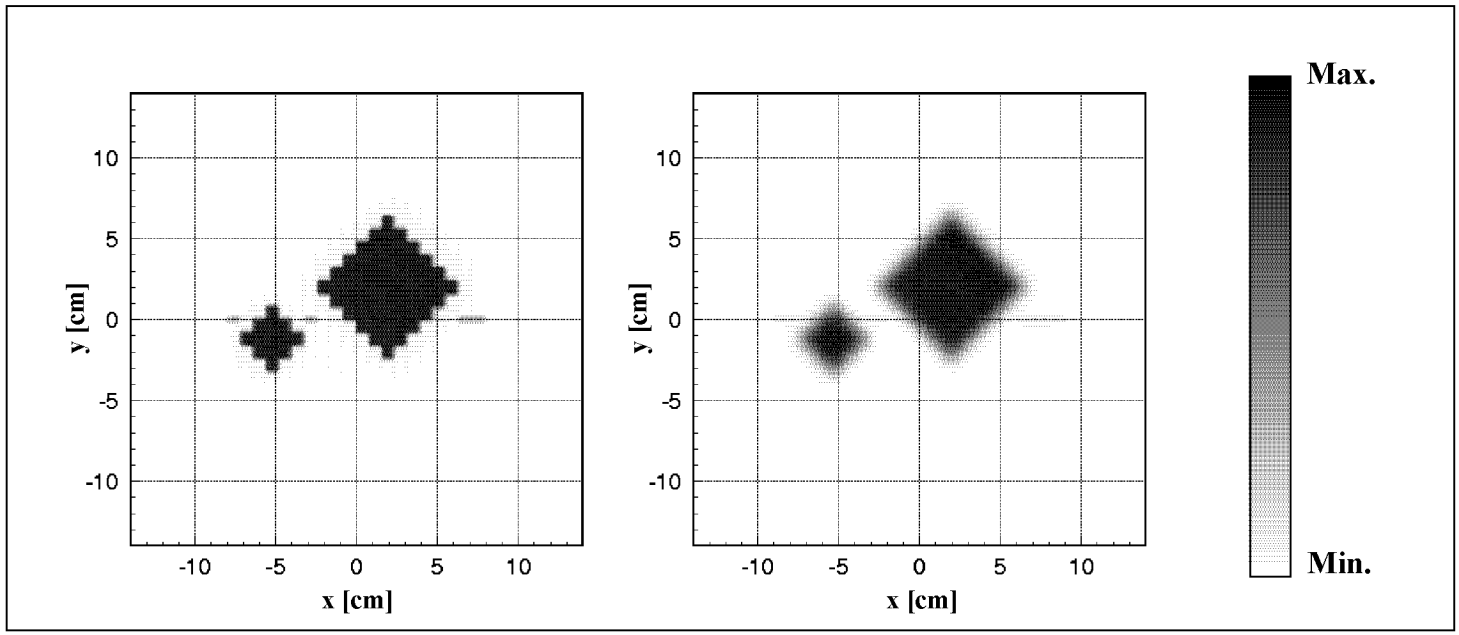

FIG. 4. The energy fluence distributions (SDD = 80 cm) of the static MLC case for all MSM sources (left) and for the primary collimator (right). The energy fluence contribution of the primary collimator is about 3% in the center of the open beam area.

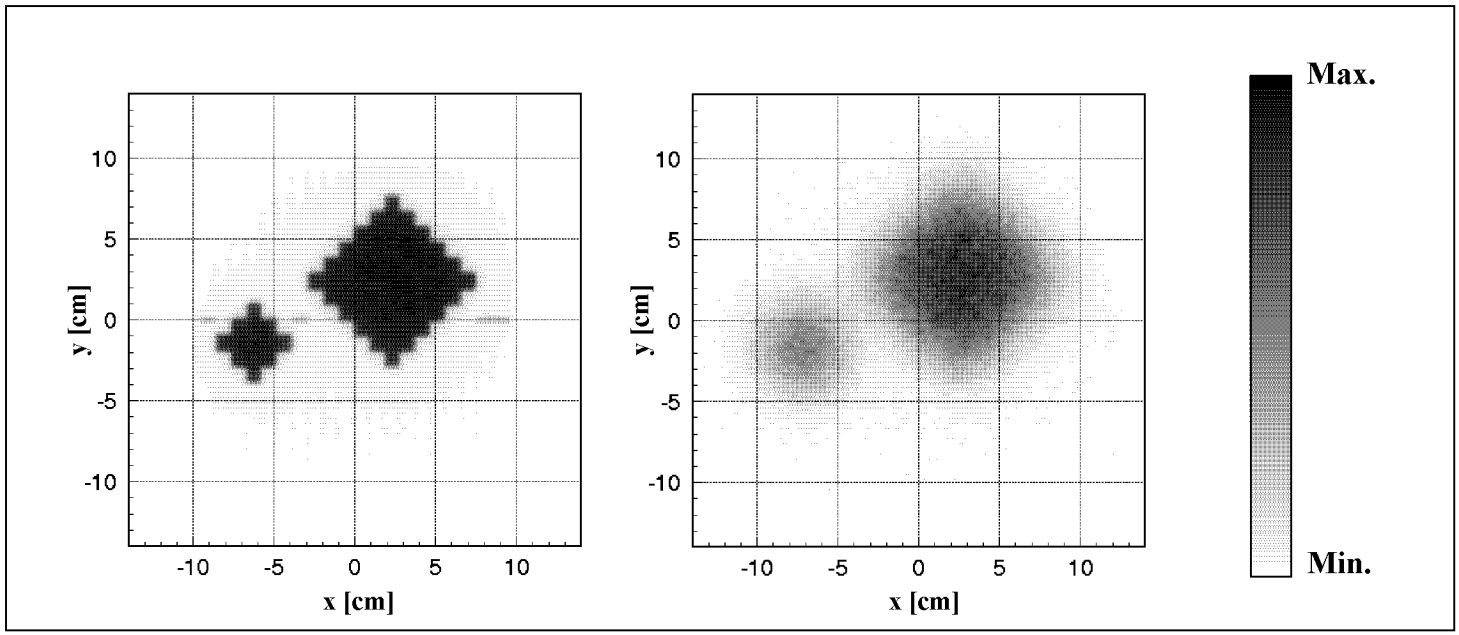

FIG. 5. The dose distribution of the static MLC case in a water depth of 5 cm (SSD = 90 cm) for all MSM sources (left) and for the flattening filter (right). The dose contribution of the flattening filter is about 4% in the center of the open beam area.

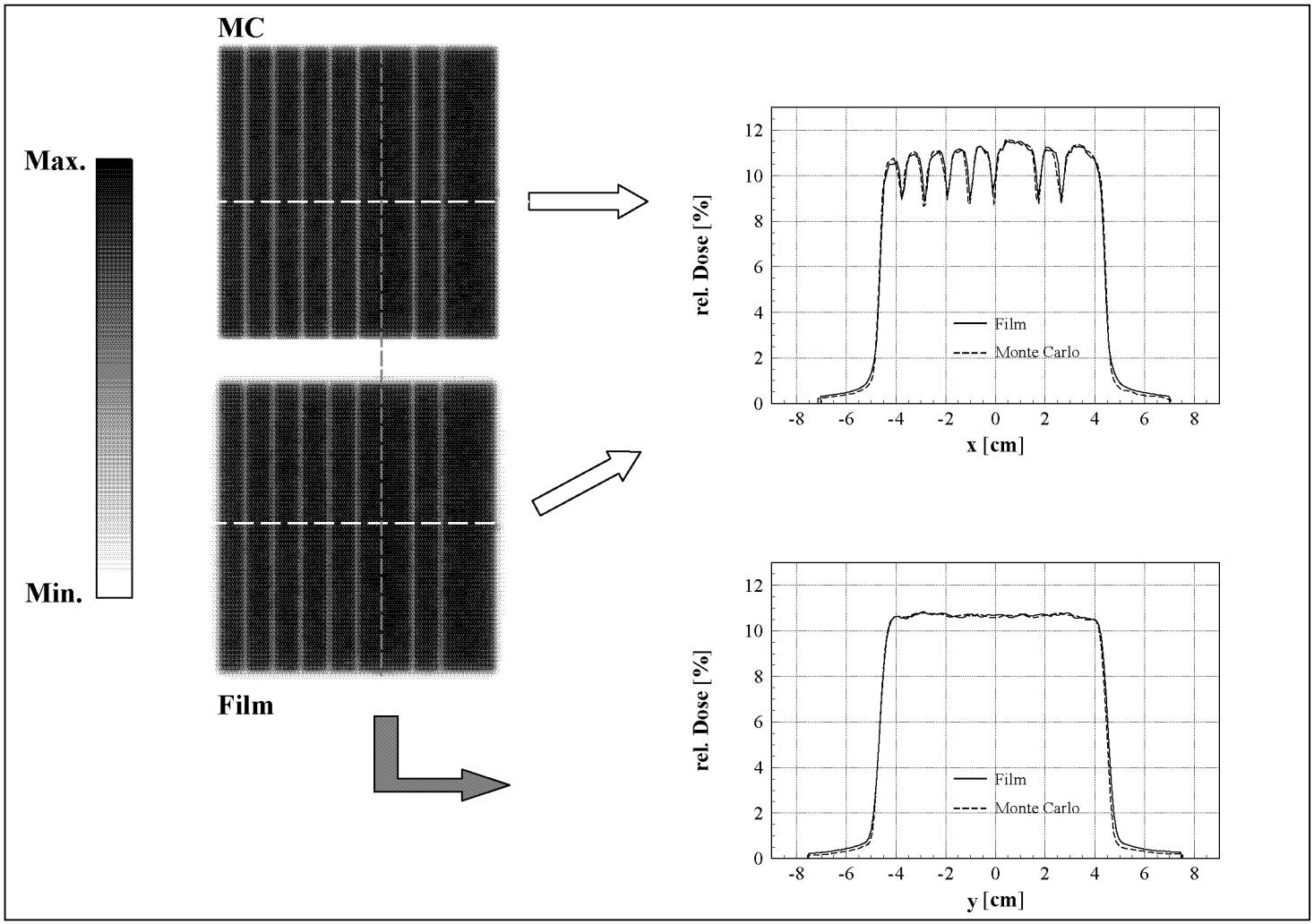

FIG. 6. The dose distribution in depth of dose maximum of the MC calculation (left top) and film measurement (left bottom) together with a comparison of profiles (right) along the x- and y-direction, respectively, for the step and shoot case. The area under the profiles was normalized to 100 %cm.

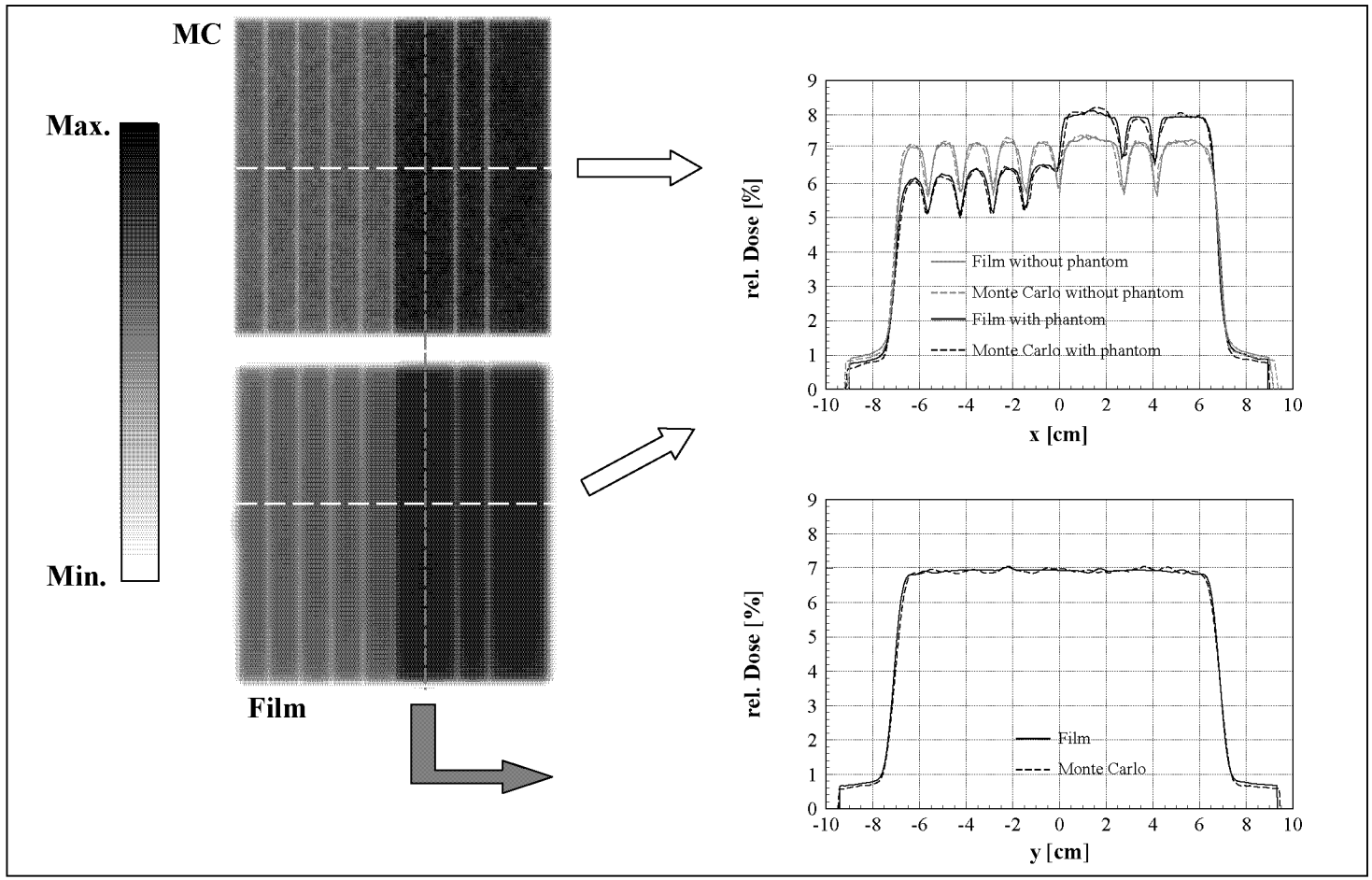

FIG. 7. The portal dose distribution in a water depth of 3 cm of the MC calculation (left top) and film measurement (left bottom) together with a comparison of profiles (right) along the x- and y-direction, respectively, for the step and shoot case with an inhomogeneous phantom was in the beam. In addition, the portal dose profile along the x-direction calculated without phantom in the beam is depicted for comparison. The area under the profiles was normalized to 100 %cm.

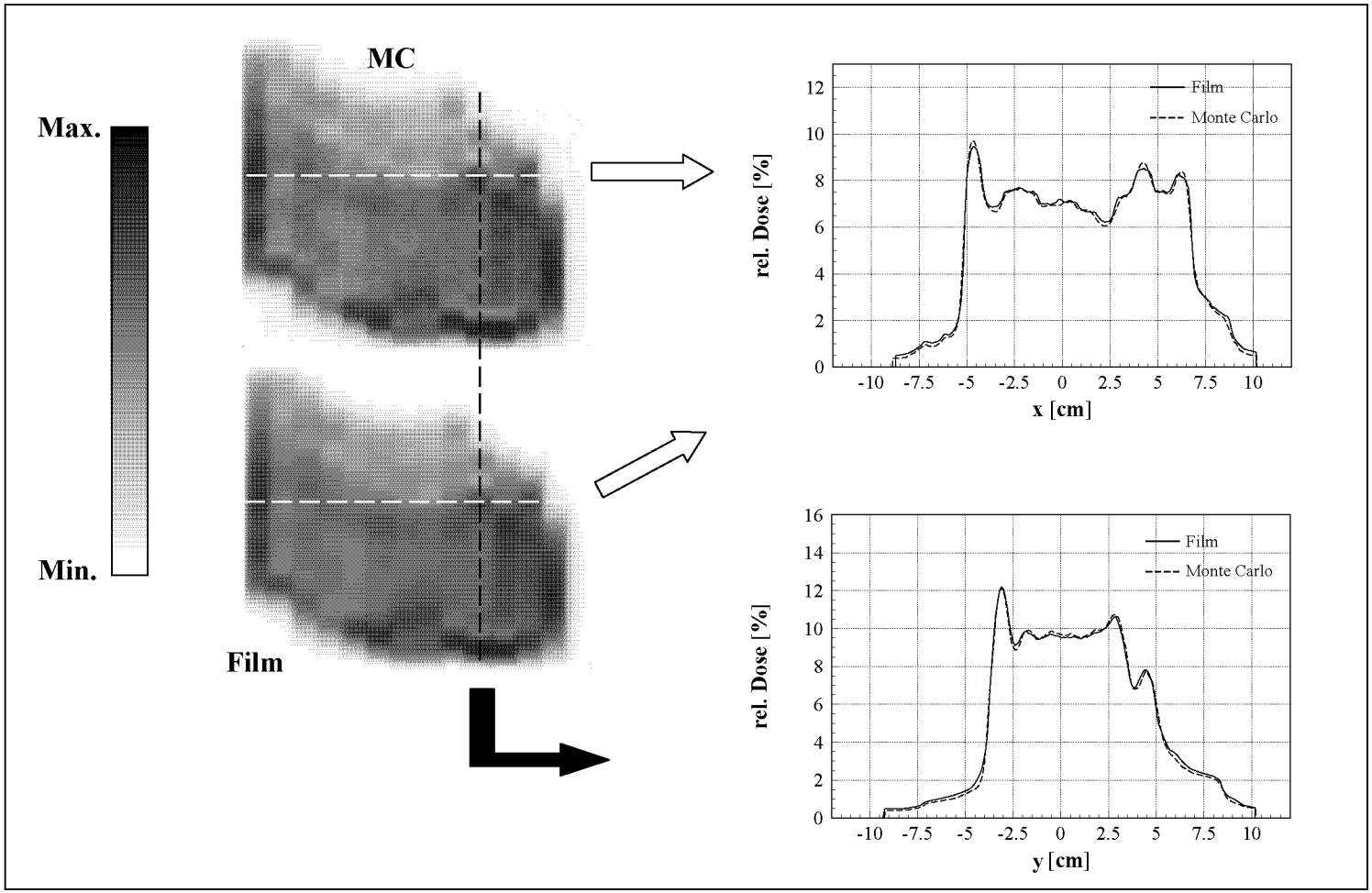

FIG. 8. The dose distribution in a water depth of 10 cm of the MC calculation (left top) and film measurement (left bottom) together with a comparison of profiles (right) along the x- and y-direction, respectively, for the head and neck case. The area under the profiles is normalized to 100 %cm. For statistical reasons, the MC profiles are smoothed by means of averaging dose values resulting in a dose matrix with a lower resolution.

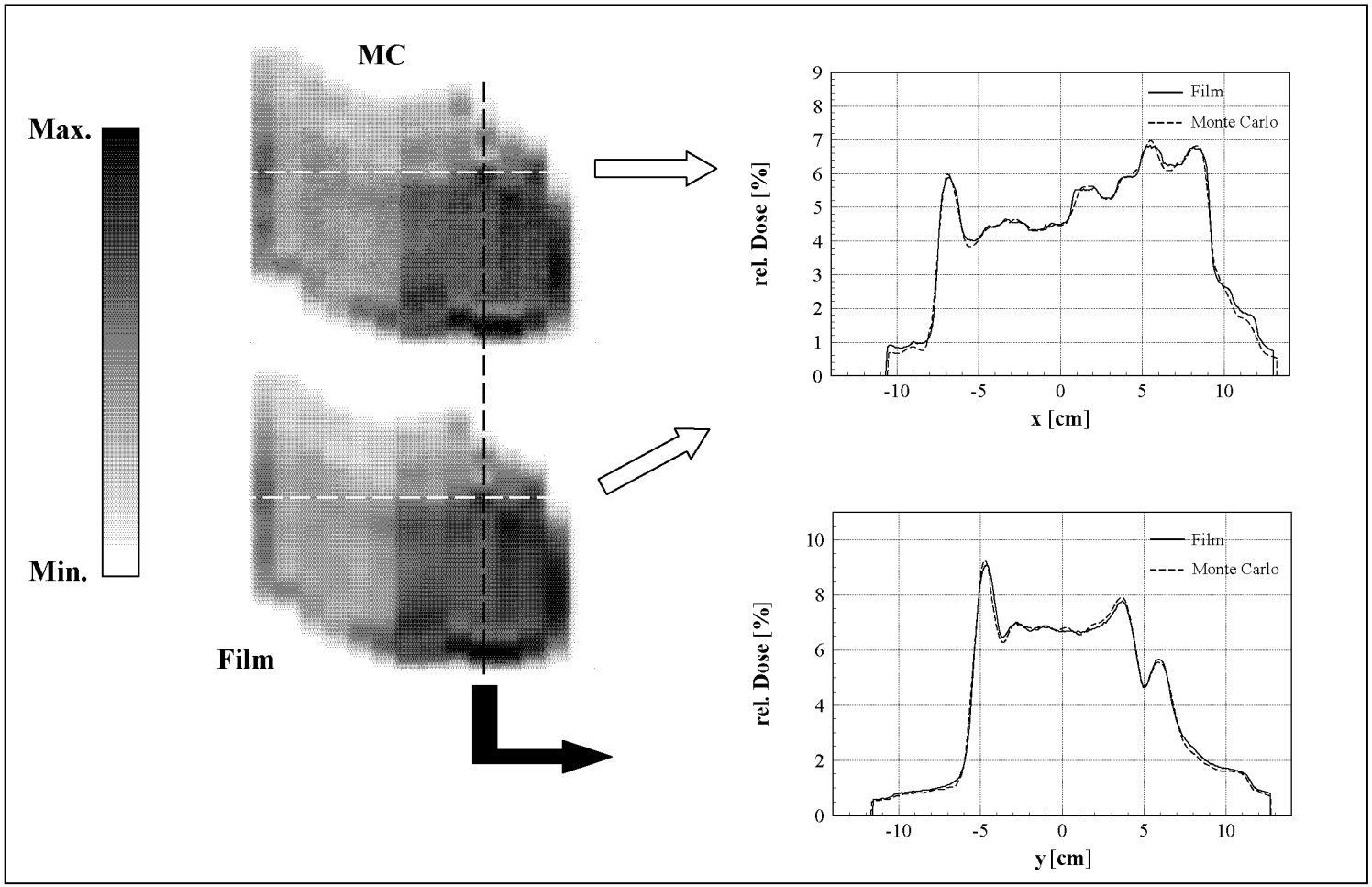

FIG. 9. The portal dose distribution in a water depth of 3 cm the MC calculation (left top) and film measurement (left bottom) together with a comparison of profiles (right) along the x- and y-direction, respectively, for the head and neck case. The area under the profiles is normalized to 100 %cm. For statistical reasons, the MC profiles are smoothed by means of averaging dose values resulting in a dose matrix with a lower resolution.

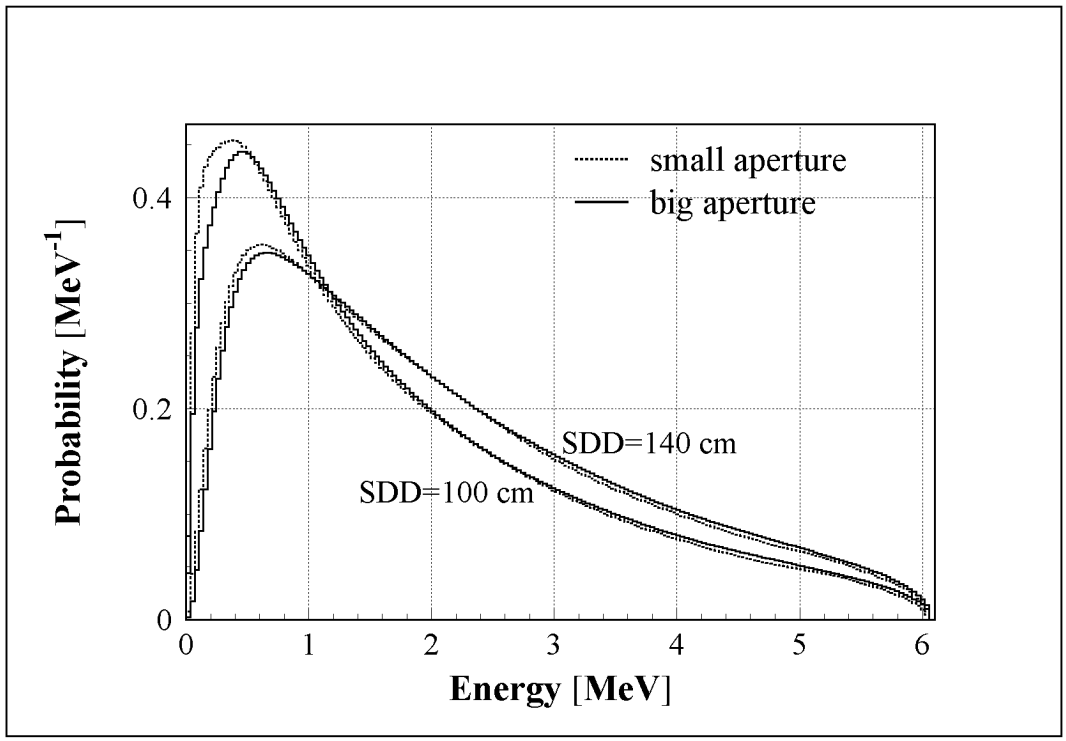

FIG. 10. The energy spectra in two portal planes (100 and 140 cm from the target) under the small and the big aperture of the static MLC field (see Fig. 3). The area under the spectra was normalized to 1.

6

Monte Carlo simulation of a dynamic MLC based on a multiple source model

published in
Physics in Medicine and Biology
2001, Vol. 46, No. 12, 3241-3257

Monte Carlo simulation of a dynamic MLC based on a multiple source model

Michael K. Fix and Peter Manser

Institute for Biomedical Engineering, University of Zurich and Swiss Federal Institute of Technology (ETH), Moussonstrasse 18, CH-8044 Zurich, Switzerland

Ernst J. Born and Roberto Mini

Division of Medical Radiation Physics, Clinic of Radio-Oncology, Inselspital, University of Berne, CH-3045 Berne, Switzerland

Peter Rüegsegger

Institute for Biomedical Engineering, University of Zurich and Swiss Federal Institute of Technology (ETH), Moussonstrasse 18, CH-8044 Zurich, Switzerland

Short title: Monte Carlo simulation of a dynamic MLC

Abstract

Detailed knowledge of the characteristics of the radiation field shaped by a multileaf collimator (MLC) is essential in intensity-modulated radiotherapy (IMRT). A previously developed multiple source model (MSM) for a 6 MV beam was extended to a 15 MV beam and supplemented with an accurate model of an 80-leaf dynamic MLC. Using the supplemented MSM and the MC code GEANT, lateral dose distributions were calculated in a water phantom and a portal water phantom. A field which is normally used for the validation of the step and shoot technique and a field from a realistic IMRT treatment plan delivered with dynamic MLC are investigated. To assess possible spectral changes caused by the modulation of beam intensity by an MLC, the energy spectra in five portal planes were calculated for moving slits of different widths.

The extension of the MSM to 15 MV was validated by analysing energy fluences, depth doses and dose profiles. In addition, the MC-calculated primary energy spectrum was verified with an energy spectrum which was reconstructed from transmission measurements. MC-calculated dose profiles using the MSM for the step and shoot case and for the dynamic MLC case are in very good agreement with measured data from film dosimetry. The investigation of a 13-cm wide field shows an increase in mean photon energy of up to 16% for the 0.25 cm slit compared to the open beam for 6 MV and of up to 6% for 15 MV, respectively.

In conclusion, the MSM supplemented with the dynamic MLC has proven to be a powerful tool for investigational and benchmarking purposes or even for dose calculations in IMRT.

1. Introduction

Simulation of the radiation transport by the Monte Carlo technique is known to be the most accurate method for dose calculation in radiotherapy (Rogers and Bielajew 1990, Andreo 1991, Mohan 1997, DeMarco *et al* 1997, Hartmann Siantar *et al* 1997, Ma *et al* 1999). However, it requires an accurate description of the radiation beams applied to the patient. For MC techniques a radiation beam can best be characterized by the phase space parameters (location, direction of motion, energy) of a large number of beam particles (photons, electrons, positrons) traversing a plane perpendicular to the central axis above the patient (Lovelock *et al* 1995, van der Zee and Welleweerd 1999, Deng *et al* 2000a). This precalculated phase space (PS) data result in a large PS file. Alternatively, to reduce the large storage amount required for this beam description, a beam model can be extracted from the PS data by grouping the particles in the PS file in reasonable classes constituting physically meaningful subsources and by parametrizing the associated distributions as, e.g. the energy and angular distributions. Such a multiple source model (MSM) must also include a procedure for sampling particles from these distributions in order to reproduce the PS data (Rogers *et al* 1995, Ma *et al* 1995, 1997, Schach von Wittenau *et al* 1999, Deng *et al* 2000a).

PS data and MSMs usually describe the beam in a plane positioned either above or below the secondary collimator. Patient-dependent beam modifiers such as wedges, compensators and multileaf collimators (MLCs) change the beam characteristics and necessitate a modification of the PS data. Approximate methods for PS data modifications were suggested by Deng *et al* (2000b), Siebers *et al* (2000), Chetty *et al* (2000), Fogg *et al* (2000), Shih (2000), Shih *et al* (2001), Laub *et al* (2001), Verhaegen (2001). Alternatively, the beam modifiers can be included in the simulation of the radiation transport through the patient (Jiang and Ayyangar 1998, Verhaegen and Das 1999, Li *et al* 2000, Fix *et al* 2001a). The need to accurately characterize this patient-dependent modifiers becomes obvious with the introduction of intensity-modulated radiotherapy (IMRT). Furthermore, when using the MLC in IMRT (step and shoot technique or dynamic MLC) rather small field segments are often applied so that ap-

preciable changes in the characteristics of the radiation beam reaching the patient are expected.

This work first describes the extension of a previously developed 6 MV MSM (Fix *et al* 2001b) to a 15 MV beam. The MSM is able to reproduce the PS data for rectangular fields in a plane below the secondary collimator. To investigate the influence of the MLC on the beam characteristics the MSM is then supplemented with the MLC. For this purpose, an accurate model of the MLC is included in the simulation process. The supplemented MSM is able to handle static, step and shoot and dynamic MLC fields. In this paper it is used to calculate dose profiles for step and shoot and for dynamic IMRT fields at patient distance. To do patient-specific IMRT quality assurance and verification the direct comparison of calculated and measured portal dose images becomes increasingly important. Therefore it is essential to have accurate, calculated portal dose images. It is shown that the supplemented MSM is able to calculate portal dose images for step and shoot and for dynamic IMRT fields. For a number of dynamic slit beam irradiations the dependence of the beam characteristics (radiation components, energy spectra) on the slit width is investigated. Such data are important in assessing the accuracy of treatment planning algorithms and in attempts to calibrate electronic portal imaging as dosimetric tools for patient quality assurance in IMRT.

2. Materials and Methods

2.1. Multiple source model (MSM) 15 MV

To define the sources of the MSM, the radiation transport through the main elements of the beam defining system of the Varian Clinac 2300 C/D (figure 1, left part) was simulated by means of the MC code GEANT 3.21 (Release 99) (CERN 1995). Manufacturer specifications were used to define dimensions and materials for the accelerator elements. Instead of starting with a monoenergetic electron pencil beam on the surface of the target for the 6 MV beam (Fix *et al* 2001b) a monoenergetic, parallel beam of constant intensity within a circular area was used for the 15 MV beam. While the depth dose is sensitive to the energy of the initial electrons, the dose profiles are sensitive to both the energy and the diameter of the initial electron beam (Fix *et al* 2000, Lovelock *et al* 1995, Faddegon *et al* 1999, Sheikh-Bagheri 1998). For this reason, the energy of the electrons and the diameter of the beam area were tuned to obtain correct depth dose data for the 10 x 10 cm^2 field and correct profiles for the 30 x 30 and 40 x 40 cm^2 fields. Comparisons with measured depth dose curves and profiles led to an effective kinetic energy of 15.0 MeV for the primary electrons and a diameter of 0.3 cm for the circular beam area, which is similar to the one given by Ma *et al* (1999) and Schach von Wittenau *et al* (1999). The output plane was located at a distance of 44.7 cm from the target (just below the secondary collimator jaws; figure 1). In the output plane PS data were generated for a set of square fields (3 x 3, 5 x 5, 8 x 8, 10 x 10, 15 x 15, 20 x 20, 30 x 30, and 40 x 40 cm^2 at isocenter distance) using 10 keV as the (kinetic) cut-off energy for the photons and for the charged particles. The number of starting primary electrons to produce the PS data was chosen in order to enable an accurate parametrization of the sources in the MSM. They ranged from 3000 million for the smallest field to 200 million for the largest field, corresponding to about 2.3 and 18 million entries in the PS files, respectively. Since for small fields most particles of the beam are absorbed in the secondary collimator, the number of starting primary electrons has to be larger.

The PS data were analysed analogously as described in Fix *et al* (2001b). In contrast to the 6 MV case, the target for the 15 MV beam was modelled as a planar source

with a diameter of about 3 mm corresponding to the diameter of the beam of primary electrons. All other sources describing the primary collimator, flattening filter and secondary collimator jaws as photon sources and the mirror as a source of charged particles contaminating the beam were similar to the ones for the 6 MV beam.

The same interpolation algorithm and sampling procedure as described by Fix *et al* (2001b) were used for the 15 MV beam. The interpolation algorithm allows the MSM to produce PS data for arbitrary rectangular fields containing the central 3 x 3 cm^2 field and the sampling procedure describes how to determine the parameters of a photon or charged particle starting from the MSM. Thereby, the particle type and the MSM source of the particle are sampled according to the weights determined from the PS data. The starting point of the particle is sampled from the spatial particle fluence distribution in the output plane. The starting direction is determined by the line between the starting point and a randomly chosen origin point of the particle on the corresponding head component of the linear accelerator. The distribution of the origin points was established by tracing the particles in the PS files backwards from the output plane to the surface of the head component of the accelerator head. At last, an energy is sampled using the corresponding energy distribution defined in the output plane.

Comparisons of energy fluences determined from the original PS data with those from PS data reproduced from the MSM and of calculated depth doses and profiles for several fields with measured values were performed to investigate the accuracy of the MSM. In order to additionally validate the MC simulations, the calculated target energy spectrum of the accelerator was compared with the measured one using an independent empirical numerical method introduced by Francois *et al* (1993). They performed the reconstruction of the energy spectrum from transmission data by direct resolution of a matrix system using spectral algebra. The algorithm described in Francois *et al* (1993) and Catala *et al* (1995) was implemented in Mathematica (Stampanoni *et al* 2001), which guarantees a high precision numeric solution. The attenuator material was made of high-purity carbon (>99.5%; type Ellor$^+$ 20) and a Farmer ionization chamber (type 2571) was used for the transmission measurements.

The dose measurements were performed in a 50 x 50 x 40 cm^3 water phantom. For field sizes larger than 20 x 20 cm^2 dose was measured by a Scanditronix 0.12 cm^3 RK

ionisation chamber and for all other measurements, a Scanditronix p-type shielded Si diode detector was utilized.

2.2 Dynamic MLC

In this work, an 80-leaf Varian MLC was modelled and included in the radiation transport simulation from the output plane downstream (figure 1, right part). Figure 2 illustrates a cross section through the MLC leaves. Each leaf consists of seven partitions of tungsten with a total height of 6.1 cm (figure 2). Every leaf has a projected width of 1 cm in the isocentric plane and can be moved in this plane over the whole 40 x 40 cm^2 field. The dimensions and the material for the leaves were chosen according to the manufacturer's specifications. Thus, the tongue and groove design used to reduce inter-leaf radiation leakage was taken into account. Since the definition of rounded forms for the leaf front ends is not straightforward in GEANT, they were modelled as plane surfaces inclined according to the actual beam divergence. Therefore, this implementation of the MLC does not account for the rounded form of the leaf front ends. However, an additional shift between two opposite leaves was implemented as a correction. The concept of this correction has been investigated by Wang *et al* (1996), LoSasso *et al* (1998) and Arnfield *et al* (2000). In our MLC model a shift of 1.2 mm was used according to measurements of Arnfield *et al* (2000), whose method is based on dynamic uniform fields. The upper surface of the MLC is located 3.2 cm below the output plane (figure 1, right part). If a starting particle from the MSM interacts with a leaf of the MLC, this particle, as well as all secondary particles produced, are tagged to be assigned to the MLC source. Thus, the MLC is an additional photon and charged particle source in the MSM.

The supplemented MSM for the 15 MV beam was used to calculate three items: dose distributions in the water phantom, portal dose distributions in the portal water phantom (figure 1) and energy spectra and energy fluences in planes perpendicular to the central axis of the field. In addition the last item was also performed using the MSM for 6 MV.

Lateral dose distributions in the water phantom (30 x 30 x 25cm^3) were calculated at SSD = 90 cm for water depths of 2.5, 5, 10 and 20 cm. For portal dose calculations a

30 x 30 x 9 cm^3 portal water phantom at a distance of 140 cm from the target was implemented (figure 1) and dose distributions were determined at a depth of 5 cm therein. Portal dose distributions were calculated with and without a water phantom (30 x 30 x 25 cm^3; SSD = 90 cm) which contained two inhomogeneities: one half of the central 4-cm thick layer consisted of air and the other half of bone (figure 1, right part). As a first example, a step and shoot arrangement of seven segments for a 12 x 12 cm^2 field was considered which formed a pyramidal dose distribution normally used for benchmark purposes in treatment planning systems. The number of primary particles in the MC calculations was 200 million per segment. These dose distributions were compared with the corresponding film measurements using Kodak X-Omat V films. For film dosimetry phantoms consisted of slabs of solid water RMI 451 and bone material RMI 450 (Gammex RMI) with films positioned between the slabs. As a second example, a dynamic MLC field taken from a potential treatment plan of a bronchus carcinoma was investigated in order to test the MSM in a clinical situation of IMRT. For this purpose, the considered dynamic MLC file created by an inverse planning system served as input for the MC calculation. The dynamic MLC file contains leaf positions as a function of monitor units and is used by the MLC controller to apply the intensity-modulated field dynamically during beam delivery. For the bronchus case, the dynamic field was approximated by discretization in 178 static segments on the basis of the dynamic MLC file, which was created by the treatment planning system. Thereby, the fraction of monitor units delivered in each segment was kept constant. MC results for the dynamic field were then produced by accumulating the corresponding results for each segment. MC dose calculations in the water phantom and portal dose distributions were compared to measured data from film dosimetry. The number of primary particles in the MC calculation was 75 million per segment. The dose scoring voxels were 0.1 x 0.1 x 1.0 cm^3 in all MC simulations and the (kinetic) cut-off energies for the photons and the charged particles were set equal to 10 keV in all MC calculations.

In IMRT the intensity pattern is characterized by large and closely spaced variations, which might result in small segments. Therefore, the knowledge of influence of the dynamic MLC on energy spectra for these small segments is very important not only for dosimetric aspects but also for calibration purposes of electronic portal imag-

ing devices (EPIDs). The supplemented MSM is, apart from dose calculations, suitable for this kind of investigation. For this reason, several dynamic MLC files, each containing 150 segments, have been created, which describe moving slits of several widths (4, 2, 1, 0.5 and 0.25 cm) crossing a 20 x 13 cm^2 field along the *y*-direction. Photon energy spectra and energy fluences for both energies, 6 and 15 MV, were then determined in portal planes perpendicular to the central axis at distances of 100, 110, 120, 130 and 140 cm from the target. For the 6 MV beam the MSM described in Fix *et al* (2001b) was used. The simulations were performed without a phantom and with a water phantom of 30 x 30 x 25 cm^3 and SSD = 75 cm in the beam. In addition, these calculations were done for the open field size of 20 x 13 cm^2 to obtain a reference situation. The number of starting particles was so chosen that each point in the portal plane is exposed to the same target fluence through the slit. The number of starting particles for the slit with a width of 4 cm was set equal to 100000 per segment. The (kinetic) cut-off energies for the photons and the charged particles were set equal to 10 keV in all MC calculations.

3. Results and Discussion

3.1. Multiple source model (MSM) 15 MV

As a first validation of the MSM figure 3 shows the energy fluence distributions along the x-axis (respectively y-axis) determined with both the PS data reproduced with the MSM and the original PS data for the 40 x 40 cm^2 field. The statistical uncertainty in these calculations is about 1%. The contributions of the components are normalized to the target energy fluence, which is set equal to 100% on the central axis. On the right-hand side the scatter components are shown in more detail. The unsharp beam boundary for the flattening filter as well as for the primary collimator is caused by the spatial extent of these sources and is correctly reproduced by the MSM. Due to the different distances from the target to the secondary collimator jaws and from there to the output plane, different energy fluences in the x- and y-directions are observed. In general, the MSM reproduces the PS data within an accuracy of about 1%.

The comparison of the MC-calculated target energy spectrum with the reconstructed spectrum from an MC-independent numerical method is illustrated in figure 4. On the left-hand side the transmission measurements for carbon are depicted. The reconstructed energy spectrum and the MC-calculated target spectrum agree within 2.5% which suggests the correctness of the original PS data (figure 4). The statistical uncertainty of the MC-calculated energy spectrum around the maximum is less than 1%.

Besides comparing PS data, the feasibility of the beam model for dose calculations in radiotherapy has to be proven by comparing dose distributions with measurements. Figure 5(a) shows the calculated depth dose curve for the 10 x 10 cm^2 field using the MSM and original PS data, respectively, together with the measurement. The electron contamination in the build-up region reaches about 12%, which is comparable to the work of Zhu and Palta (1998) who found about 11% for an 18 MV beam. The dose decrease near the water depth of 20 cm is due to the lack of backscatter, since the thickness of the water phantom for the MSM dose calculations is only 20 cm. Measured dose profiles as well as the corresponding calculations using the MSM and the original PS data, respectively, for several field sizes are depicted in figure 5(b). The agreement between the calculations and the measurements is within 1% and 1 mm. In

order to test the fitting procedure the comparisons of the calculated depth dose curve and dose profiles at several depths of water with the corresponding measurements are illustrated in figure 5(c) and (d), respectively, for a field size of 9 x 17 cm^2. The deviation between calculated and measured dose distributions is less than 1% and 1 mm, which is comparable to the works of Liu *et al* (1997) and Ma *et al* (1998, 1999).

In all cases, the main scatter component after the build-up region is the flattening filter. In general, the difference between the MSM-calculated dose values and those using the original PS data and measurements, respectively, is very good and is within 1% and 1 mm.

3.2. Dynamic MLC

The results of the dose distributions for the step and shoot case are shown in figure 6 (left-hand side) for a depth of 5 cm in the water phantom. In the lower part of the dose distributions and in the isodose plots, the consequence of the tongue and groove effect is visible due to the segmentation of the step and shot case. This effect results in a dose reduction between the leaves of about 5% at a water depth of 20 cm and of about 10% at the depth of dose maximum for the MC calculations as well as for the film measurements. The statistical uncertainty around the maximum in the MC dose calculation is about 1%. On the right-hand side of figure 6 a profile for a quantitative comparison is depicted. The area under the profiles is normalized to 100%cm. The deviations between the measured and calculated profiles in the water phantom are within 2% and 1 mm for all water depths. Similar deviations result for the corresponding portal dose profiles.

The results for the bronchus case of the portal dose distributions in 140 cm distance from the target, where an inhomogeneous phantom was in the beam, are depicted in figure 7. The statistical uncertainty around the maximum in the MC dose calculation is about 1.5%. The quantitative results are shown as the dose profiles along the x- and y-direction where the area under the profiles is normalized to 100%cm. In addition, the portal dose profiles without a phantom in the beam are shown for comparison. The dose values below the air inhomogeneity increase whereas the bone inhomogeneity absorbs more radiation leading to lower dose values in the area underneath, as ex-

pected. Due to different scattering conditions slight differences in the profiles along the *y*-direction are present. Outside the radiation field the additional scattered radiation from the phantom is clearly visible. The calculated and measured portal dose profiles show an agreement within 2.5% and 1.5 mm. Figure 8 shows isodose plots of this case for a 2D comparison. Corresponding dose profiles in the water phantom agree within 2% and 1 mm. The deviations mainly appear in the extremes of the intensity modulations, which corresponds to results for dynamic MLC applications of the 6 MV beam (Fix *et al* 2001a).

In summary, the MC dose calculations of dynamic MLC fields coincide very well with the film measurements for all cases studied.

Typical results of the mean energy spectra for the 20 x 13 cm^2 field of the dynamically applied slits in a portal plane at a distance of 100 cm from the target are shown in figure 9 for 6 and 15 MV and with and without the water phantom. The area under the spectra is normalized to 1. The beam hardening which occurs for smaller widths of the slit is clearly visible and is more distinct for the 6 MV beam. In addition, a shoulder appears between 1.5 and 2 MeV for decreasing slit widths. The effect is weakened if a phantom is positioned in the beam (figure 9(c)). Since the portal plane is directly below the phantom, the increase of low-energy scatter radiation from the phantom compared with the unattenuated beam is evident. In order to explain the changes in the energy spectra, the contribution of the main sources for the 6 MV beam without phantom are depicted in figure 10. The target spectrum (figure 10(a)) becomes harder for decreasing widths of the slit due to the increasing attenuation of the MLC. The MLC as source, however, contributes more scattered radiation for decreasing slit widths (figure 10(d)). In figure 10(b) and (c), the reduction in head scatter from the primary collimator and flattening filter for smaller widths of the slit is noticeable, since the MLC increasingly hides the sources.

Figure 11 demonstrates the behaviour of the energy spectra with increasing air gap between the phantom and the portal plane for the 6 MV beam. While the energy spectra change appreciably with distance from the target, the differences between the energy spectra for different slit widths are weakly decreasing for increasing air gap. As expected, the low-energy radiation is reduced due to of the wider angular distribution of the scattered photons. Similar results were found by Jaffray *et al* (1990). However,

some changes in energy spectra are still visible at an air gap of 40 cm, which may be important for calibration purposes of EPIDs. In addition, the difference in energy between scatter and primary fluences will have some implications in the design of detectors and scatter rejection techniques for use at megavoltage energies.

The mean energy along the y-axis in a portal plane at a distance of 100 cm to the target is illustrated in figure 12 for both energies (with and without the water phantom). The increase in mean energy on the central axis between the open field and the slit width of 0.25 cm is 16 and 6% for 6 and 15 MV, respectively, if no phantom is in the beam. For 6 MV these changes are larger than the off-axis softening. This is in contrast to the 15 MV case (figure 12(b)), where both the off-axis softening and the change in the mean energy due to the reduction of the slit width are about 6%. The changes in the mean energy on the central axis decrease to 10 and 2% for 6 and 15 MV, respectively, when the phantom is in the beam (figure 12(c) and (d)). Another difference between 6 and 15 MV appears outside the geometric radiation field (figure 12(a) and (b)). If there is no phantom in the beam the mean energy drops at the field edge in the 15 MV case while such a behaviour for small slit widths is not visible for 6 MV. A more detailed analysis of the contributions of the MSM sources shows that this behaviour is caused by the increasing screening of the scattered low-energy photons by the MLC for decreasing slid widths for the 6 MV beam and by the increasingly forward-peaked radiation of scattered high-energy photons for the 15 MV beam. The mean energy along the x-axis in a portal plane at a distance of 100 cm to the target is illustrated in figure 13 for both energies (with and without the water phantom). Due to the tongue and groove design of the MLC, the mean energy increased below adjacent leaves. However, the general behviour of the mean energy is the same as along the y-axis.

The calculated energy fluence along the y-axis for all slit widths in the portal plane at a distance of 100 cm to the target is shown in figure 14. The curves are normalized to the energy fluence of the open field, which is set equal to 1 on the central axis. The increase in energy fluence of up to 40% for decreasing slit widths is due to transmission, scattered radiation and changes in the energy spectra. The energy fluence is almost flat and slightly increasing with increasing off-axis distance for 6 and 15 MV, respectively, when no phantom is in the beam. With the phantom in the beam, the en-

ergy fluence decreases with increasing off-axis distance, especially in the 6 MV case. In addition, the drop of the energy fluence near the field boundaries is smoother for all slits compared with the open beam, because the tongue and groove design of the leaves blurs the field edge. The analogous-calculated energy fluence along the x-axis is depicted in figure 15. Similarly to the mean energy also the mean energy fluence increases below adjacent leaves due to the tongue and groove design of the MLC. This increase is stronger for smaller slit widths, since the contributions of transmission and scatter radiation increase. However, the general behviour of the energy fluence is the same as along the y-axis.

The influence of the MLC on the beam characteristics has to be taken into account in treatment planning systems when segments with small slits are used in intensity-modulated fields. As a simple approach an effective, leaf-sequence-dependent, transmission could be used to describe the influence of the MLC.

4. Conclusions

In this paper we first extended the previously described MSM for the 6 MV beam of a Varian Clinac 2300 C/D to 15 MV by introducing a few modifications. PS comparisons show that the MSM reproduces the original PS data very accurately. In addition, the primary energy spectrum of the beam is in good agreement with the energy spectrum reconstructed from transmission measurements. Comparisons of depth dose curves and dose profiles coincide very well with dose distributions resulting from original PS data and with measurements.

The MSM allows the calculation dose distributions, portal dose distributions, energy spectra, energy fluences, etc for dynamic MLC fields. Comparisons of calculated dose distributions with the results from film dosimetry show good agreement for all the cases investigated in this study. The capability to calculate portal dose distributions is important in terms of IMRT pretreatment and treatment verification. These distributions can also be used as reference images for EPIDs. Furthermore, the MSM enables the calculation of energy fluence maps, which in turn allows the comparison with fluence maps used in IMRT treatment planning systems (Chetty *et al* 2000, Deng *et al* 2000, Laub *et al* 2001). Other potential uses are the calibration of EPIDs for portal dose imaging and benchmarking of treatment planning systems. In summary, the MSM supplemented with the dynamic MLC is a very flexible tool to examine in detail a variety of dosimetric matters in radiotherapy.

References

Andreo P 1991 Monte Carlo technique in medical physics *Med. Phys.* **36** 861-920

Arnfield M, Siebers J, Kim J, Wu Q, Keall P and Mohan R 2000 A method for determining multileaf collimator transmission and scatter for dynamic intensity modulated radiotherapy *Med. Phys.* **27** 2231-41

Catala A, Francois P, Bonnet J and Scouarnec C 1995 Reconstruction of 12 MV bremsstrahlung spectra from measured transmission data by direct resolution of the numeric system AF=T *Med. Phys.* **22** 3-10

CERN Application Software Group Computing and Network Division 1995 GEANT – Detector description and simulation tool *CERN Program Library Long Writeup* W5013 Genf

Chetty I, DeMarco J and Solberg T 2000 A virtual source model for Monte Carlo modeling of arbitrary intensity distributions *Med. Phys.* **27** 166-72

Deng J, Jiang S B, Kapur A, Li J, Pawlicki T and Ma C M 2000a Photon beam characterization and modelling for Monte Carlo treatment planning *Phys. Med. Biol.* **45** 411-27

Deng J, Pawlicki T, Chen Y, Li J, Jiang S and Ma C 2000b The MLC tongue-and-groove effect on IMRT dose distributions *Med. Phys.* **27**

——2000 *World Conf. (Chicago, 2000)* 1418

DeMarco J J, Solberg T D and Smathers J B 1997 A CT-based Monte Carlo simulation tool for dosimetry planning and analysis *Med. Phys.* **25** 1-11

Faddegon B A, O'Brien P and Mason D L D 1999 The flatness of Siemens linear accelerator x-ray fields *Med. Phys.* **26** 220-8

Fix M K, Keller H, Born E J and Rüegsegger P 2000 Simple beam models for Monte Carlo photon dose calculations in radiotherapy *Med. Phys.* **27** 2739-47

Fix M K, Manser P, Born E J, Vetterli D, Mini R and Rüegsegger P 2001a Monte Carlo simulation of a dynamic MLC: implementation and application *Z. Med. Phys.* **11** 163-70

Fix M K, Stampanoni M, Manser P, Born E J, Mini R and Rüegsegger P 2001b A multiple source model for 6 MV photon beam dose calculations using Monte Carlo *Phys. Med. Biol.* **46** 1407-27

Francois P, Catala A and Scouarnec C 1993 Simulation of x-ray spectral reconstruction from transmission data by direct resolution of the numeric system AF=T *Med. Phys.* **20** 1695-1703

Fogg R, Chetty I, DeMarco J, Agazaryn N and Solberg T 2000 Development and modification of a virtual source model for Monte Carlo based IMRT verification *Med. Phys.* **27**

——2000 *World Conf. (Chicago, 2000)* 1410

Hartmann Siantar C L, Bergstrom P M, Chandler W P, Chase L, Cox L J, Daly T P, Garrett D, Hornstein S M, House R K, Moses E I, Patterson R W, Rathkopf J A and Schach A 1997 Lawrence Livermore National Laboratory's PEREGRINE Project *Proc. 12th ICCR (Salt Lake City, USA)* (Madison, WI: Medical Physics Publishing) pp19-22

Jaffray D A, Battista J J, Fenster A and Munro P 1990 X-ray scatter in megavoltage transmission radiography: physical characteristics and influence on image quality *Med. Phys.* **21**, 45-60

Jiang S B and Ayyangar K M 1998 On compensator design for photon beam intensity-modulated conformal therapy *Med. Phys.* **25** 668-75

Li J S, Pawlicki T, Deng J, Jiang S B, Mok E and Ma C M 2000 Validation of a Monte Carlo dose calculation tool for radiotherapy treatment planning *Phys. Med. Biol.* **45** 2969-85

Liu H H, Mackie T R and McCullough E C 1997 A dual source photon beam model used in convolution/superposition dose calculations for clinical megavoltage x-ray beams *Med. Phys.* **24** 1960-74

LoSasso T, Chui C and Ling C 1998 Physical and dosimetric aspects of a multileaf collimation system used in the dynamic mode for implementing intensity modulated radiotherapy *Med. Phys.* **25** 1919-27

Lovelock D M J, Chui C S and Mohan R 1995 A Monte Carlo model of photon beams used in radiation therapy *Med. Phys.* **22** 1387-94

Ma C M and Rogers D W O 1995 Beam characterization: a multiple-source model *National Research Council of Canada Report* PIRS 0509C (NCR, Ottawa)

Ma C M, Mok E, Kapur A, Brain S, Findley D and Boyer A 1998 Clinical implementation of a Monte Carlo treatment planning system *Med. Phys.* **25** A128

Ma C-M, Mok E, Kapur A, Pawlicki T, Findley D, Brain S, Forster K and Boyer A L 1999 Clinical implementation of a Monte Carlo treatment planning system *Med. Phys.* **26** 2133-43

Mohan R 1997 Why Monte Carlo? *12th Int. Conf. on the Use of Computers in Radiation Therapy (Salt Lake City, Utah, May 1997)*

Rogers D W O and Bielajew A F 1990 Monte Carlo techniques of electron and photon transport for radiation dosimetry *The Dosimetry of Ionizing Radiation* vol 3 ed K R Kase, B E Bjärngard and F H Attix (San Diego, CA: Academic Press) pp 427-539

Rogers D W O, Faddegon B A, Ding G X, Ma C M and We J 1995 BEAM: a Monte Carlo code to simulate radiotherapy treatment units *Med. Phys.* **22** 503-25

Schach von Wittenau A E, Cox L J, Bergstrom P M, Chandler W P, Siantar C L and Mohan R 1999 Correlated histogram representation of Monte Carlo derived medical accelerator photon-output phase space *Med. Phys.* **26** 1196-211

Shih R 2000 Monte Carlo simulation of dynamic wedged fields *Med. Phys.* **27** 2827

Shih R, Li X A and Chu J C H 2001 Dynamic wedge versus physical wedge: a Monte Carlo study *Med. Phys.* **28** 612-19

Siebers J V, Keall P J, Arnfield M, Kim J O and Mohan R 2000 Dynamic-MLC modeling for Monte Carlo dose calculations *13th Conf. of Use in Computers in Radiation Therapy (Heidelberg, May 2000)* ed W Schlegel and T Bortfeld pp 455-7

Sjögren R and Karlsson M 1996 Electron contamination in clinical high energy photon beams *Med. Phys.* **23** 1873-81

Stampanoni M, Fix M K, Francois P and Rüegsegger P 2001 Computer algebra for x-ray spectral reconstruction between 6 and 25 MV *Med. Phys.* **28** 325-7

van der Zee W and Welleweerd J 1999 Calculating photon beam characteristics with Monte Carlo techniques *Med. Phys.* **26** 1883-92

Verhaegen F and Das I J 1999 Monte Carlo modelling of a virtual wedge *Phys. Med. Biol.* **44** N251-59

Verhaegen F and Liu H H 2001 Incorporating dynamic collimator motion in Monte Carlo simulations: an application in modelling a dynamic wedge *Phys. Med. Biol.* **46** 287-96

Wang X, Spirou S, LoSasso T, Stein J, Chui C and Mohan R 1996 Dosimetric verification of intensity modulated fields *Med. Phys.* **23** 317-27

Zhu T C and Palta J-R 1998 Electron contamination in 8 and 18 MV photon beams *Med. Phys.* **25** 12-19

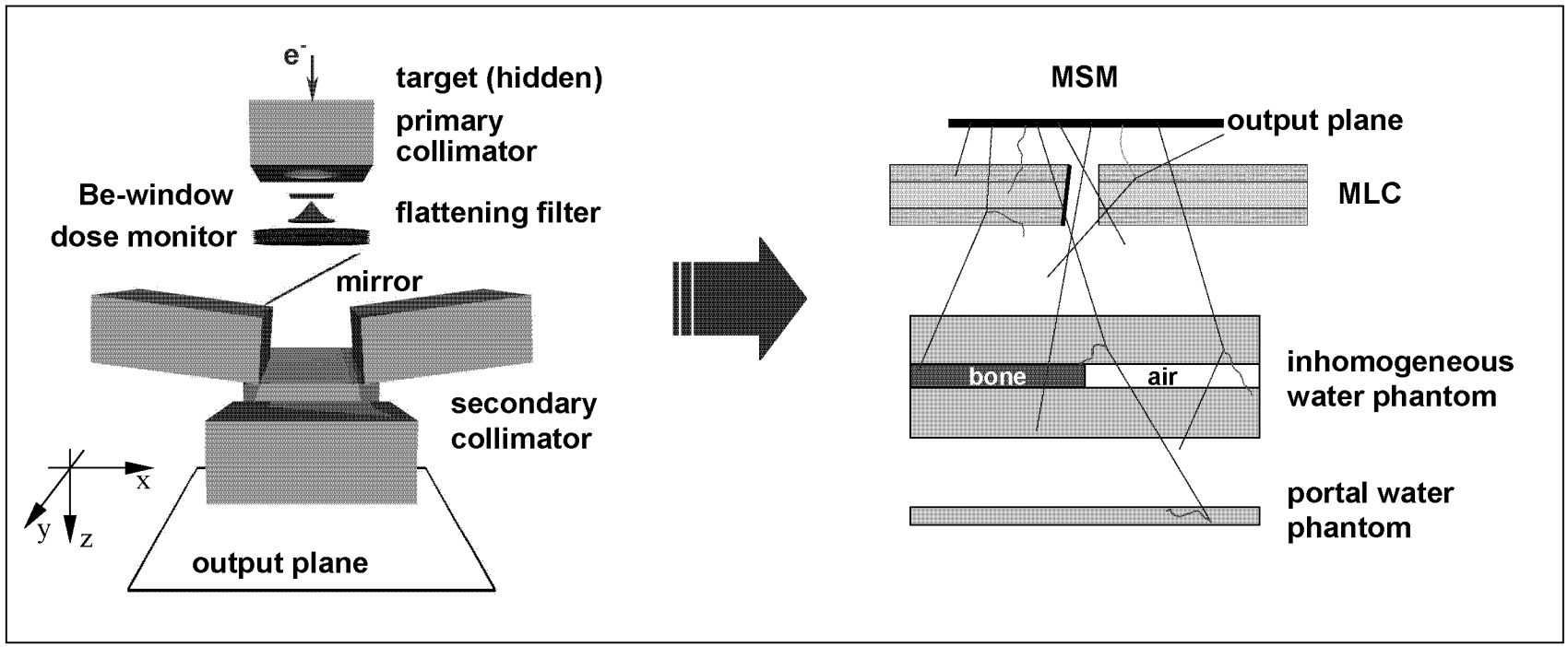

FIG. 1. Geometry of the accelerator head implemented in the MC code GEANT to generate the phase space data (left). A monoenergetic circular electron parallel beam hits the target at the central axis. Below the two pairs of secondary collimator jaws, the output plane is located perpendicularly to the central axis and used as scoring plane for the phase space files. The MSM defines the particles' starting parameters in the output plane (right) downstream to the MLC and the phantom configuration.

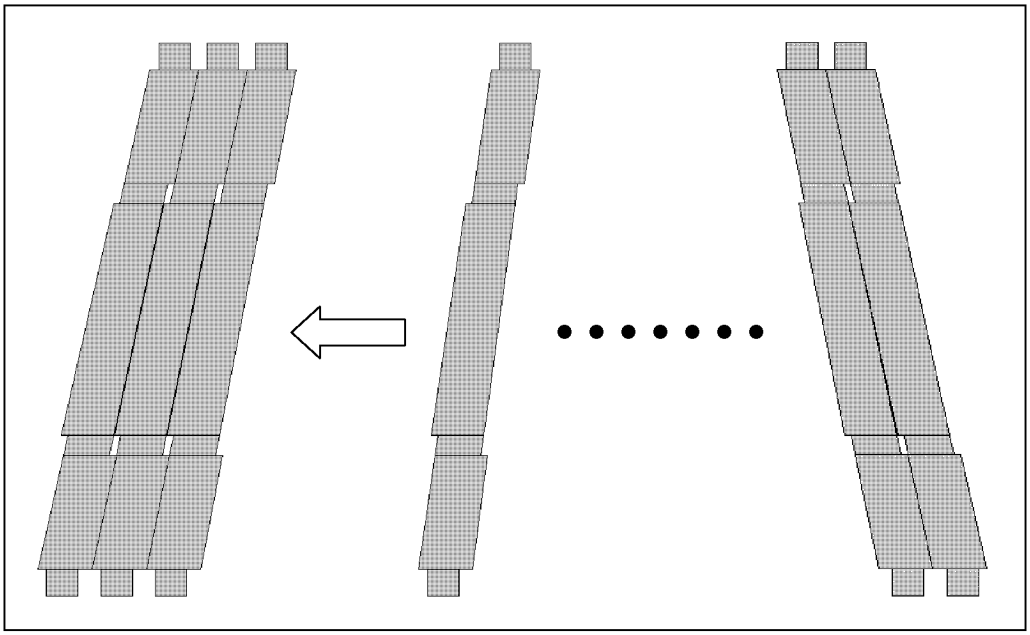

FIG. 2. Cross section of the MLC modelled for the MC simulations. The tongue and groove of the leaves were fully modelled.

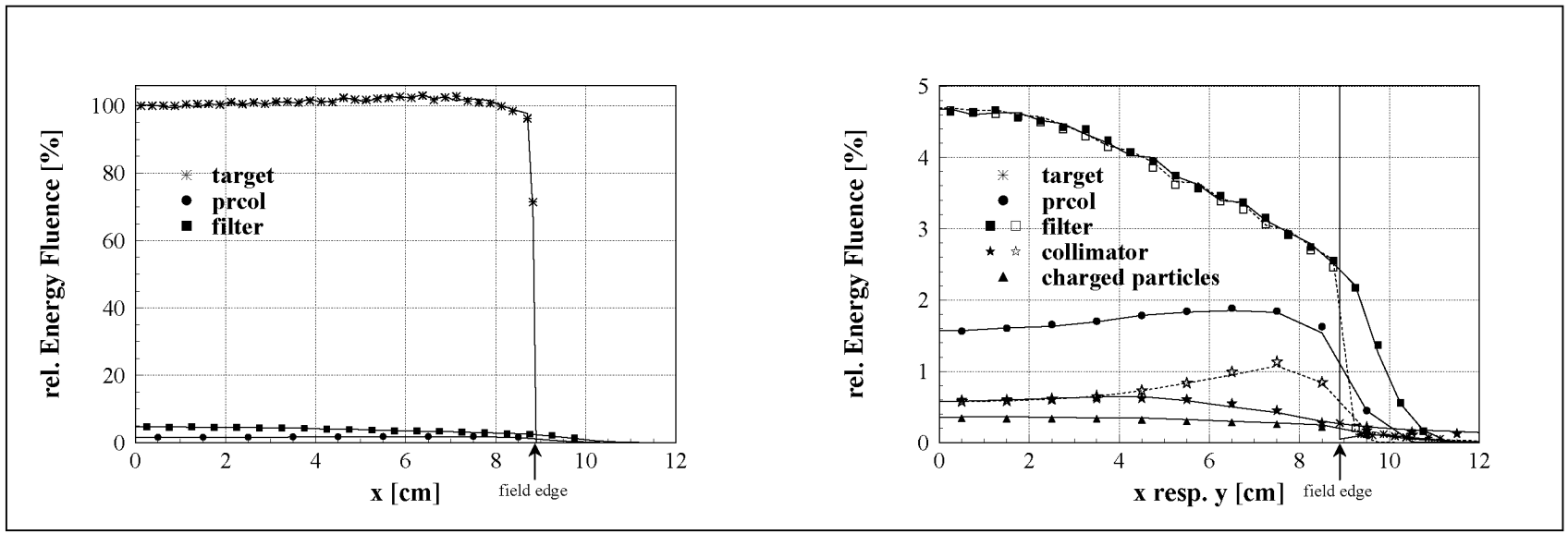

FIG. 3. Energy fluence distributions in the output plane for the 40 x 40 cm^2 field of the MSM (curves) and the original PS data (symbols). The right-hand side gives some more details of the scatter components. The full curves together with the full symbols represent the distribution of energy fluence along the *x*-axis, the broken curves and the open symbols that along the *y*-axis. (prcol = primary collimator.)

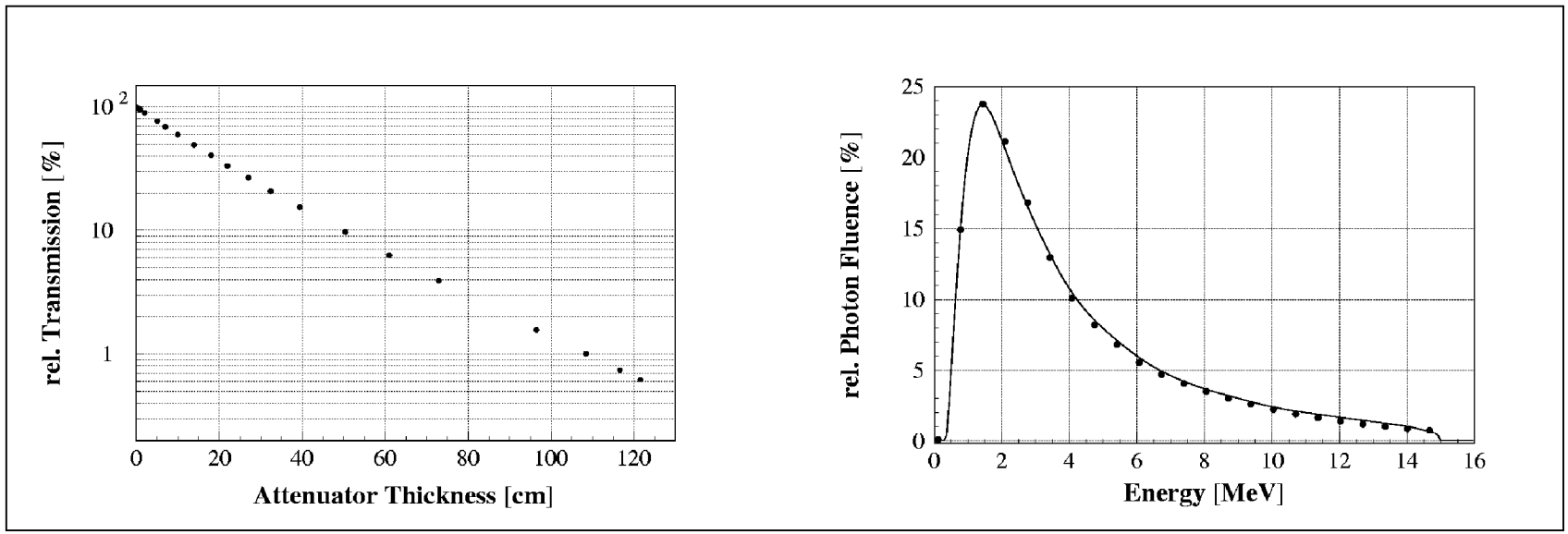

FIG. 4. Transmission curve (left) and reconstructed energy spectrum (right) of a 15 MV photon beam using an empirical numerical method introduced by Francois *et al* (1993). Carbon was used for the attenuator material. The full curve is the MC-calculated target spectrum whereas the dots result from the reconstruction of the transmission curve. The error bars for the measurements are smaller than the symbols.

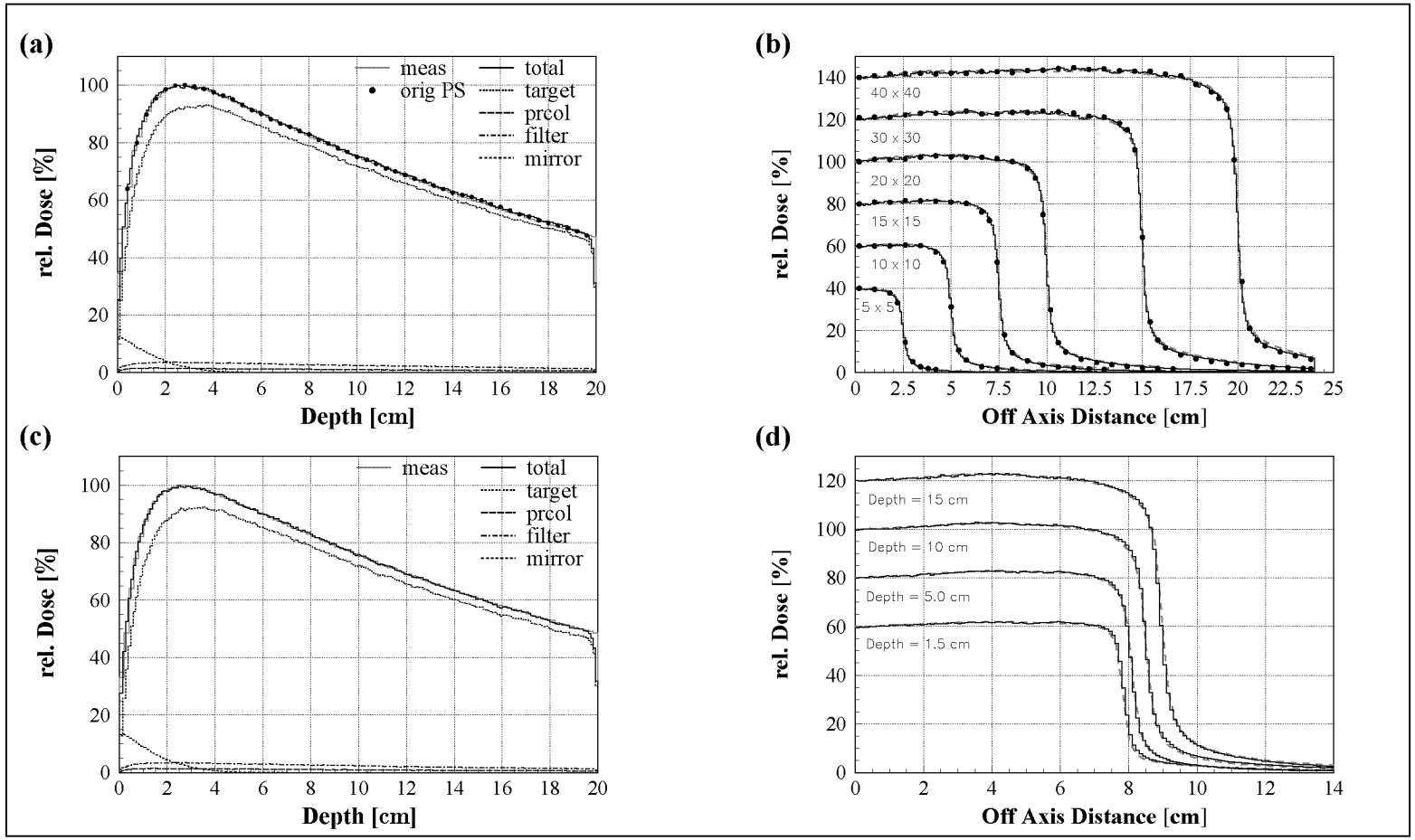

FIG. 5. Calculated depth dose curves for a 10 x 10 cm^2 (a) and 9 x 17 cm^2 (c) field and dose profiles for several field sizes at a water depth of 10 cm (b) and for several depths for a 9 x 17 cm^2 (d) field together with the corresponding measurements for a 15 MV photon beam. The dots represent the dose calculations using the original PS data in (a) and (b). The statistical uncertainty of the MC dose calculations around the maximum is less than 1%. For readability, the profiles are normalized to different central axis values.

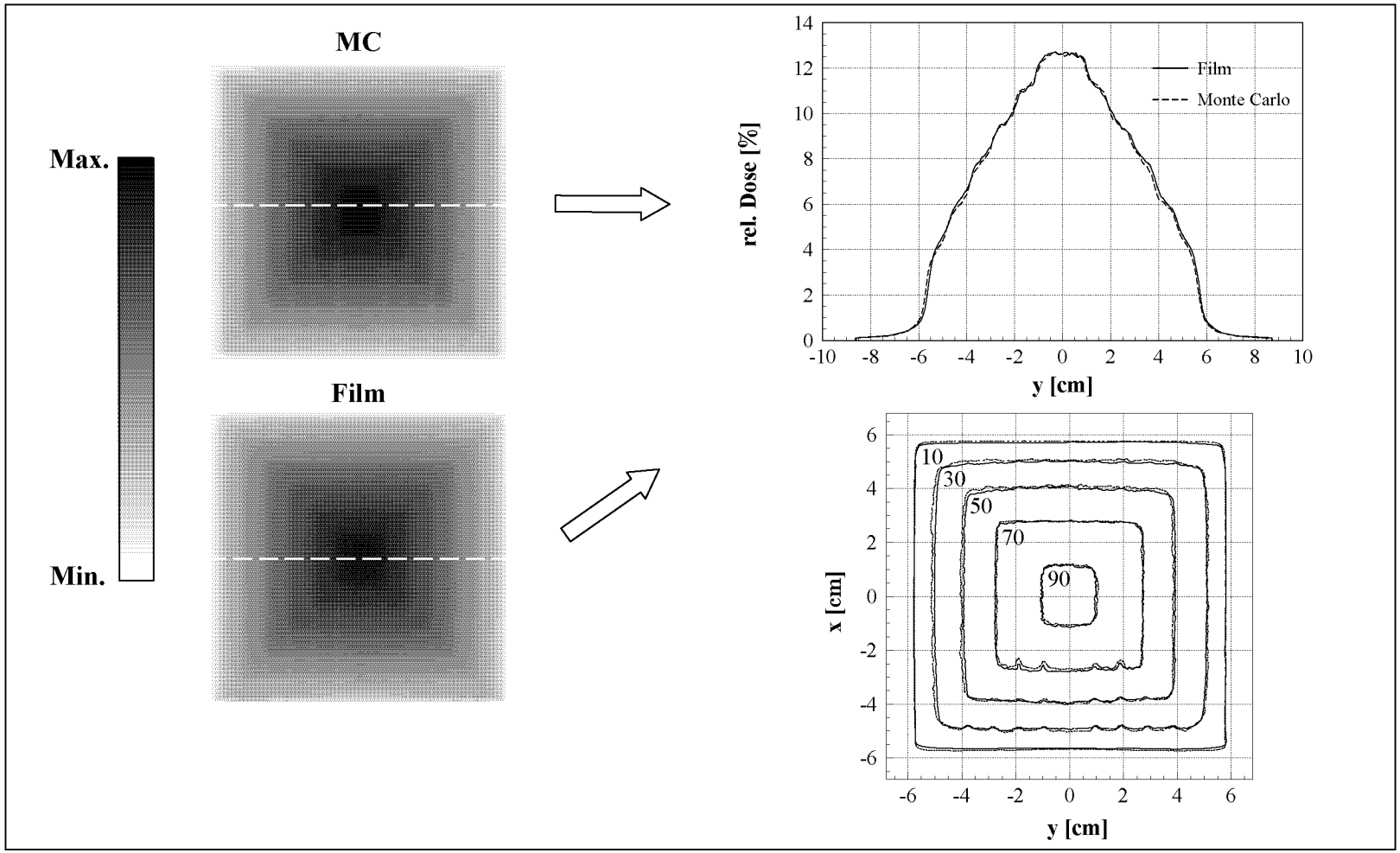

FIG. 6. The dose distributions at a water depth of 5 cm of the MC calculation (left top) and film measurement (left bottom) together with a comparison of a profile (right top) along the *y*-direction as indicated by the broken curves for the step and shoot case. The area under each profile is normalized to 100%cm. In addition, isodose plots (right bottom) of the MC calculation (broken curves) and the film measurement (full curves) are depicted for comparison.

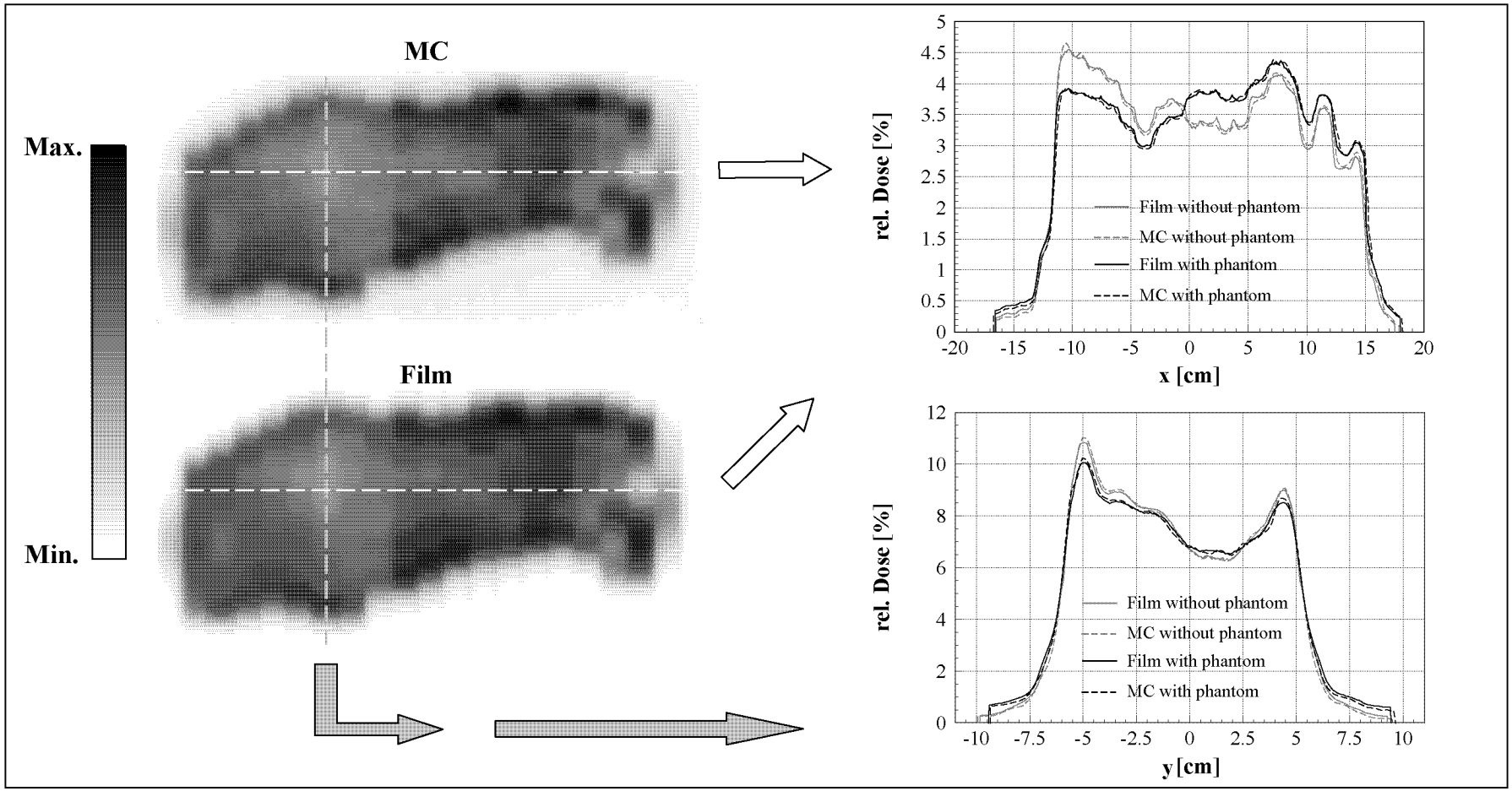

FIG. 7. The portal dose distributions at a water depth of 5 cm of the MC calculation (left top) and film measurement (left bottom) together with a comparison of profiles (right) along the *x*- and *y*-direction, respectively, as indicated by the broken lines for the bronchus case, where the inhomogeneous phantom was in the beam. In addition, the portal dose profiles calculated without phantom in the beam are depicted for comparison. The area under each profile is normalized to 100%cm.

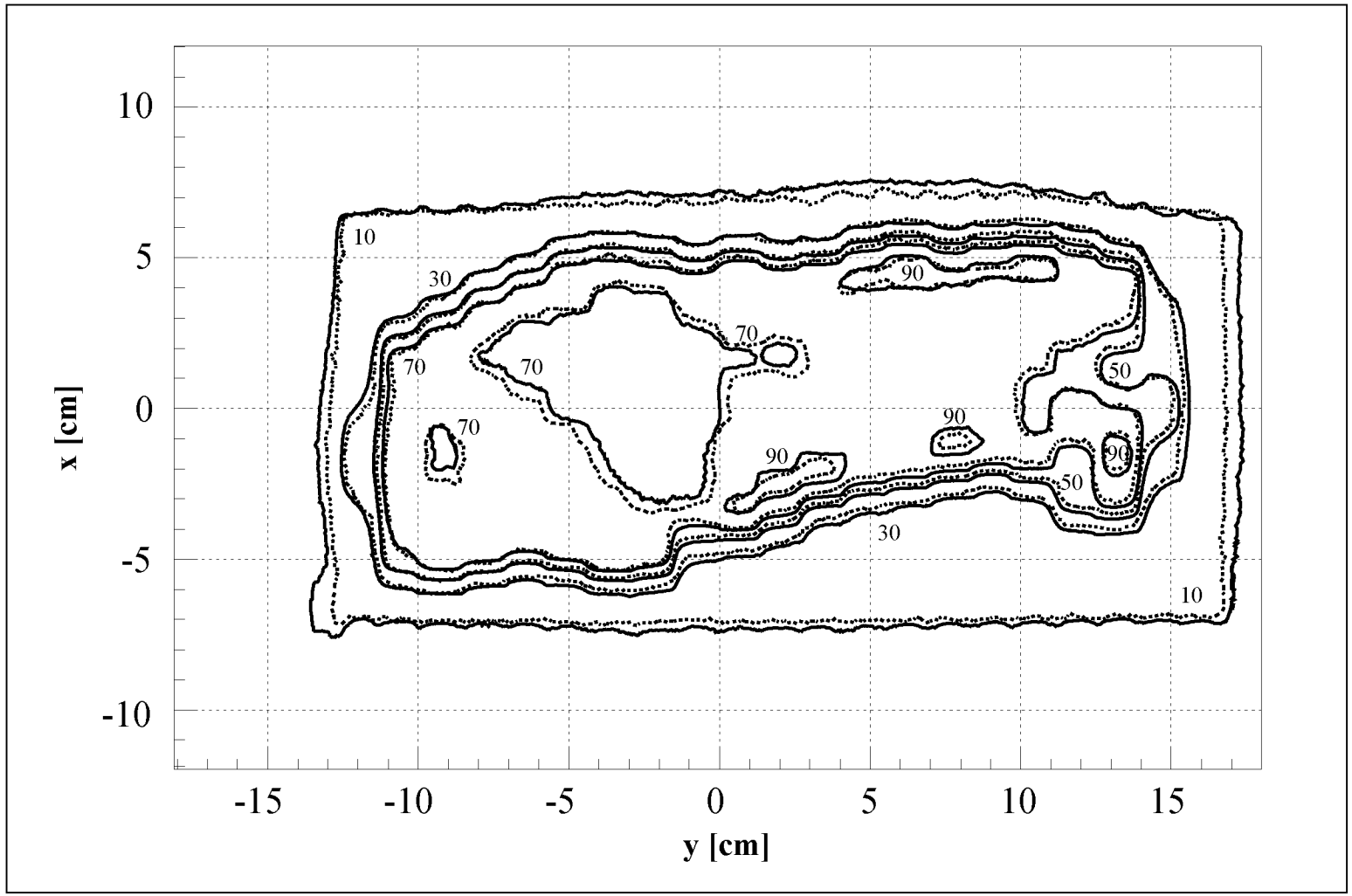

FIG. 8. Isodose plots for the bronchus case (see figure 7) of the MC calculation (broken curves) and of the film measurement (full curves) are depicted for comparison.

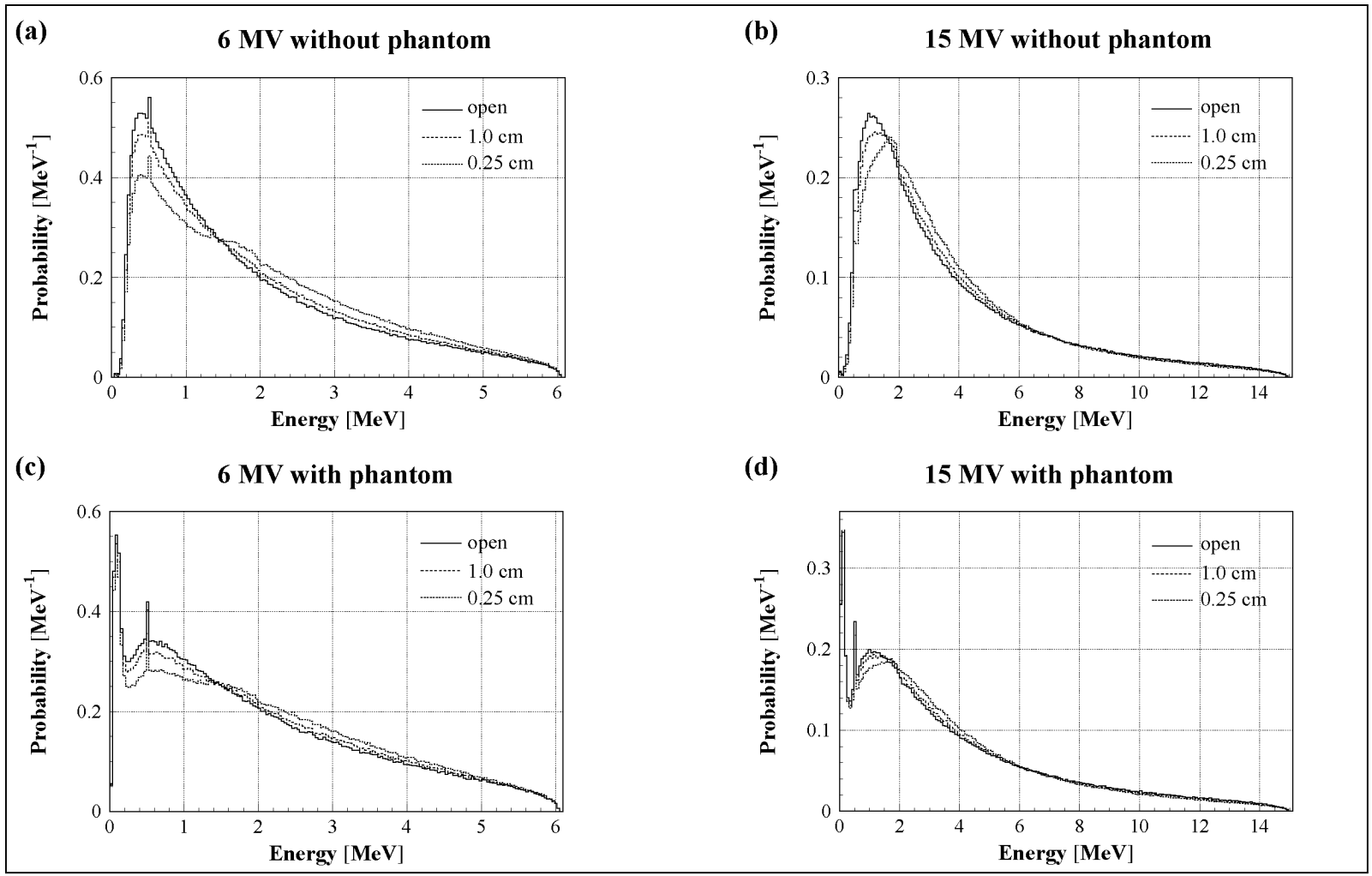

FIG. 9. Energy spectra for the 6 and 15 MV beam without phantom in the beam (a) and (b), respectively, and together with a phantom in the beam (c) and (d), respectively, for the open beam and for the slits with a width of 1.0 and 0.25 cm. The statistical uncertainty around the maximum is about 1%. The area under each curve is normalized to 1.

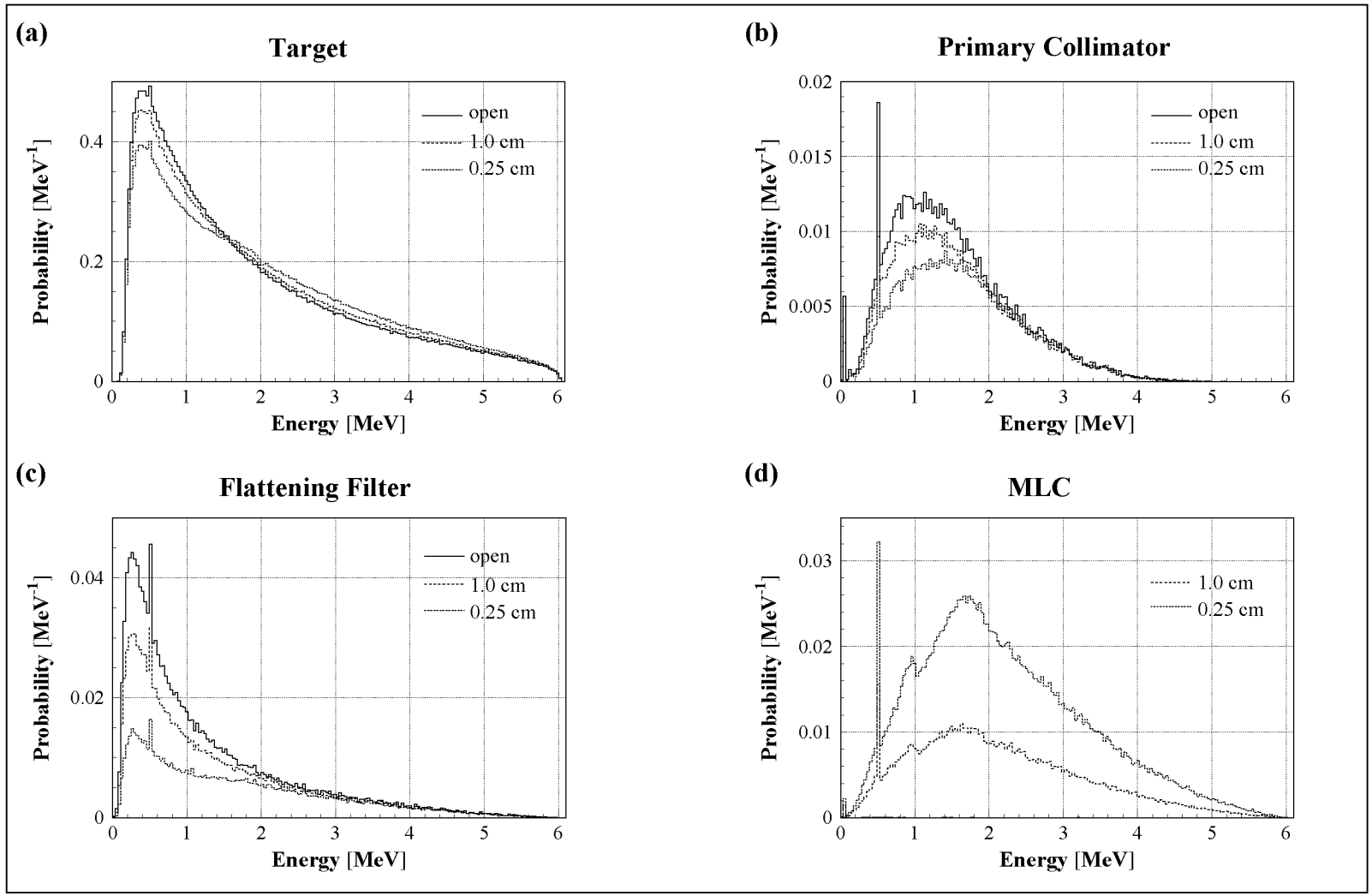

FIG. 10. The contribution of the main scatter components to the total energy spectra of the 6 MV beam (figure 8(a)) without phantom in the beam: target (a), primary collimator (b), flattening filter (c) and MLC (d) for the open beam and for the slits with a width of 1.0 and 0.25 cm. The statistical uncertainty around the maximum is about 1% for (a) and (c), about 3% for (d) and 4% for (b).

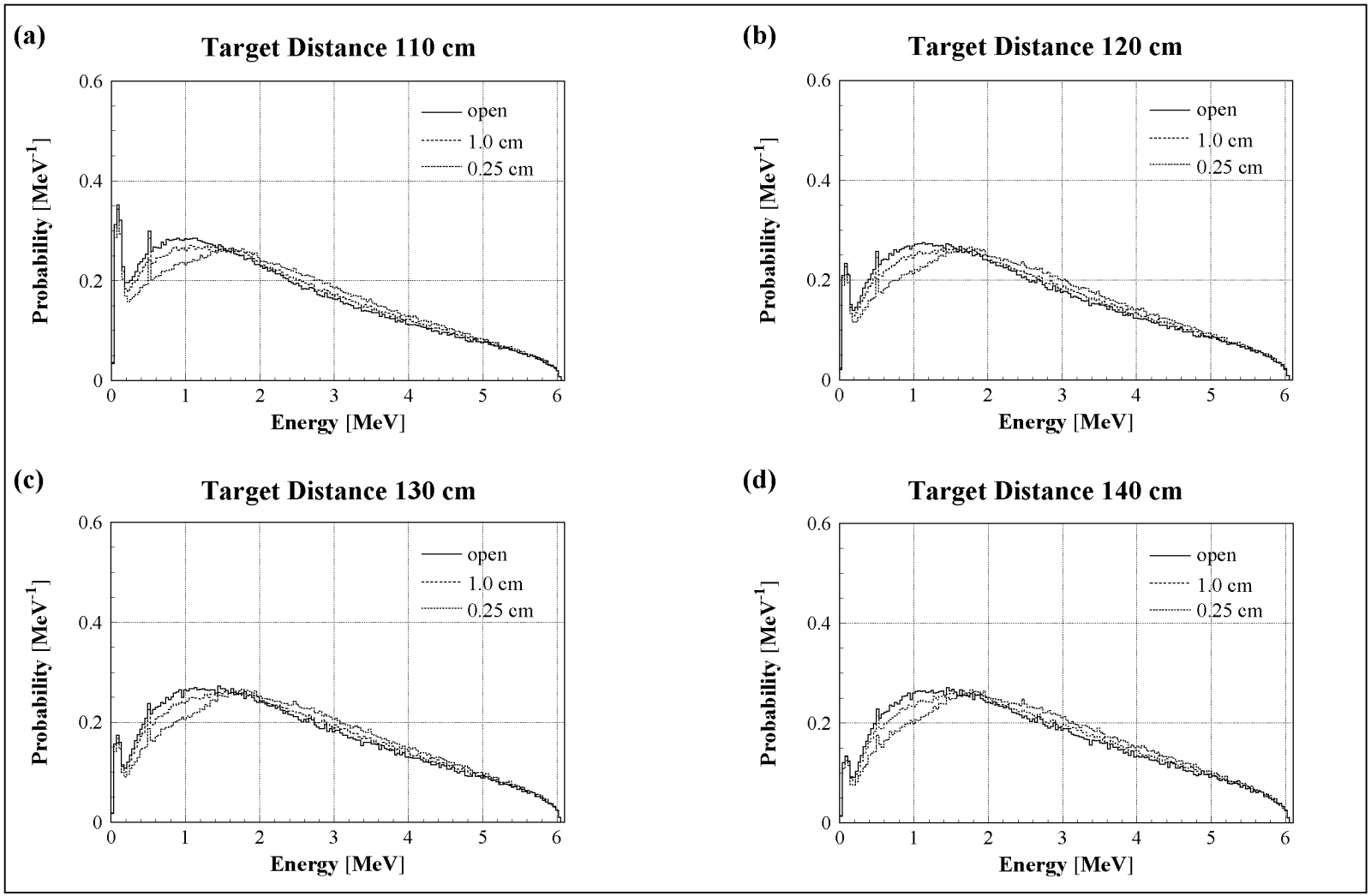

FIG. 11. Energy spectra for the 6 MV beam with phantom in the beam for the portal planes with a distance of 110 cm (a), 120 cm (b), 130 cm (c) and 140 cm (d) from the target for the open beam and for the slits with a width of 1.0 and 0.25 cm. The statistical uncertainty around the maximum is about 1.5%. The area under each curve is normalized to 1.

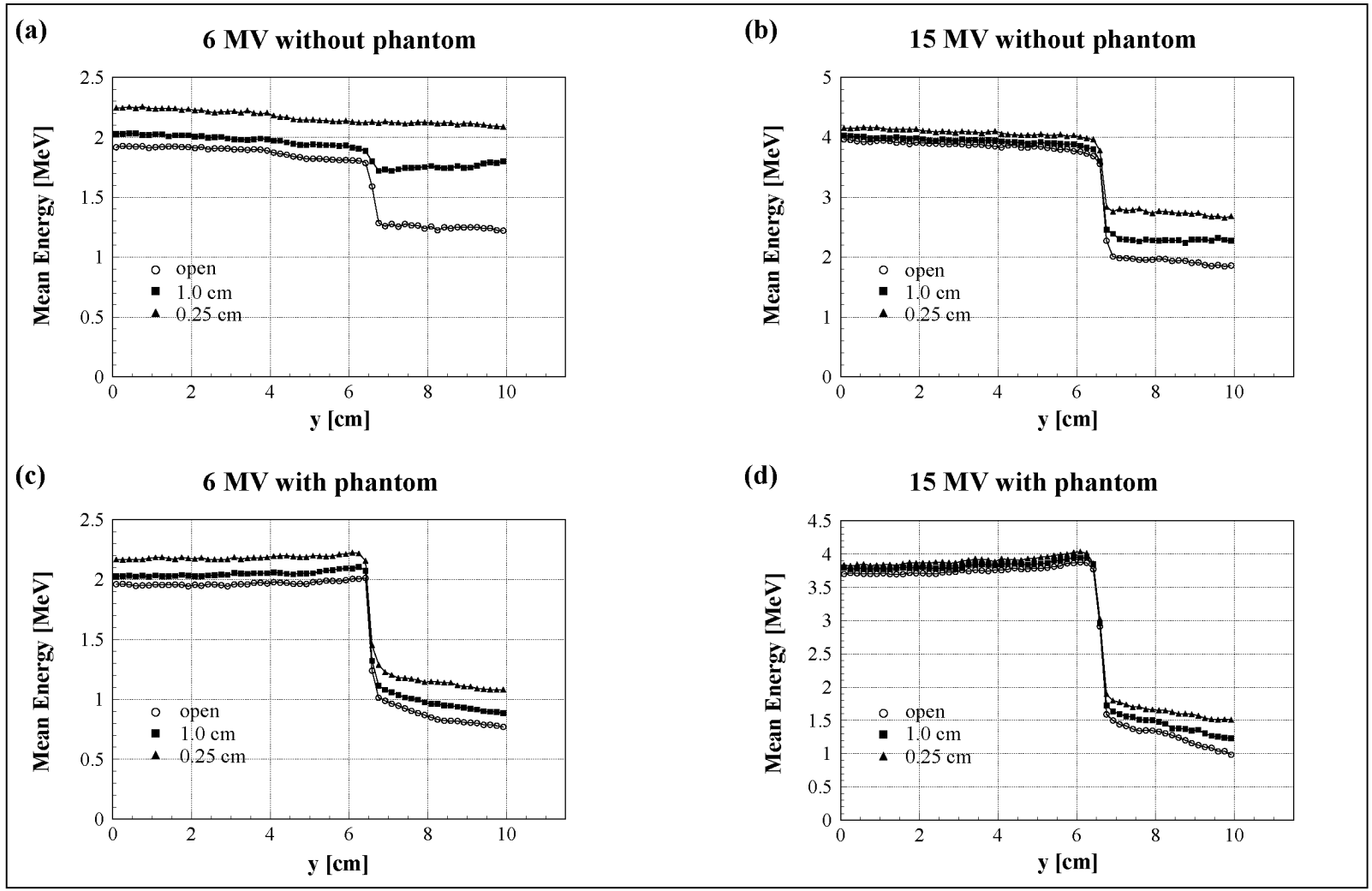

FIG. 12. Mean energy along the *y*-direction for the 6 and 15 MV beam without phantom in the beam (a) and (b), respectively, and together with a phantom in the beam (c) and (d), respectively, for the open beam and for the slits with a width of 1.0 and 0.25 cm. The statistical uncertainty is about 1%.

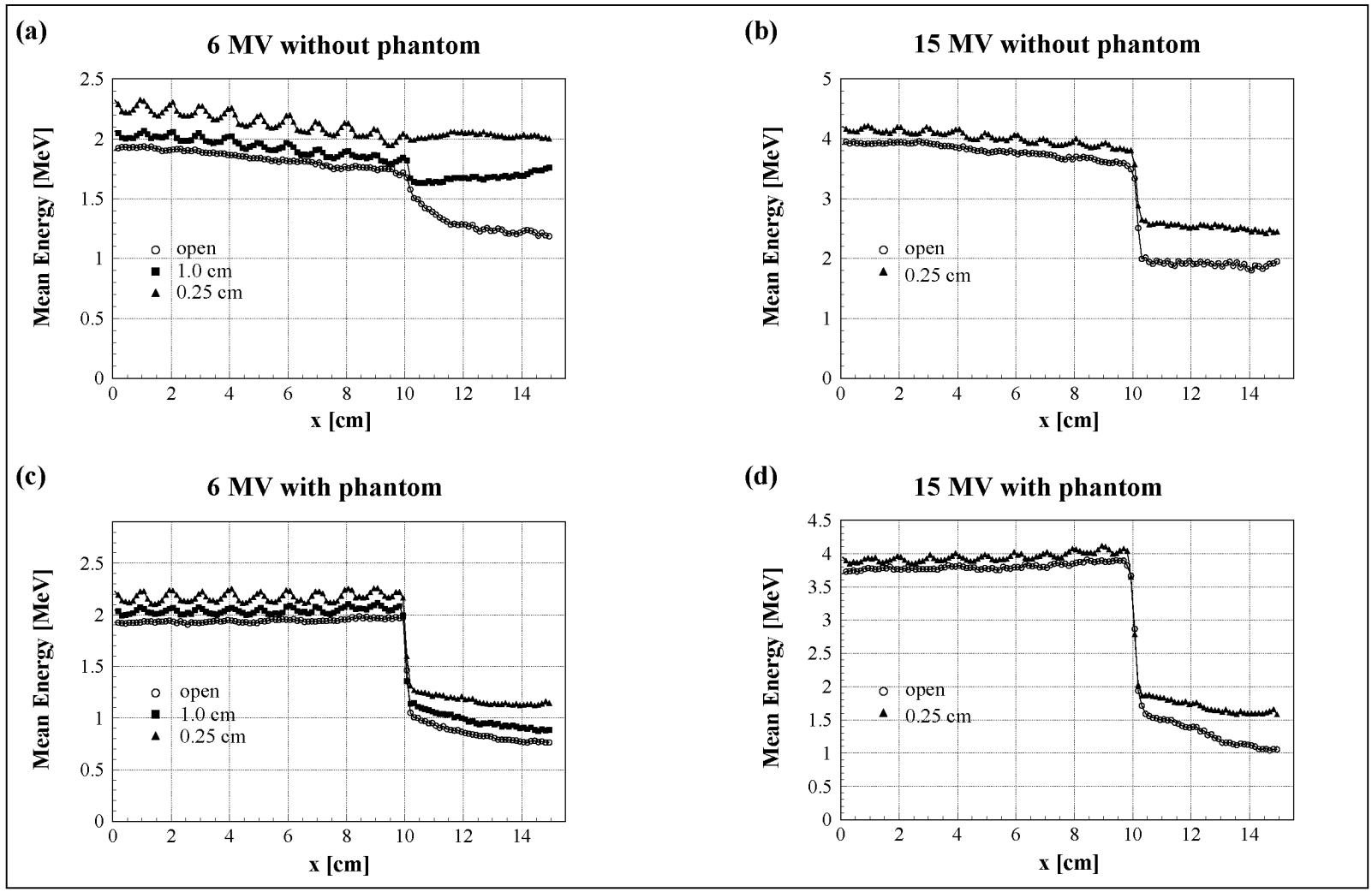

FIG. 13. Mean energy along the *x*-direction for the 6 and 15 MV beam without phantom in the beam (a) and ((b), respectively, and together with a phantom in the beam (c) and (d), respectively. The statistical uncertainty is about 1%.

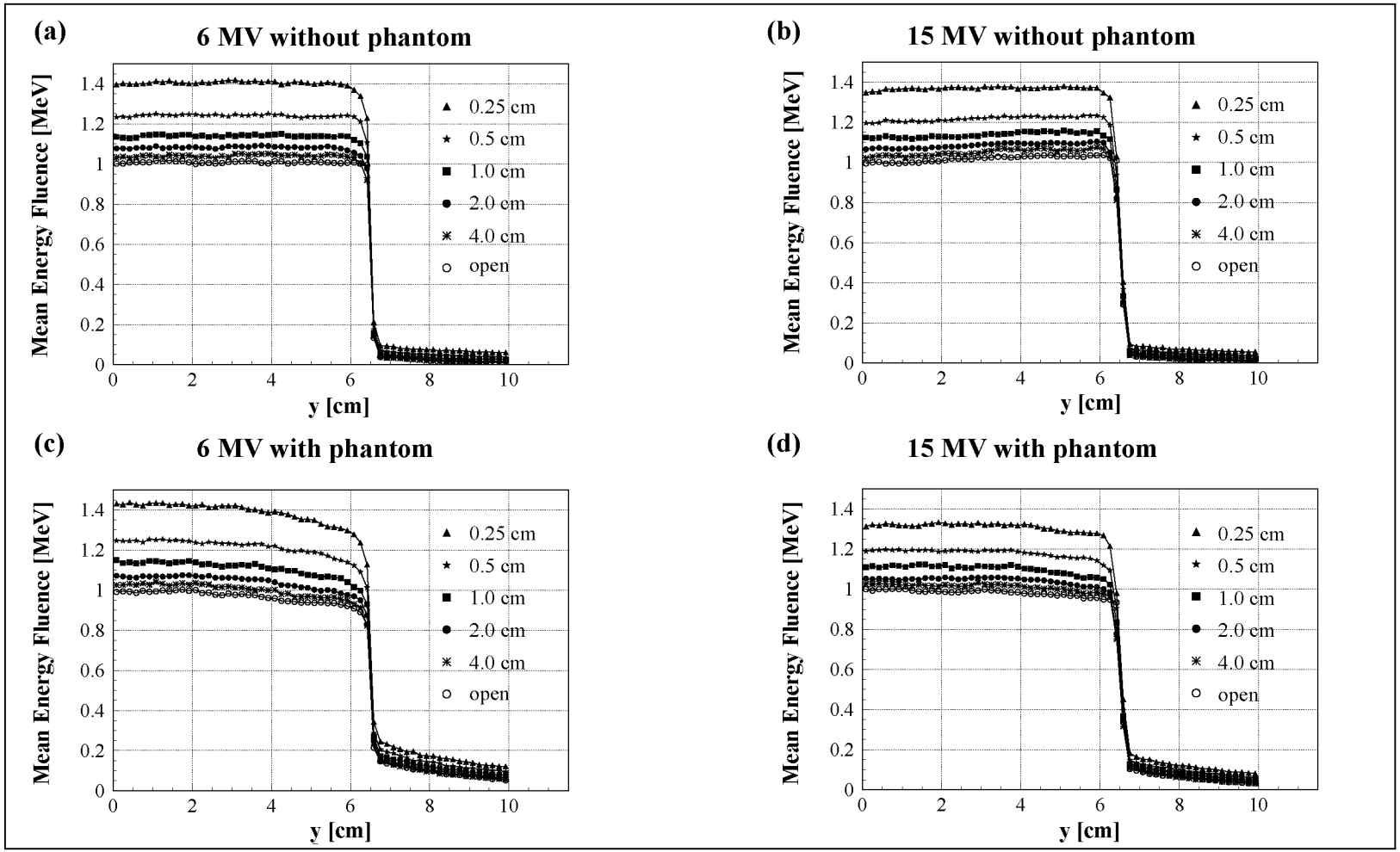

FIG. 14. Mean energy fluence along the *y*-direction for the 6 and 15 MV beam without phantom in the beam (a) and (b), respectively, and together with a phantom in the beam (c) and (d), respectively. The statistical uncertainty is about 1%. The curves are normalized to the mean energy fluence of the open field, which was set equal to 1 on the central axis.

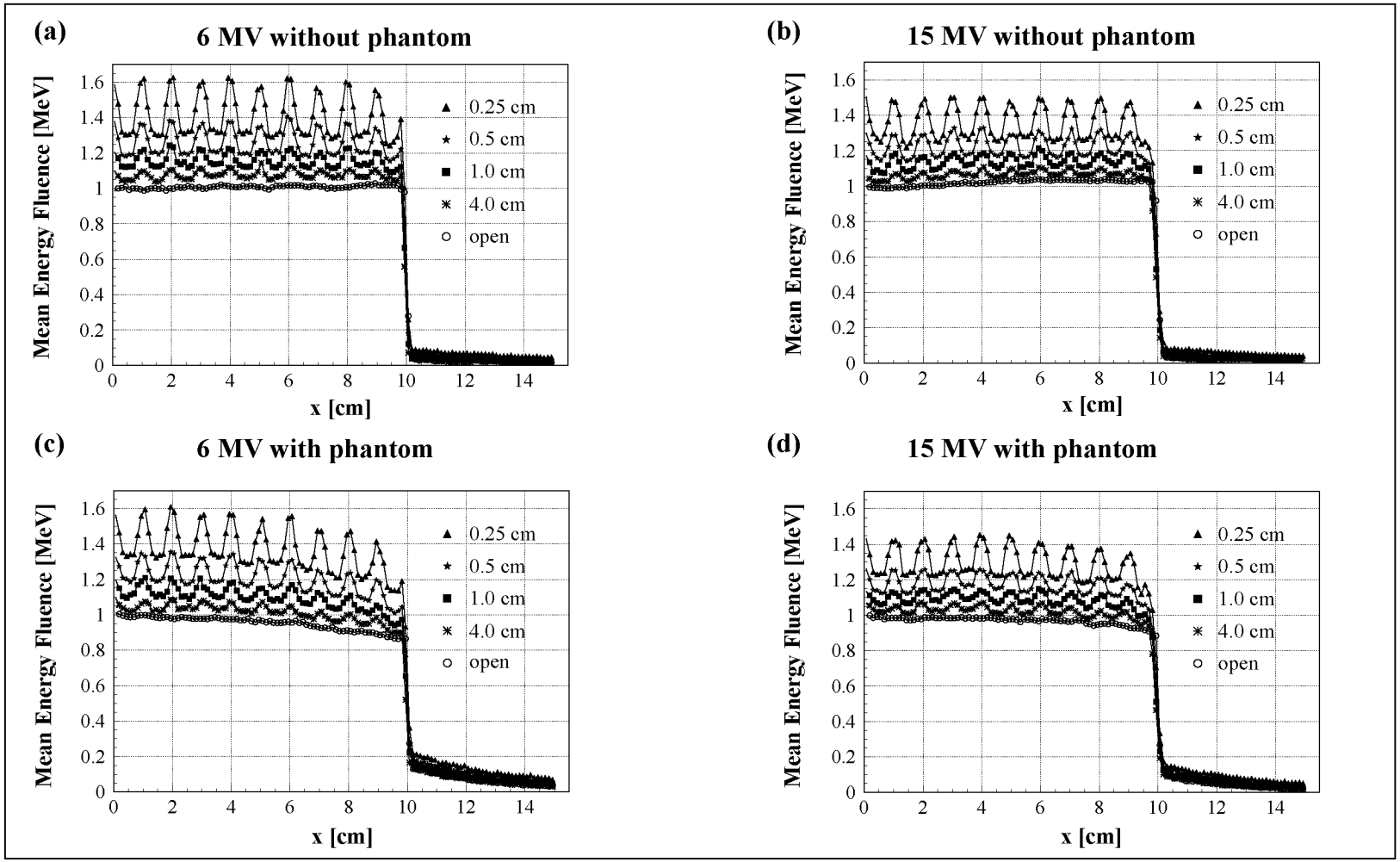

FIG. 15. Mean energy fluence along the *x*-direction for the 6 and 15 MV beam without phantom in the beam (a) and (b), respectively, and together with a phantom in the beam (c) and (d), respectively. The statistical uncertainty is about 1%. The curves are normalized to the mean energy fluence of the open field, which was set equal to 1 on the central axis.

7

Discussion

In the following sections certain aspects of accuracy and precision of the MC simulations and the measurements made in this work are discussed.

7.1. MC simulations

The MC method uses probability distributions of interactions of electrons and photons with matter to simulate random trajectories of individual particles. The accuracy of the MC results depends on the quality of the cross sections used. A recently published review of compilations of mass attenuation coefficient data for photons assigns 1-2% uncertainty in the energy range between 5 keV and 10 MeV (Hubbell 1999). As described in the ICRU Report No. 37 (1984), the uncertainty in the electron and positron collision stopping power between 10 and 100 keV is estimated to be 2-3% for low-Z materials and 5-10% for high-Z materials. Above 100 keV, the uncertainty is estimated to be within 1-2%. In addition, there are the uncertainties up to a few percent caused by the analytic components of the simulation (tabulations, fittings, etc.) reflecting inherent approximations.

Errors in the cross-section data aside, the random number generation as well as the cutoff energies cause errors in MC calculations. However, great effort has been made to develop random generators with a large period, for example the one in GEANT has a period of 2^{60} (CERN 1995). On the other hand, the lowest energy cutoff of 10 keV possible in GEANT is low enough for dose calculations, since the range of these low-energy particles is small compared with the geometries of interest. Thus, these errors do not virtually contribute to the overall uncertainty of the final result for dose calculations in radiotherapy.

Other sources of uncertainties are the error made by implementing ideal materials and geometries, the programming errors and roundoff and truncation errors as discussed in Rogers and Bielajew (1990).

The overall uncertainty resulting in the final calculation is very hard to determine. As an extreme example, a 50% error in the electron stopping power below 2 MeV would have virtually no effect on a calculated depth dose curve for 10 MeV photons because these electrons have a short range and deposit all of their energy locally (Rogers and Bielajew 1990). These systematic errors are almost cancelled out considering ratios or relative quantities as throughout this thesis. In addition the relatively high uncertainties for the cross section data of charged particles are less important when dealing with photon beams, since the mean free pathlength of the photons is large in comparison with the geometries of interest throughout this thesis.

Besides these systematic errors, results from MC calculations are of virtually no use unless some estimate of their statistical uncertainty is given. It is a common practice to separate the MC calculation into a number of independent batches N using the same number of histories (Rogers and Bielajew 1990). The final estimation of the quantity of interest X is the average of this quantity of each batch X_i. Assuming a normal distribution for the X_i, the best estimation of the variance of the mean S is:

$$S(X)^2 = \sum_{i=1}^{N} \frac{(X_i - X)^2}{N(N-1)}$$

In this thesis, all MC calculations were split into 10 batches and the statistical error was calculated using the equation above. In addition, in this work relative quantities in dose calculations are discussed and therefore the precision of the result, dealing with random uncertainties, is important.

7.2. Dose measurements

Throughout this thesis several dose measurements were performed using ionization chambers, diodes or films. The following sections discuss the accuracy and the precision of these dose measurements.

7.2.1. Ionization chamber

According to the AAPM protocol (AAPM TG-21 1983) the dose in a medium D_{med} can be determined from the dose measured in a gas D_{gas} using an ionization chamber:

$$D_{med} = D_{gas} \cdot \left(\frac{S}{\rho}\right)_{gas}^{med} \cdot P = M \cdot N_D \cdot \left(\frac{S}{\rho}\right)_{gas}^{med} \cdot P$$

where $(S/\rho)_{gas}^{med}$ is the stopping power ratio of the medium to that of the gas, P is a total perturbation correction factor, M is the reading from the electrometer in the ionization chamber set-up and N_D is the cavity-gas calibration factor. The total correction factor P accounts for the correction of the perturbation of the electron fluence around the reference point by the gas cavity and for differences in the material of the chamber wall and the medium. The factor N_D is directly related to the chamber calibration made by a primary standards laboratory and takes the correction for the charge collection efficiency, differences in materials of the wall and the build-up cap, the average energy required to produce an ion pair and some other corrections into account (SGSMP 1992). Usually air is used in the gas cavity of the ionization chamber and water is the preferred medium in phantoms.

The overall uncertainty in the dose determination at the reference depth in a water phantom is composed of several numbers of systematic uncertainties inherent to the protocol and random uncertainties attached to the measurement procedure. In table 1 estimations of these uncertainties are summarized (Lillicrap *et al* 1983,SGSMP 1992).

Since ratios and relative dose comparisons were made in this thesis using the same linear accelerator, the uncertainties and therefore the precision in the dose measurements is reduced to the last four random uncertainties listed in table 1 and can be estimated to be about 0.5%.

The estimation of an uncertainty of 0.5% can also be used for the ionization chamber measurements carried out to perform the transmission curve.

Uncertainty	Type	Value
primary exposure standard	systematic	1.5%
calibration factor N_D	systematic	1.9%
correction factor P	systematic	1%
stopping power ratio	systematic	1.5%
total systematic uncertainties		3.0%
secondary standard calibration	systematic/random	0.6%
calibration of the field instrument	systematic/random	1%
charge measurement	random	0.2%
ion recombination	random	0.2%
temperature measurement	random	0.3%
depth of measurement	random	0.3%
total random uncertainties		1.3%
total uncertainties		3.3%

Table 1 *Summary of the uncertainties in the dose determination at the reference depth in water using a ionization chamber.*

7.2.2. P-type diodes

Normally ionization chambers are used for dose determination in photon radiotherapy. However, for relatively small fields (up to a field size of 20 x 20 cm^2) and relative dosimetry the use of diodes instead of ionization chambers is preferable, because diodes show a high sensitivity to radiation, possess a good mechanical stability, are of small size and need no external voltage. The sensitivity per unit volume of a diode is about 18000 times higher than for an air-filled ionization chamber (Essers and Mijnheer 1999) and the small size results in higher spatial resolution, which is especially important in the build-up and the penumbra region, and in less perturbation of the radiation field. For greater field sizes, diodes overestimate the dose, because of the increasing amount of low-energy scattered photons in the radiation field and the preferential response of the diode to low-energy photons. Furthermore, the dependence of

the diode response on accumulated dose, dose rate and temperature has to be taken into account. For example, a decrease in dose response of about 0.1% per 100 Gy has been observed for p-type diodes (Lanson *et al* 1999). The dependence of diode sensitivity on dose rate and temperature has been investigated by Grusell *et al* 1986 and van Dam *et al* 1990. A sensitivity increase with temperature of about 0.1% per °C was found by Grusell *et al* (1986) for p-type silicon detectors increasing to about 0.3% per °C after a pre-irradiation of 5 kGy without any increase for further pre-irradiation. van Dam *et al* (1990) confirmed these results. In addition, they reported an increase in dose response between 1 and 11% when dose rate changes from 0.06 Gy/min to 3.9 Gy/min.

The diodes are usually calibrated against an ionization chamber measurement at a reference point. Calibration factors have to be corrected for the dependence of the diode response on accumulated dose, dose rate and temperature. However, for relative dose measurements in a homogeneous phantom only the dependence of temperature is important and when the diode is positioned in a water phantom, this dependency is almost negligible, as the water reservoir acts as a thermal buffer and if frequent recalibrations are performed. Overall one can estimate about the same uncertainty of 0.5% for the dose determination with the diode as for the one using the ionization chamber, when dealing with relative dose measurements.

7.2.3. Photographic film

Due to its high spatial resolution, fast acquisition of fully two-dimensional images and easy set up, the photographic film is regarded as an attractive integrating dosimeter. Therefore, films are a useful alternative for measuring lateral dose distributions when dealing with intensity modulated fields. The main drawback of the photographic films arises from the fact that the silver-bromide grains in the film emulsion preferentially respond to photons with energies lower than about 400 keV. This is due to the large photoelectric absorption cross section of silver-bromide.

In order to obtain the dose distribution from an irradiated film, the film has first to be developed by a chemical processing. The radiation effect is then measured in terms of the optical density OD

$$OD = \log_{10}(\frac{I_0}{I_t})$$

where I_0 is the light intensity incident on the developed film and I_t is the light intensity transmitted through the film. The OD can be mathematically expressed as (Dixon and Ekstrand 1976, Attix 1986, Yeo *et al* 1999)

$$OD = \log(e) \cdot \sigma_d x n$$

where σ_d is the effective cross-sectional area of the developed grains in the emulsion, x is the emulsion thickness and n is the developed grain number density in the emulsion. n can be related to the dose the film has received by using the target-hit model (Dixon and Ekstrand 1976):

$$n(t) = N\left(1 - e^{\sigma\phi t}\right)$$

where N is the initial grain number density in the emulsion, t is the exposure time, σ is the cross section of interaction and ϕ is the fluence. Since $\sigma\phi t$ is proportional to dose, the OD is also a function of the total dose. Therefore, a calibration function between OD and dose is needed, which can be achieved by exposing films to known doses under calibration conditions. Since the developed films have to be scanned by a scanning device, another calibration curve is required to relate the output of the analog/digital converter (ADC) involved to the OD. This function is determined with reference films of known ODs. Furthermore, one has to take into account that the nonexposed film will already have a finite OD. This is due to some spontaneous reactions in the emulsion and background radiation, called *fog*, and a corresponding light absorption in the film base, called *base*. These background densities have always to be subtracted from the OD readings after film exposure.

One of the most critical aspects concerning the uncertainty in the dose determination using films is the variation of their sensitivity. In order to overcome this uncertainty the experiment and the corresponding film calibration was performed using films from the same batch. Table 2 contains the remaining uncertainties of the different steps in the dose determination according to a reference depth in water. The typical automated process used in radiotherapy to develop the films can achieve a reproducibility of about 3% over a period of one day (Metcalfe *et al* 1997). To reduce this uncertainty to a minimum, all used films of a batch were processed at the same time.

Uncertainty	Type	Value
chemical processing	systematic/random	3%
reference films	systematic	0.5%
conversion ADC to OD	systematic	1%
conversion OD to dose	systematic	2%
fog and base correction	systematic/random	0.5%
film reading	random	0.5%
positioning	random	0.3%
energy dependence	systematic/random	0.8%
total uncertainties		3.9%

Table 2 *Summary of the uncertainties in the dose determination at the reference depth in water using a radiographic film (ADC = analog digital converter).*

The uncertainty for the linear conversion from the ADC to OD was estimated by analyzing different reference films and for the conversion of OD to dose the accuracy of the fit for the calibration films was considered (figure 1).

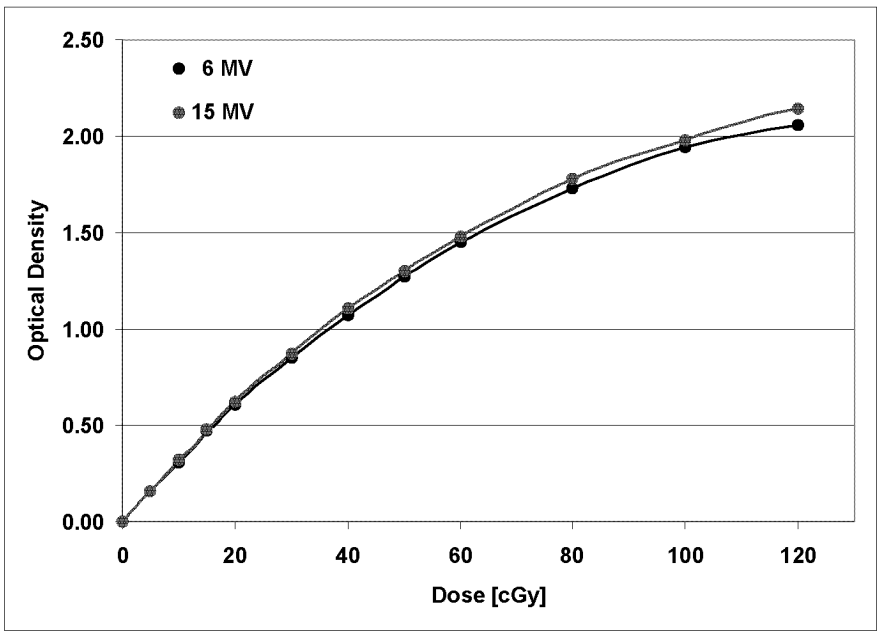

Figure 1 *Calibration curve OD to dose used for the film measurements.*

For film measurements of a relative lateral dose distribution only the uncertainties of the film reading and the energy dependence are important and therefore the precision of dose determination in this case can be estimated to be about 1%. In this work, the reference conditions for the film calibration measurements were: field size 10 x 10 cm^2, source surface distance 100 cm, depth of measurements 1.5 cm (6 MV) or 2.5 cm (15 MV).

Since the film response is energy dependent and the energy spectra change with depth in a phantom, the response of film versus dose becomes also depth dependent. Therefore, a correction factor b is introduced for the dose determination in a depth d, $D(d)$, different to the reference depth d_{ref} (Williamson *et al* 1981):

$$D(d) = D(d_{ref}) \cdot \left(\frac{1}{1 + b\left(d - d_{ref}\right)} \right)$$

where b is set to 0.0018 cm^{-1} and 0 for the 6 and 15 MV beam respectively. This means that there is no energy dependence for the 15 MV beam, because the amount of low-energy photons is negligible. An alternative manual method has been investigated by Hale *et al*, who performed calibration curves for the conversion of OD to dose at several depths by orienting the films parallel to the central axis.

7.2.4. Energy spectrum measurements

As already pointed out in 7.2.1., the uncertainty for the transmission measurements can be estimated to be about 0.5%. Consequently this measurement uncertainty together with the uncertainties in the reconstruction algorithm itself lead to an uncertainty of the reconstructed energy spectra. In the works of Francois *et al* 1993 and Catala *et al* 1995, where this method of reconstruction of photon energy spectra has been introduced, the uncertainty of the method was studied. By analyzing different simulated cases they showed that the overall uncertainty of the set up must be less than 1%. With this condition, they have seen that the error on the reconstructed spectrum remains acceptable for use in clinical practice (Francois *et al* 1993). For example, an uncertainty of 0.5% in the transmission measurements results in an uncertainty of the modal energy in the reconstructed spectrum of about 2-3%.

References

AAPM TG-21 1983 A protocol for the determination of absorbed dose from high-energy photon and electron beams *Med. Phys.* **10** 741-71

Attix F H 1986 *Introduction to radiological physics and radiation dosimetry* (New York: John Wiley & Sons)

Brahme A, ed 1988 Accuracy requirements and quality assurance of external beam therapy with photons and electrons *Acta Oncol.* Suppl. 1

Catala A, Francois P, Bonnet J and Scouarnec C 1995 Reconstruction of 12 MV bremsstrahlung spectra from measured transmission data by direct resolution of the numeric system *AF=T Med. Phys.* **22** 3-10

CERN Application Software Group Computing and Network Division 1995 GEANT–detector description and simulation tool *CERN Program Library Long Writeup* W5013 Genf

Dixon R L and Ekstrand K E 1976 Heuristic model for understanding x-ray film characteristics *Med. Phys.* **3** 340-5

Essers M and Mijnheer 1999 In vivo dosimetry during external photon beam radiotherapy *Int. J. Rad. Oncol. Biol. Phys.* **43** 245-59

Francois P, Catala A and Scouarnec C 1993 Simulation of x-ray spectral reconstruction from transmission data by direct resolution of the numeric system *AF=T Med. Phys.* **20** 1695-703

Grusel E and Rikner G 1986 Evaluation of temperature effects in p-type silicon detectors *Phys. Med. Biol.* **31** 527-34

Hale J I, Kerr A T and Shragge P C 1994 Calibration of film for accurate megavoltage photon dosimetry *Med. Dosim.* **19** 43-6

Hubbell J H 1999 Review of photon interaction cross section data in the medical and biological context *Phys. Med. Biol.* **44** R1-R22

ICRU 1984 Stopping powers for electrons and positrons *ICRU report 37* (Bethesda, MD: International Commission on Radiation Units and Measurement)

Lanson J H, Essers M, Meijer G J, Minken A W, Uiterwaal G J and Mijnheer B J 1999 In vivo dosimetry during conformal radiotherapy: requirements for and findings of a routine procedure *Radiother. Oncol.* **52** 51-9

Lillicrap S C, Burns J E, Greene D and Williams P C 1983 Revised Code of Practice for the dosimetry of 2 to 35 MV x-ray, and of caesium-137 and cobalt-60 gamma-ray beams *Phys. Med. Biol.* **28** 1097-104

Metcalf P, Kron T. and Hoban P 1997 *The Physics of Radiotherapy X-Rays from Linear Accelerators* (Madison: Medical Physics Publishing)

Rogers D W O and Bielajew A F 1990 Monte Carlo techniques of electron and photon transport for radiation dosimetry *The Dosimetry of Ionizing Radiation, Vol III* ed K R Kase, B E Bjärngard and F H Attix (San Diego,CA: Academic Press) pp 427-539

SGSMP (Swiss Society of Radiation Biology and Medical Physics) 1992 Dosimetry of high energy photon and electron beams *Recommendations No. 4*

van Dam J, Leunens G and Dutreix A 1990 Correlation between temperature and dose rate dependence of semiconductor response; influence of accumulated dose *Radiother. Oncol.* **19** 345-51

Williamson J F, Khan F M and Sharma S C 1981 Film dosimetry of megavoltage photon beams: a practical method of isodensity-to-isodose curve conversion *Med. Phys.* **8** 94-98

Yeo I J, Wang C-K C and Burch S E 1999 A new approach to film dosimetry for high-energy photon beams using organic plastic scintillators *Phys. Med. Biol.* **44** 3055-69

8

Conclusions

In the present work, several MC beam models for the 6 and 15 MV beams of a Varian Clinac 2300 C/D have been investigated in order to develop a flexible tool, which is able to describe and analyze the dosimetry in radiotherapy even for highly complex application techniques used in IMRT. Investigations on simple source models showed promising results within the geometric radiation field, when using the radially dependent energy spectra together with the spatial photon fluence distribution of the radiation beam in an output plane below the secondary collimator jaws. Although these models are not complex during generation they show the common advantages of beam models like reducing calculation time compared with full MC calculations and disk space for the phase space files. However, their main drawbacks are the lack of flexibility (only fixed field sizes available), the limited accuracy outside the geometric radiation field and some assumptions which have been made for the head scatter, especially for its angular distribution. Therefore, a more complex multiple source model (MSM) was developed to characterize the beam. Based on phase space data of a set of eight square fields, the MSM is defined for arbitrary rectangular field size. The consideration of the main head components allows to describe the head scatter in detail and, thus, to characterize the beam also outside the geometric radiation field. Furthermore, the MSM was supplemented with a model for an MLC in order to enable MC calculations for MLC shaped fields including IMRT fields produced by the step and shoot or the dynamic MLC method. With these attributes the supplemented MSM is a flexible tool for dosimetric investigations in radiotherapy. Comparisons of original phase space (PS) data with PS data reproduced with the MSM show that the MSM is able to represent the MC simulation of the radiation transport through the complete geometry of the accelerator head. In addition, the energy spectra for target photons show a very good agreement with measured ones derived from transmission measurements for both energies, 6 and 15 MV. Moreover, all dose calculations performed for several setups using the MSM resulted in good agreement compared with dose calculations using the

original PS data or measurements respectively. Therefore the supplemented MSM is able to describe and analyze the dosimetric situation in conformal radiotherapy, which was the aim of this thesis. The simulation time for an IMRT field is rather long, i.e. the CPU time is about 7 minutes per segment on an Alpha XP 1000 workstation for 1 million primary particles per segment for the 6 MV beam. For the 15 MV beam the CPU time increases by about a factor of 1.5, however the statistical accuracy for the 15 MV beam results about 1.5 times better than for 6 MV. In order to reduce the long simulation times, variance reduction methods have to be implemented in the MC code.

Apart from the application discussed in this thesis, the MSM might also be a useful tool for *in vivo* dosimetry in IMRT verification, assuming a portal dose image as input, e.g. from an electronic portal imaging device. In the work of Keller (1999) several methods are discussed to extract the primary photon fluence in the portal plane from a portal dose image. By backwards ray tracing the primary fluence through the actual anatomy of the patient, the primary fluence above the patient can be calculated (McNutt *et al* 1996, 1997). The forward MC dose calculation taking the head scatter from the MSM into account leads to the *in vivo* dose distribution of the patient for the actual fraction in the treatment, which includes the true scatter radiation from the patient and therefore no scatter correction has to be made as in other forward dose calculation tools mentioned in chapter 1. Additionally one can think of further applications of the MSM, such as parameter studies in patient set up or organ motion.

In summary, the MSM supplemented with the dynamic MLC is shown to be a powerful tool not only for investigational and benchmarking purposes but also for IMRT treatment planning.

References

Keller H 1999 Investigations on absolute portal dosimetry for the verification of static and dynamic dose delivery in radiotherapy *PhD Thesis* Swiss Federal Institute of Technology Zurich

McNutt T R, Mackie T R, Reckwerdt P and Paliwal B R 1996 Modeling dose distributions from portal dose images using the convolution/superposition method *Med. Phys.* **23** 1381-92

McNutt T R, Mackie T R and Paliwal B R 1997 Analysis and convergence of the iterative convolution/superposition dose reconstruction technique for multiple treatment beams and tomotherapy *Med. Phys.* **24** 1465-76

Curriculum Vitae

Michael Karl Fix	born on May 20, 1967 in Waldkirch i. Br., Germany citizen of Germany
1973-1977	Elementary school in Kollnau i.Br., Germany
1977-1983	Geschwister-Scholl Gymnasium in Waldkirch i.Br.
1983-1985	Vocational training for toolmaker at Rold AG Niederwinden, Germany (aborted due to medical problems)
1985	Volunteer at the Berufskolleg in Waldkirch i.Br.
1985-1988	High school (Gymnasium) in Emmendingen, Germany
1988-1989	Military service
1990-1992	Physics studies at Albert-Ludwigs-Universität in Freiburg i.Br., Germany
1992-1995	Physics studies at ETH Zürich with graduation as Dipl. Phys. ETH
1996-1998	Post-graduate course in Medical Physics at ETH Zürich with graduation as Dipl. NDS ETHZ in Medical Physics
1996-2001	Ph.D. student and scientific researcher at the Institute for Biomedical Engineering, ETH and University of Zürich

Acknowledgements

I would like to express my thanks to:
Prof. Dr. Peter Rüegsegger and *Prof. Dr. Peter Niederer*, for giving me the opportunity to explore many fascinating issues in the field of Medical Physics. *Prof. Dr. Ralph Eichler*, for agreeing to co-examine this thesis.

In addition, I wish to express my sincere gratitude to
Ernst Born, who deserves my cordial gratitude, for his continuous support and advice and the numerous stimulating suggestions he made. Thanks for the many fruitful discussions during these years; I also enjoyed the many personal conversations we had.
Harald Keller, for the many enlightening discussions and his support in all matters concerning the first part of this thesis. *Peter Manser*, for his tremendous advice in working and personal matters, from which I will profit for the rest of my life. *Marco Stampanoni*, whose diploma and post-graduate diploma theses contributed substantially to this work. *Stefanie Oestreicher*, for the helpful discussions not only about my but also her work and the exceptionally teamwork as system operator. *Andres Laib*, for always having an open ear for all matters and his valuable advice. *Bruno Koller*, who has me taught all I know about VMS, and for his amicable attitude. *Stefan Hämmerle* and *Emmi Rüegsegger*, for even-mindedness and friendliness, which created a positive working atmosphere. *Adrian Kohlbrenner*, who gave me every possible support to convert image formats. *Walter Pistoa*, whose amusing character always brought colour into everyday life.
Bruno Willi, for his great guidance through the PC world. *Paul Lüthi*, for his speedy and precise preparation of the aluminum attenuators.
The people of the Division of Medical Radiation Physics, especially *Daniel Vetterli* and *Roberto Mini*, for providing an excellent environment for scientific research and their expert knowledge in all questions concerning the experimental setups.

My *family*, especially *Petra*, *Nicolas* and *Lena* without whose constant encouragement and love I could not have completed this thesis.